University of Alberta

DEVELOPMENT AND ANALYSIS OF MAGNETIC CARBON NANOTUBE AND MICROBUBBLE-ASSISTED HIGH CENTRIFUGATION FIELD TECHNIQUES FOR THE INCREASE OF CELL MEMBRANE PERMEABILITY

by

Chuan He

A thesis submitted to the Faculty of Graduate Studies and Research
in partial fulfillment of the requirements for the degree of

Doctor of Philosophy

in

Biomedical Engineering

Department of Electrical and Computer Engineering

Spring 2014

Edmonton, Alberta

Dedication

To my family

Abstract

To cure diseases at the gene level, therapeutic biomaterials need to enter the cells. However, since the cell membrane is a highly selective structure, its permeability is usually very low. In this thesis, we propose two innovative and efficient methods to increase cell membrane permeability.

The first method is based on magnetic carbon nanotubes (mCNT). By using atomic force microscope force curve analysis (AFM-FCA) and transmission electron microscope (TEM) images, we successfully develop mCNT from raw materials. Under a magnetic field, mCNT can facilitate cell endocytosis by firmly attaching onto the cell membrane. As a result, the cell membrane permeability of several mammalian cell lines is increased.

The second method to increase cell membrane permeability is based on using microbubble-assisted high centrifugation field. The mechanism of this method relies on the centrifugation-induced collision between microbubbles and cells and the force of the microbubbles bursting. The validity of this method is demonstrated on mammalian cells and plant cells. Theoretical models are built to simulate the interaction between microbubbles and cells in the centrifugation field. The simulation results indicate that intracellular pathways can be created once the relative velocity between the microbubble and cell is beyond a critical value. In addition, cell deformed morphology induced in the centrifugation field and cell mechanical properties are closely related to the resulting increase of cell membrane permeability.

Acknowledgments

First and foremost, I express my sincere gratitude to my advisor, Prof. Jie Chen, for providing me the valuable opportunity to work with him. This thesis would not have been possible without his patient guidance, constant encouragement and continuous support. His vision, enthusiasm and desire for excellence not only influenced my current research, but also gave me a lifelong role model for my professional and personal development.

I also thank Prof. Hongbo Zeng, Prof. James Xing, Prof. Hao Zhang and Prof. Tian Tang, not only for their inspiring suggestions for my research, but also for their sharing of their research and career development experience. I also thank Prof. Steve Dew and Prof. H. Vicky Zhao for agreeing to serve on my thesis committee, and for their time and effort spent reviewing my thesis.

Thanks should also go to all my colleagues and friends during my Ph.D. studies, for their friendship, help and inspiration. I feel lucky to be their friend, and I am also deeply grateful for all that I have learned from them. Special thanks go to Dr. Quanrong Gu, Dr. Yuzhi Hao, Min Huang, Xiaoyan Yang, Peng Xu, Woon, Qian Wan, Jida Xing, Alexandra Savchenko, Fabrice MVondo, Mianzhen Mo and Zhiyin Zhou. I will always remember my happy times with them.

Finally and most importantly, I give my heartfelt gratitude to my aunt's family and my parents. Without their patience, unconditional support and countless sacrifices, I could never have accomplished so much and reached this milestone in my life. I dedicate this thesis to them.

Table of Contents

List of Tables

List of Figures

maximum strain on cell membrane of deformation type I and deformation type II cell by varing cell membrane elastic modulus $E_{membrane}$

Figure 5-4 (a) equivalent strain distribution on the cell membrane of deformation type I cell when $E_{membrane}$ =4.5×10^4*N/m*^{2}; (b) equivalent strain distribution on the cell membrane of deformation type I cell when $E_{membrane}$ =4.5×10^8*N/m*^{2}; (c) equivalent strain distribution on the cell membrane of deformation type II cell when $E_{membrane}$ =4.5×10^4*N/m*^{2}; (d) equivalent strain distribution on the cell membrane of deformation type II cell when $E_{membrane}$ =4.5×10^8*N/m*^{2}

Figure 5-5 (a) average strain on cell membrane of deformation type I and deformation type II cell by varing cell membrane shear modulus $G_{membrane}$; (b) maximum strain on cell membrane of deformation type I and deformation type II cell by varing cell membrane shear modulus $G_{membrane}$

Figure 5-6 (a) equivalent strain distribution on the cell membrane of deformation type I cell when $G_{membrane}$ =20*N/m*^{2}; (b) equivalent strain distribution on the cell membrane of deformation type I cell when $G_{membrane}$ =10^5*N/m*^{2}; (c) equivalent strain distribution on the cell membrane of deformation type II cell when $G_{membrane}$ =20*N/m*^{2}; (d) equivalent strain distribution on the cell membrane of deformation type II cell when $G_{membrane}$ =10^5*N/m*^{2}

Figure 5-7 (a) average strain on the cell membrane of deformation type I and deformation type II cell by varing cell elastic modulus E_{cell} ; (b) maximum strain on cell membrane of deformation type I and deformation type II cell by varing cell elastic modulus E_{cell} ; (c) average strain on the cell membrane of deformation type I and deformation type II cell by varing membrane thickness *h*; (d) maximum strain on the cell membrane of deformation type I and deformation type II cell by varing membrane thickness *h*

List of Abbreviations

Acronyms	Definition
ADA	adenosine deaminase
AFM	atomic force microscope
AFM-FCA	atomic force microscope force distance curve analysis
ARDS	acute respiratory distress syndrome
CII	collision induced impulsion
CNT	carbon nanotube
CPP	cell penetrating peptide
CVD	chemical vapour deposition
DLS	dynamic light scattering
DLVO	Derjaguin - Landau - Verwey - Overbeek
DMF	N,N - Dimethylformamide
DNA	deoxyribonucleic acid
DSPC	1,2-distearoyl-sn-glycero-3-phosphocholine
FACS	fluorescence-activated cell sorting
FBS	fetal bovine serum
FDA	fluorescein diacetate
FD	FITC-Dextran
FITC	fluorescein isothiocyanate
JKR	Johnson - Kendall - Roberts
LBST	laser beam gene transduction
mCNT	magnetic carbon nanotube
MTC	magnetic twisting cytometer
OT	optical tweezers
P/S	penicillin and streptomycin

pDNA	plasmid DNA
PTFE	polytetrafluoroethylene
RCF	relative centrifugal force
SDS	sodium dodecyl sulfate
SEM	scanning electron microscope
siRNA	small interfering RNA
SWNT	single-walled carbon nanotube
TGA	thermal gravimetric analysis
TEM	transmission electron microscope
VDW	Van der Waals

List of Symbols

Symbols	Definitions
F_{ad}	adhesion force between two spherical particles
W_{ad}	work of adhesion
R	particle radius
A	Hamaker constant of material
D	separation distance between two particles or surfaces
C_{AB}	coefficient in the particle-particle pair interaction
ρ	density of material
ε	dielectric constant of material
n	reflective index of material
k	Boltzmann constant
T	temperature
h	Planck constant
ψ	surface potential
$1/\kappa$	Debye length
r	rotational radius
g	gravitational acceleration
η	viscosity of liquid
N	rotations per second
V	velocity between two particles
κ_b	bending rigidity
c_{fl}	numerical constant
P	pressure
K_a	compressibility modulus

$T_{membrane}$	membrane thickness
z	penetration depth

Chapter 1

I. Introduction

1.1 Motivation

In 1990, a four-year-old girl was treated with virus-encapsulated functional genes to fix a specific DNA sequence coding for adenosine deaminase (ADA). The fixed gene could have led her body to reproduce enough immune cells called T lymphocytes to recover immune system function [1]. Although the treatment was initially successful, the therapeutic effect diminished over time. However, this occasion was the first time in human history that doctors tried to treat a disease at the gene level. This new generation of illness treatment was thus named “gene therapy” from then on.

Since its first emergence, gene therapy has been widely influential. Scientists and doctors have been trying hard to improve the effectiveness of this method, but have rarely succeeded. To date, the most successful application of gene therapy might be in restoring sight to blind people. In Bennett et al.’s study, the researchers succeeded in helping three adults to improve their sight in both eyes by using gene therapy. After treatment,

the patients could see in a low-light environment and were also able to find their way around [2]. Why did gene therapy succeed in helping restore sight, but fail in other applications? To answer this question, an understanding of the gene therapy mechanism and current methods is necessary.

During gene therapy, functional genetic biomaterials such as plasmid DNA (pDNA), antisense oligonucleotides, ribozymes, siRNA or peptide nucleic acids are inserted into cells to recover or silence the targeted gene expression [3]. Theoretically, once researchers identified the abnormal functional genes for diseases like cancer, immunodeficiency, leukemia, Parkinson diseases or AIDS, they all could be cured at the gene level [4-8]. Gene therapy targeted human cells can be divided into two categories: germ line cells and somatic cells [9]. If a germ line cell is treated with gene therapy successfully, the patient's descendants will also carry the therapeutic transgene. By contrast, if only somatic cells are fixed, only the recipient of the treated somatic cell will benefit. As this technology is still in its infancy, it requires even more time than traditional pharmaceutical technology to reach the clinical trial stage. Investigators usually use *in-vitro* environments to test the therapeutic effect of genetic materials on cells. A major barrier for gene therapy in *in-vitro* environments is that delivering genetic biomaterials into the cells is very difficult [10]. Usually

gene therapy has to fulfil the following criteria in order to succeed. (1) The genetic biomaterials must penetrate the cell membrane and enter the cytoplasm. If cells take the biomaterial through endocytosis, the internalized biomaterial is trapped in the endosomes and has to be released from them. (2) The genetic biomaterial needs to move through the cytoplasm and reach the cell nucleus. (3) After entering the cell nucleus, the genetic biomaterial must still maintain its function and be expressed under the proper cell translation mechanism [10]. Normally, cells will not take up genetic biomaterial spontaneously. As a result, researchers have had to develop carriers to help the genetic materials pass through the cell membrane. The first carrier proposed was a virus, which is still the most efficient carrier to date. The human immune system is very efficient in identifying and destroying a virus carrier with genetic material. Therefore, to avoid triggering the immune response, the virus carrier has to be modified to cheat the immune system. However, a practitioner cannot fully control the virus after injecting it into a human body. Although a virus is programmed to target non-functional cells, it might still attack healthy cells, thus leading to unexpected lethal diseases. In a study in 2000, three of the ten children treated with virus-assisted gene therapy developed leukemia [11]. However, in organs where the immune system is less efficient, the virus-gene composite is safer and has

a higher possibility of entering the target cells and replacing the abnormally functioning gene with therapeutic ones. For this reason, gene therapy for curing eye disorders has had more positive results than gene therapy for other disorders.

Researchers have been aware of the virus safety issue for a long time, and alternative non-viral delivery methods are urgently needed. Based on the literature review carried out for this thesis, these methods can be generally divided into two categories: chemical-based methods and physical-based methods. This project developed one chemical-based method and one physical-based method to increase cell membrane permeability and, potentially, help accelerate the research progress on non-viral gene therapy methods.

1.2 Thesis contribution

As explained above, one critical step in gene therapy is to deliver the therapeutic genetic biomaterials into cells. To increase delivery efficiency, cell membrane permeability needs to be increased. In this thesis, two methods are developed to increase cell membrane permeability. The first method is based on the magnetic carbon nanotube (mCNT). The second method is based on microbubble-assisted high centrifugation field. The contributions of this thesis are summarized as follows:

1.2.1 Development and analysis of mCNT for increase of cell membrane permeability

A carbon nanotube (CNT), with its high-aspect ratio characteristic, is considered as a biocompatible material [12]. This thesis demonstrates that mCNT can efficiently increase the membrane permeability of several mammalian cell lines.

In Chapter 2, the experimental procedures to extract mCNT from normal CNTs manufactured from the arc-discharge method are discussed. As well, a method based on atomic force microscope force curve analysis (AFM-FCA) and transmission electron microscope (TEM) images to identify magnetic particles that are attached onto CNTs is developed. In the final step, the increase of cell membrane permeability by evaluating the delivery efficiency of mCNT combined with fluorescein isothiocyanate (FITC) is discussed.

1.2.2 Development and analysis of microbubbles-assisted high centrifugation field to increase cell membrane permeability

Microbubbles are used widely in ultrasound imaging as a common agent to improve image contrast. Microbubbles can also be used to induce pores on a cell membrane under an ultrasound field. Beyond the above two

applications, this study finds that microbubbles can also increase the cell membrane permeability by centrifuging with cells at a high speed.

In Chapter 3, the microbubble manufacture method is explained. Next, the experiment design and the successful delivery results of FITC-Dextran (FD) into two mammalian cell lines by centrifuging cells with microbubbles at high speed are explained. Finally, two mechanisms for the developed method are proposed. The first mechanism is based on the collision between the microbubbles and the cells. A theoretical model indicates that once the relative velocity between the microbubbles and cells is beyond a critical value, the hydrodynamic force will be large enough to penetrate the cell membrane. The second mechanism exploits microbubble bursting and is supported by scanning electron microscope (SEM) images.

In Chapter 4, the application of microbubble-assisted high centrifugation field is extended to plant cells. The experimental results show that FD can be efficiently delivered into canola protoplasts or even canola cells with cell walls by using this method.

1.2.3 Investigation of the effect of cell deformed morphology and mechanical properties on cell membrane permeability

Cell mechanics has been a popular research topic recently. This study finds that the deformed cell morphologies induced by the centrifugation field and cell mechanical properties are very important elements in the increase of cell membrane permeability.

In Chapter 5, confocal microscope images are used to rebuild three-dimensional deformed cell morphologies under a high centrifugation field. In the next step, the structural behaviors of two such models are investigated under microbubble collision pressure. Several cell mechanical properties are also varied to observe the resulting change of the strain value and strain distribution on the cell membrane. It is found that cells with more abnormal shapes experience a higher strain under the same collision-induced pressure. The strain value of the cell membrane is determined by the synergistic effect of the cell mechanical properties and cell morphology. The strain-intensive area tends to be aligned with the cell elongation region induced in a centrifugation field.

1.3 Thesis Outline

This thesis is organized as follows. In Chapter 2, the development and identification of mCNT with its application for intracellular delivery is reported. In Chapter 3, the method of using a microbubble-assisted high centrifugation field for increasing cell membrane permeability in mammalian cancer cells is explained. A simple model to study the interaction mechanism is also presented. In Chapter 4, the delivery results from using the method of microbubble-assisted high centrifugation field on plant cells are reported. In Chapter 5, three-dimensional cell models are built to evaluate the effect of deformed cell morphology and mechanical properties on the range of strain values and distribution on cell membranes under pressure. Conclusions and potential future research topics are presented in Chapter 6.

Chapter 2

II. Development and analysis of mCNT for increasing cell membrane permeability

2.1 Introduction

2.1.1 Chemical-based methods to increase cell membrane permeability

The main mechanism of chemical-based methods to increase cell membrane permeability is to trigger the cells' own endocytosis ability [1]. Endocytosis can be defined as the uptake of extracellular materials by the infolding of the plasma membrane, followed by the pinching off of a membrane-bound vesicle containing extracellular fluid and materials [13]. The use of chemical-based methods to increase cell membrane permeability can be traced back to 1928, when Griffith first found that some genes from dead bacteria could be transferred to the rough strain (without cell wall) and make it pathogenic [14]. He concluded that

immersing the bacteria in a calcium-chloride-rich medium with genetic materials could help transfer the bacterial inheritable properties. This phenomenon was later found to be universal in almost all cells [15-18]. This technique is widely used in science labs today to produce functional pDNA from bacteria such as *Escherichia Coli*. Unfortunately, the mechanism of this method is still unknown. One possible explanation is that the high concentration difference of calcium ions inside and outside the cell creates a high osmotic pressure. As a result, the calcium ions are driven into the cytoplasm. In order to balance the internal calcium ion concentration, the calcium ion pumps inside the cells try to excrete the extra calcium ions by creating a pathway on the cell membranes. Most likely, the plasmids can then diffuse into the cytoplasm at the same time. Another mechanism might be that the positively charged calcium ion can neutralize the negatively charged pDNA, so the plasmid can attach to the cell membrane more easily. Thus, the possibility of pDNA being taken up through the cell endocytosis process is increased [19].

Although the calcium chloride method is effective, it is highly toxic and has reproducibility problems. As a result, its future prospects in clinical or *in-vivo* application are limited. To overcome these limitations, carrier-based delivery methods are developed. The carrier will be chemical materials with both hydrophilic and hydrophobic regions. Due to this structure, the

chemical carrier will self-aggregate into either single-layer or double-layer micelles in water. The desired biomolecules such as pDNA will then be capsulized inside the hydrophobic or hydrophilic regions of these micro-scale or nano-scale micelles. These micelles will carry the biomolecules to the cell surface and enter the cell through cell endocytosis. The micelle structure will then release the biomolecules into the cytoplasm. Chemical carriers are made from materials such as polymers, dendrimers, lipid-based nanocarriers, nanoparticles, drug nanocrystals, liquid crystals, nanoemulsions and hydrogels [20-26]. The advantages of these chemical carrier-based methods are as follows. (1) Most chemical carriers are biocompatible and will not induce a serious immune response [27-29]. (2) The polymers or lipid incorporated can help condense the pDNA into a globule morphology, which is much smaller than the normal coiled shape and is easier to deliver [30]. (3) The chemical carriers provide a protective area for the pDNA in order to avoid nuclease degradation [31, 32]. (4) Some chemical carriers can help the genes to get released from the endosomes [33]. (5) The chemical carrier can be designed to have special functions, such as specific targeting functions [34]. (6) The chemical carriers can be mixed together or chemically reacted together. It has been reported that by combining several chemical carriers together, either the material toxicity can be greatly reduced or the delivery efficiency can be

increased [35-38]. The chemical carrier-based method has a major disadvantage. It cannot increase the cell membrane permeability for cells with extremely low endocytosis ability, like stem cells or neural cells. The sensitiveness of different cells to different chemical carriers also varies greatly. Another disadvantage is that the chemical carriers aggregate readily when circulating in the human body [39]. Recently, materials like copolymers have gained more and more attention [40]. An increasing number of clinical trials is also underway. Grossman has reported significant positive results for the treatment of arterial disease by using various polymers as genetic drug carriers [41].

Another carrier-based method is based on cell-penetrating peptide (CPP). As its name indicates, CPP specializes in penetrating cell membranes. When the biomaterials are linked to CPP, they enter the cells with the CPP at the same time. The translocation of CPP into the cytoplasm is based mainly on three possible mechanisms: direct penetration, endocytosis mediated translocation and translocation through the formation of a transitory structure [42-44]. Milletti produced a detailed review, suggesting that the physical-chemical properties of CPP, CPP three-dimensional structures, and the origins of CPP will all be key elements in the translocation process of cell membranes [45]. CPP has successfully delivered biomaterials such as siRNA, nucleotides, small molecules,

proteins and other peptides into cytoplasm both *in-vitro* and *in-vivo* [46-48]. Compared to the chemical carrier-based method, the CPP-based method takes a more active role in triggering the cell response, while chemical carrier-based method responds mainly passively to cell endocytosis. However, as future pharmaceutical products, CPPs still have typical shortcomings such as short duration of action and lack of oral bioavailability [45]. Proper chemistry and formulations are needed to address these problems.

2.1.2 Introduction of CNT

Since Iijima discovered the CNT in 1991 [49], the interest in CNTs has increased exponentially. They are currently being studied in a wide range of areas, such as microelectronics [50], renewable energy [51], and biomedicine [52]. In biomedical applications, Pantarotto reported increased gene delivery efficiency by applying CNT as a proper transporter [52]. Two methods are used to modify CNTs with magnetic materials. The first method is to load magnetic nanoparticles inside CNTs, but doing so requires the diameter of the CNT to be around 300*nm,* which is too large for application in *in-vitro* study [53]. The other way is to purify the CNTs manufactured by using the chemical vapour deposition (CVD) method. According to Cai's work, CVD-produced CNTs usually have

embedded magnetic nanoparticles inside the CNTs. The diameter (around 100*nm*) of these CNTs is much smaller than that of other mCNTs [54].

2.1.3 Work description

In this chapter, an innovative purification method is described for obtaining mCNT from arc-discharged SWNTs to increase cell membrane permeability by facilitating cell membrane endocytosis. The arc discharge technology requires two electrodes placed in a gaseous atmosphere where a direct current (DC) passes through. The production of SWNTs usually requires the insertion of a mixture of metallic catalysts into the anode [49]. As a result, metallic catalyst nanoparticles such as nickel will remain in the produced SWNTs as impurities; some of the nanoparticles are scattered around the SWNTs, while the others are attached onto the SWNTs, or wrapped by amorphous carbons (which are by-products during the arc discharge process). Among the various purification methods reported in the literature, chemical oxidation including gas-phase oxidation and liquid oxidation, filtration, centrifugation, high-temperature annealing, and ultrasonication are commonly used [55-61]. In recent years, researchers have also tried to use combinations of the above methods for purification [62-68]. These methods are intended to be very efficient in removing all impurities. Our developed method selectively keeps nickel nanoparticles, which are firmly attached onto the SWNTs after purification,

while the scattered nickel nanoparticles and amorphous carbons surrounding the mCNT are removed. The nickel nanoparticles remaining on the SWNT surface, however, will enable the SWNT to respond to an external magnetic field.

Another innovation is to use AFM-FCA combined with the TEM image to monitor the SWNT purification process. An AFM force distance curve is a plot representing the force-distance relationship between the AFM tip and the sample surface, and the separation distance is controlled by the closed-loop scanning system of the AFM during the measurements [69]. The interacting force measured in the air is usually the Van der Waals (VDW) force. AFM-FCA can be applied to obtain information about the electric properties, the elastic modulus, and the chemical-bonding strengths of the samples [69]. The curve can be drawn after a complete AFM tip-engaging process is performed, which includes an approaching and detaching cycle. When the tip is approaching the sample surface, at one point, the attraction between the AFM tip and sample surface causes the sudden movement of the tip towards the sample surface (the so-called jump-in process), leading to a peak value on the curve. Similarly, during the detaching process, the AFM tip remains in contact with the sample surface due to the VDW attractive force until one critical point is reached when the interface separates (the so-called jump-out process). This jump-

out will lead to another peak value on the force-distance profile. Compared with the peak force in the approaching process, the jump-out peak value in the detaching process is less affected by the tip engaging speed, which corresponds to the force necessary to remove the cantilever tip from the sample surface and is essentially a measure of the adhesive force; thus, only the AFM force curve during the detaching process is presented, and the related peak value is defined as the adhesion force. The main idea is that the ranges of the adhesion force for three fundamental materials are identified first: (1) the range of the adhesion force between the AFM tip and amorphous carbon, (2) the range of the adhesion force between the AFM tip and the pre-purified SWNT, and (3) the range of the adhesion force between the AFM tip and the nickel nanoparticles. Then, based on the values of the adhesion forces, the sample points taken during the different purification treatments are used to qualitatively differentiate the materials in the mixtures. Compared with TEM, Scanning Electron Microscope (SEM), or Raman spectra, which are commonly used to monitor the purification process, this method is fast and intuitive. As previously mentioned, the major impurities in arc-discharged SWNTs are nickel nanoparticles and amorphous carbons [55]. To show that adhesion force information extracted from AFM-FCA can be used to differentiate the three standard materials mentioned above, an experimental model and

numerical hypothesis are provided. The calculation results are in line with our experimental results. To our best knowledge, this thesis is the first report on using AFM-FCA to assist SWNT purification.

In the final stage, the developed mCNTs are connected with FITC and mixed with cells. The magnetic field is expected to guide the mCNTs moving towards the cells and attaching onto the cell membranes. As a result, the possibilities of the cell endocytosis of mCNTs are increased.

2.2 Development of mCNT

2.2.1 Materials and instruments

Materials: Sodium dodecyl sulfate (SDS) (05030) was purchased from Fluka Analytical®. Hydrogen peroxide (H3410) was purchased from Sigma®. A polytetrafluoroethylene (PTFE) membrane filter (0.45μm) (TE36) was purchased from Whatman®. N, N-Dimethylformamide (DMF) (31,993-7) and amorphous carbon (484164) were purchased from Aldrich®. 95% ethanol was purchased from Commercial Alcohols®. DI-water was obtained from the university purification system.

Pre-purified SWNTs (652490) used as the standard material were purchased from Sigma® and manufactured by using the arc-discharge method. The manufacturer claimed that the nanotubes were purified with nitric acid and left in a highly functionalized form.

The arc-discharged raw SWNTs (519308) used in our developed purification process were also purchased from Sigma®. Based on the product information, the sample composition is 50%-70% carbon, as determined by Raman Spectroscopy and SEM. It contained residual catalyst impurities Ni. The SWNTs were in bundles of length ~20μm, and the individual tube length was unknown.

Instrumentations: A thermo Fisher Scientific® Sorvall T1 centrifuge and a Fisher Scientific® bath sonicator (FS30H) were used in the purification process. TEM images were acquired on a JEOL® TEM microscope. A sample solution was sonicated for 10*mins* and immediately transferred in drops onto the TEM mesh grid, which was dried overnight at room temperature. TEM images were photographed on the next day. AFM imaging and related FCA were performed on a Veeco® Multimode V SPM under the contact mode. The AFM tip used was a Veeco® NP-20. Firstly, the pH value of the sample solution was adjusted to approximately 7.0. A small amount of the sample solution was then directly transferred in drops onto the silicon wafer. The sample was dried at room temperature overnight.

2.2.2 Standard materials preparation

(a) A certain amount of amorphous carbon was first sonicated in DI water for 10*mins*, then directly transferred in drops onto a small piece of silicon wafer. The sample was dried at room temperature.

(b) To further ensure that the pre-purified SWNT was pure, SWNT samples were oxidized in concentrated acid (sulphuric acid: nitric acid=3:1) for 40*mins* and sonicated in H_2O_2 for another 2*hrs*. After being transferred in drops onto the silicon wafer, the solution was dried at room temperature.

(c) The pure nickel nanoparticles were obtained from a redox reaction between nickel oxalate and formic acid. The remaining sample preparation steps were the same as those for the amorphous carbon.

2.2.3 Purification process

The purification process consisted of three treatments: (a) SDS treatment, (b) organic solvent treatment and (c) H_2O_2 treatment, which are described in detail as follows:

(a) SDS Treatment

26.2*mg* SWNTs were weighed and dispersed in a solution of 10*mL* 20% concentration SDS and 150*mL* DI water. The container was gently agitated, and then the sample solution was sonicated for 2*hrs*. After

sonication, a sample solution was transferred into centrifuge tubes and centrifuged at 11180*g* (10000*RPM*) for 10*mins*. The sediment was discarded; the supernatant was filtered through a PTFE membrane with 0.45*μm* pore size. In order to completely remove the SDS after filtration, DI water was used in several rinse cycles to wash the SWNTs remaining on the filter membrane. Finally, the SWNTs remaining on the PTFE membrane were suspended in 95% ethanol. A sample solution was stored at room temperature for TEM analysis and the next purification treatment.

(b) Organic Solvent Treatment

Before the organic solvent treatment, the sample solution needs to be completely dried. After the drying process, the SWNTs were suspended in 100*mL* DMF, after which the sample solution was refluxed at 130^{o}C for 98*hrs*. After the reflux process, the sample solution was filtered again through a PTFE membrane with 0.45*μm* pore size. DI water was used to wash away the remaining DMF. The SWNT remaining on the PTFE membrane was suspended in 95% ethanol and stored properly for TEM and AFM analysis and the next purification step.

(c) H_2O_2 Treatment

Before the H_2O_2 treatment, the sample solution needs to be completely dried. After the drying process, 22*mL* H_2O_2 was added to suspend the

SWNTs. The sample solution was then sonicated for a total duration of 4*hrs*. To ensure that enough oxidant was supplied 10*mL* H_2O_2 was supplemented into the solution at 2*hr* intervals. After the H_2O_2 treatment, the samples underwent the same filtration process as that previously described. Finally, the SWNT was stored in a 95% ethanol solution.

2.3 Results and discussion

In order to use the defined adhesion force to differentiate materials, the ranges of the adhesion forces associated with different materials should be shown to have little overlap with one another. Both experimental and theoretical approaches were carried out in order to reach a convincing conclusion.

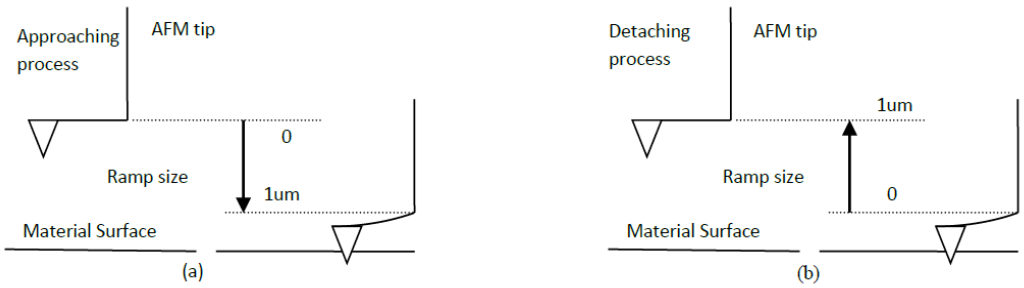

Figure 2-1 (a) AFM tip approaching process, the ramp size was measured from top to bottom; (b) AFM tip detaching process, the ramp size was measured from bottom to top.

2.3.1 Experimental evaluation of adhesion force

The adhesion force between the AFM tip and the pure standard materials by AFM-FCA was determined in the contact mode. The AFM tip approached and detached from the sample surface at a rate of 1*Hz*. During the experiments, an AFM topographic image reflecting the sample's surface structure was first generated. As the adhesion force depends on the geometry and size of the interacting surfaces, the rules for choosing the sample points from the generated AFM image are universal throughout the standard material analysis. The rules are (a) the morphology feature must be clear on the image and (b) the surrounding morphology of the sample points must be similar, such as the slope, particle size, etc. In reality, keeping sampling consistent even in the same material was difficult. Therefore, instead of using only one force value, a range of adhesion force values was identified for each material. The real "separation distance" between the AFM tip and sample surface is the combined effect of several factors, such as the chemical composition of the material, the chemical composition of the tip, the morphology of the material surface, the morphology of the tip, and the detaching speed. Because many of these factors can vary, this process is sensitive. Therefore, accurately measuring the range of the separation distance is difficult. To summarize the adhesion force from the sample points, in Fig.

2-3a and c, the vertical axis represents the value of the adhesion force, while the horizontal axis represents the AFM tip ramp size when the peak adhesion force is obtained. This ramp size is termed the ramp size at the jump-out. As shown in Fig. 2-1a, in the approaching process, the AFM tip started in the air at 0*nm* and then moved 1*μm* to reach the material surface, but this process did not guarantee the tip would just touch the material surface after 1*μm*. During the detaching process, as shown in Fig. 2-1b, the “turnaround” point, where the tip was going to be lifted, is defined as 0nm, and from then on, the ramp size was measured in the opposite direction. Because only the detaching process is presented in this thesis, the ramp size in all related images was measured from the “bottom”. In Fig. 2-5, 2-7, and 2-8, the vertical axis is the same as that mentioned above, but the horizontal axis shows the overall ramp process during the detaching process.

(1) Adhesion force on amorphous carbon

The AFM image information of amorphous carbon is presented in Fig. 2-2a-c. Fig. 2-2a shows the overall amorphous carbon structure, while Fig. 2-2b presents this surface morphology in a three-dimensional view. Fig. 2-2c demonstrates the sample points used for AFM-FCA. They are marked by red dots. Fig. 2-3a summarizes the adhesion forces from all the sample points. As mentioned above, to maintain a relatively consistent sampling

environment, all the sample points were taken on one carbon bump, which was measured to be spherical with a radius of 1*μm* (see Fig. 2-2c). Fig. 2-3a shows that the majority of the values of the adhesion force for the amorphous carbon range from 26.9 to 38.7*nN* with an average of 31.7*nN*. One point was measured to be about 22.8*nN* far away from the majority. The micro-scale morphology variance may lead to a relatively wide range of AFM tip ramp sizes. For the other two standard materials, the experiment results presented in Fig. 2-2d-i are listed in the same way.

(2) Adhesion force on SWNT

The SWNTs' radius was measured to be 87, 92.2, 108, 123, or 130*nm* (see Fig.2- 2f); thus, the SWNTs were in a bundled form in this case. The SWNTs are supposed to have a relatively uniform morphology, as they do in our experimental results. The variance in adhesion force is much smaller compared to that of amorphous carbon (see Fig. 2-3b). The adhesion force values range from 21.8 to 26.8*nN* with an average of 23.9*nN*. In addition, the range of the ramp size at the jump-out is smaller than that of the amorphous carbon.

(3) Adhesion force on nickel nanoparticles

Fig. 2-2g reveals the presence of many nickel nanoparticles, but their radius can be divided into 27, 55, 111 and 222*nm* according to Fig. 2-2i.

The range of the adhesion force for nickel is from 6.8 to 21.3*nN,* with an average of 16.4*nN*. The pattern of the adhesion force scattering of the nickel nanoparticles is similar to the one for amorphous carbon (see Fig. 2-3c), but the variance in the value of the adhesion force is larger. Because nickel is metallic, not only the morphology difference led to the variance in the adhesion force, but the crystal orientation also plays an important role in determining the adhesion force values [70].

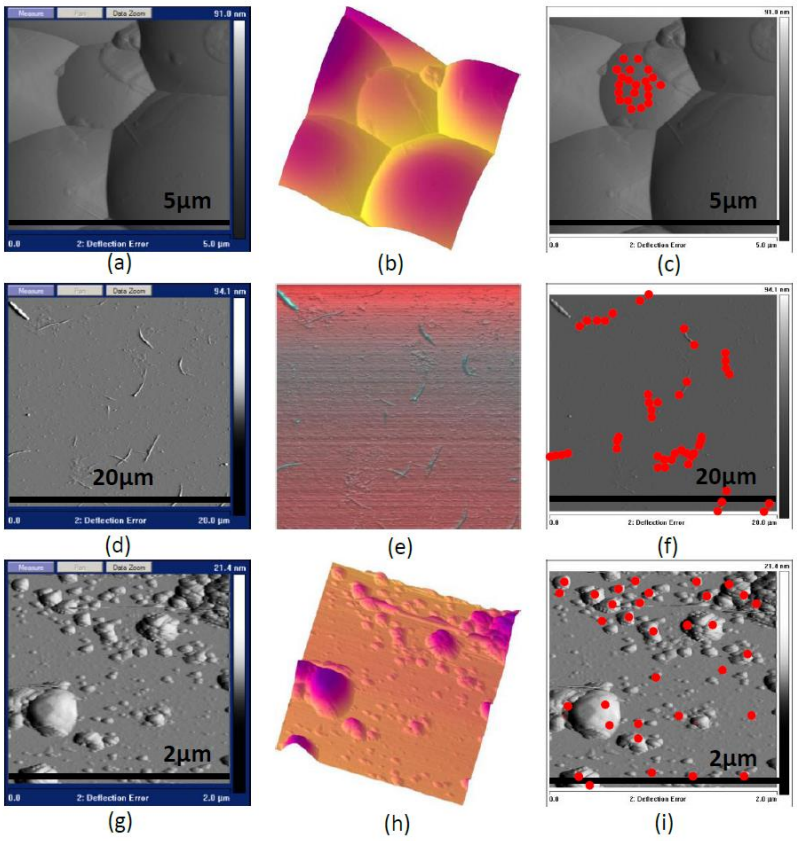

Figure 2-2 (a) AFM deflection image of amorphous carbon; (b) three- dimensional image of amorphous carbon; (c) point image of amorphous carbon, red dots represent the sampling point; (d) AFM deflection image of SWNT; (e) three-dimensional image of SWNT; (f) point image of SWNT, red dots represent sample points; (g) AFM deflection image of nickel nanoparticles; (h) three-dimensional image of nickel nanoparticles; and (i) point image of nickel nanoparticles, red dots represent sample points.

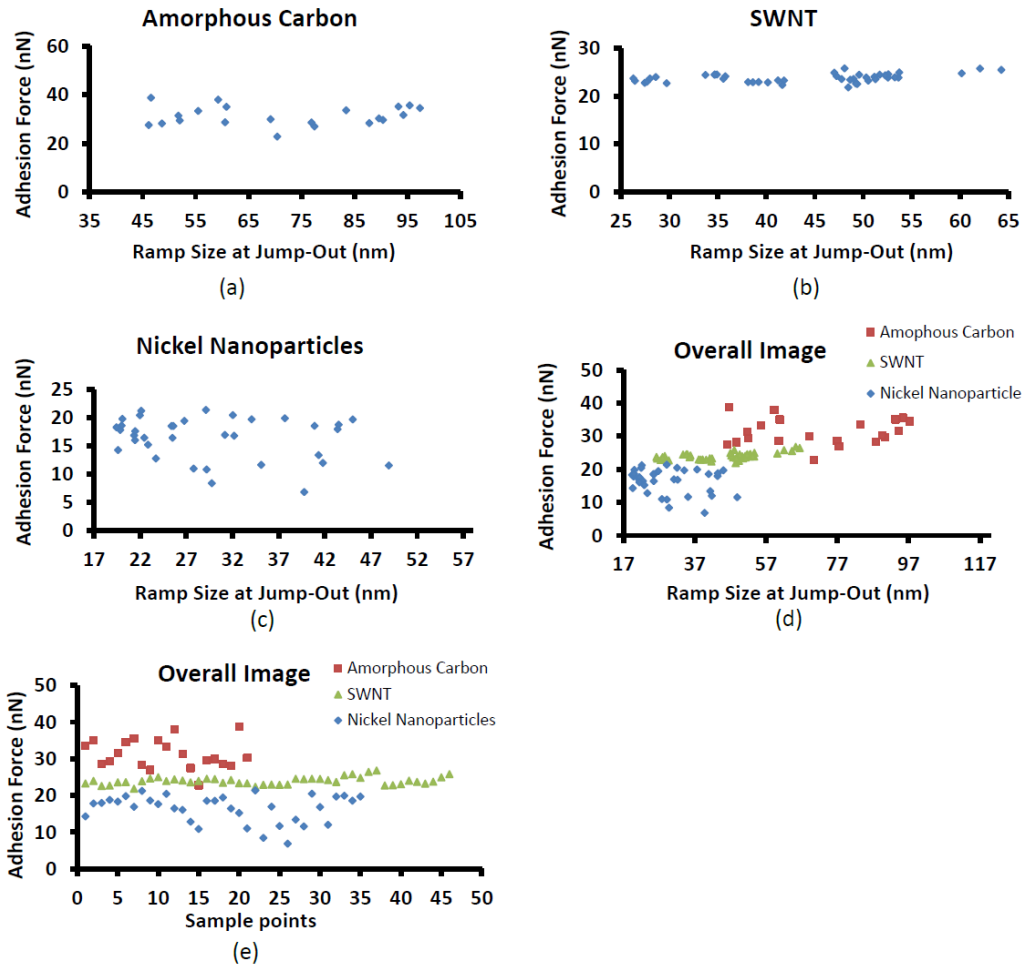

Figure 2-3 (a) adhesion force vs. ramp size for amorphous carbon; (b) adhesion force vs. ramp size for SWNT; (c) adhesion force vs. ramp size for nickel nanoparticles; (d) overall image of adhesion forces of amorphous carbon, CNT and nickel nanoparticles versus ramp size; and (e) overall image of adhesion forces of amorphous carbon, CNT and nickel nanoparticles versus sample points.

In order to compare the range of the adhesion force for different materials, the overall adhesion force scattering is shown in Fig. 2-3d and e. In Fig. 2-3d, the vertical axis represents the value of the adhesion force, while the horizontal axis represents the AFM tip ramp size at the jump-out. In Fig. 2-

3e, the vertical axis shows the value of the adhesion force, while the horizontal axis is the sample's serial number. In both Fig. 2-3d and e, based on the density of the points for each material, clear distinctions are visible among these three materials except for the single exceptional point from amorphous carbon. The range of the adhesion force is 28-38*nN* for the amorphous carbon, 22-26*nN* for the bundled SWNTs, and 6.8-20*nN* for the nickel nanoparticles. These non-overlapping force ranges provide an effective means to differentiate the three materials from the AFM adhesion force measurements. The force measurement in our experiments is very accurate. Specifically, the normal distance resolution of the AFM was 0.1*nm*. The spring constant of the cantilever used in the force measurement was 0.27*N/m* for the amorphous carbon, 0.30*N/m* for the SWNTs and 0.28*N/m* for the nickel; therefore, the force sensitivity was <0.1*nN*.

2.3.2 Theoretical evaluation of adhesion force

The Johnson-Kendall-Roberts (JKR) theory can be used to predict the force needed to separate a particle from another particle or a flat surface [71]. This model is widely used but requires the deformation of the interacting particles to be small. In the JKR theory, the adhesion force follows the equations below:

$$F_{ad} = 3\pi R \frac{W_{ad}}{2} \tag{2-1}$$

$$R = \frac{R_1 R_2}{R_1 + R_2} \tag{2-2}$$

$$W_{ad} \approx \frac{A_{12}}{12\pi D_0^{\,2}} \tag{2-3}$$

$$A_{12} = \sqrt{A_1 A_2}\,, \tag{2-4}$$

where F_{ad} is the defined adhesion force between two spherical particles; R_1 and R_2 are the radii of curvature of the interacting particles; W_{ad} is the work of adhesion per unit area; A_1, A_2 and A_{12} are the Hamaker constants, and D_0 is the closest separation between the two particles.

To simply estimate the defined adhesion force between the AFM tip and the material, the calculation contains the following steps: (a) choose the interaction model determined by the JKR theory, (b) measure the size of the two interacting particles from the AFM deflection image, (c) identify the Hamaker constants based on the existing literature, and (d) calculate the adhesion force by using Eq. 2-1 to 2-4 based on the JKR theory.

In the following calculation, R_1 stands for the radius of the sample material and was determined by using the pixel method. For example, the scale bar takes 100 pixels, and thus a SWNT's diameter, which takes 50 pixels, will

be half of the scale bar. R_2 stands for the radius of the AFM tip. D_0 is chosen to be 0.16*nm* (see [72]). Based on this separation, Eq. 2-3 has been successfully applied to predict the surface and adhesion energies of a variety of compounds ranging from simple molecular materials to polymers. This separation should also be close to the real contact separation between the molecules/atoms on the AFM tip and the contacting molecules on the opposing sample surface.

(1) AFM tip interacting with amorphous carbon surface

In Fig. 2-2b, the amorphous carbon has a spherical structure, since the AFM tip is simplified as a sphere; thus, the separation process is approximated as two spherical surfaces locally interacting with each other. All the sample points were taken on three carbon bumps, and measured to be spherical with a radius (R_1) of 1μm, while the tip radius (R_2) was around 20*nm*. In [73], the Hamaker constants for amorphous carbon and Si_3N_4 are $A_1=50\times10^{-20}J$ and $A_2=17.4\times10^{-20}J$, respectively. The calculated adhesion force for amorphous carbon is 28.2*nN*. Fig. 2-4a compares the experimental values with the theoretical values for amorphous carbon. The vertical axis stands for the value of the adhesion force, while the horizontal axis is the sample point serial number. Clearly, the theoretical value falls into the range of the adhesion force measured experimentally.

(2) AFM tip interacting with SWNT surface

The SWNTs' radius (R_1) was measured to be 87, 92.2, 108, 123, or 130*nm*; thus, the SWNTs in our sample are obviously in bundled form. Although bundled SWNTs are best approximated by a cylindrical structure, the exact JKR solution for the adhesion force between a sphere and a cylinder is not available. Therefore, here we approximate the bundled SWNTs by a sphere and use Eq. 2-1 to estimate the adhesion force. More accurate calculation of the adhesion force between a sphere and a cylinder can be obtained through numerical analysis by, for example, using the finite element method. However, the use of this method is beyond the scope of this thesis. Accordingly, the bundled SWNTs are considered as a sphere; while the AFM tip represents the other sphere. The tip radius (R_2) is around 20*nm*. The Hamaker constants for CNT and Si_3N_4 are $A_1=50\times10^{-20}J$ and $A_2=17.4\times10^{-20}J$ [73] . The calculated adhesion force for the bundled SWNTs is 23.4, 23.7, 24.3, 24.8, and 24.9*nN*. Fig. 2-4b compares the experimental values with the theoretical values for SWNTs. Most of the theoretical values agree well with the experimental values.

(3) AFM tip interacting with nickel nanoparticle surface

The nickel nanoparticles are simplified to have a spherical structure. This process is also approximated as two spherical surfaces interacting locally. The radius for a nickel particle (R_1) can be classified into 27.5, 55, 111 and 222*nm*, while the tip radius (R_2) is 20*nm*. The Hamaker constants for nickel and Si_3N_4 are $A_1=22\times10^{-20}J$ and $A_2=17.4\times10^{-20}J$ [72]. The calculated adhesion force for nickel nanoparticles of different sizes is 11.1, 14.1, 16.3 and 17.6*nN,* respectively, which is in line with the experimentally measured values.

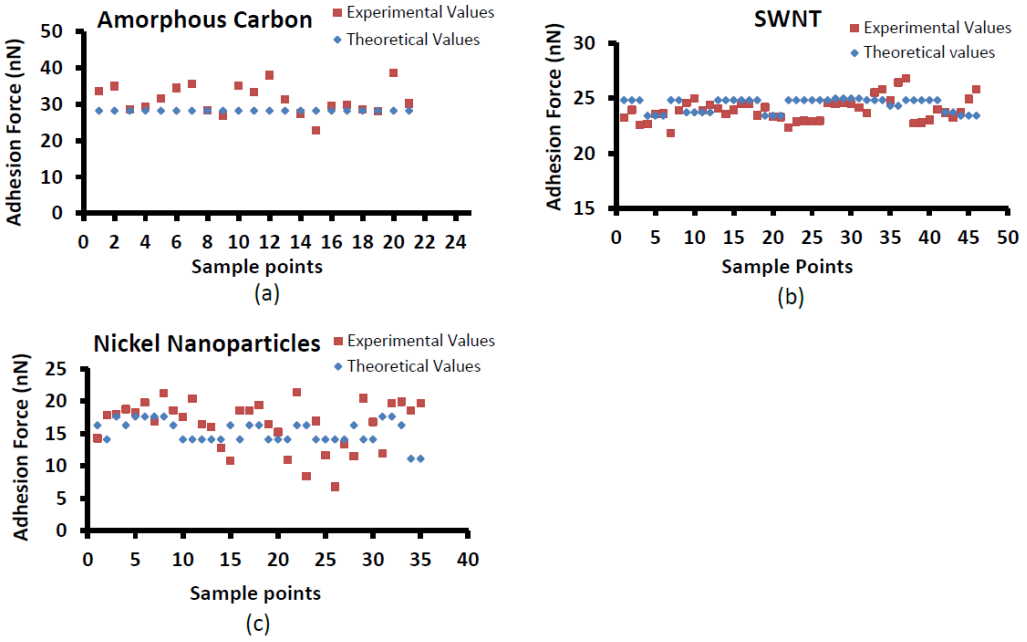

Figure 2-4 (a) adhesion forces of amorphous carbon, experimental values vs. theoretical values; (b) adhesion forces of SWNTs, experimental values vs. theoretical values; and (c) adhesion forces of nickel nanoparticles, experimental values vs. theoretical values.

In our experiment, we have shown that, from both our theoretical analysis and experimental measurements, a clear difference in adhesion force exists for these three materials. Perry et al. used a similar method to measure the adhesion force between AFM tip and the amorphous carbon [74]. However, these researchers used a tungsten AFM tip instead of a silicon nitride AFM tip. Since the Hamaker constant of tungsten is at least twice as large as that of silicon nitride [75], the adhesion force that Perry et al. measured (at least 54.4nN) is much bigger than ours. Decossas et al. measured the adhesion force between the AFM tip and the carbon

nanotubes [76]. Although these researchers used the same silicon nitride AFM tip as ours, the carbon nanotubes that they measured were mainly multi-walled carbon nanotubes. The reported value is around 20nN. Therefore, the exceptional point in amorphous carbon can be considered to be abnormal and will not be considered in the following analysis. Overall, the experimental measurement is in accordance with the theoretical calculation. To explain the difference between the theoretical value and the experimental value, in addition to the reasons previously mentioned, two other possible factors are that (a) in the theoretical analysis, all the samples are assumed to have a round morphology or at least a round cross area, but this assumption is not always true in experiments; and (b) in the theoretical calculations, the tip is assumed to interact with the middle of the samples. However, the tip is difficult to control in experiments. Some of the sample points are not located in the center of the particle.

Although the adhesion forces for these three materials are obviously different, in our simple theoretical calculation the size difference allows us to distinguish the amorphous carbon from the SWNT. In the purification process, a clear distinction exists between the size of the aggregated amorphous carbon and the bundled SWNT. Although sometimes the materials' size can change due to external forces, if properly sampled, the

morphology around the sample location will be quite consistent for each material. Therefore, in general, the adhesion force can be used to distinguish these three different materials on the same substrate. By comparing the ranges of the adhesion force identified for the three standard materials, the materials in the mixture can be distinguished based on their adhesion force value. This method was used to monitor the SWNT purification process.

2.3.3 Monitoring the purification process

TEM and AFM-FCA were performed at different purification steps. The aim was to monitor the process and judge which material was either removed or changed in status after the respective process.

(1) Original SWNT material

Fig. 2-5 shows the status of the original arc-discharged raw SWNT material before any purification. Fig. 2-5a and b were taken by TEM, while Fig. 2-5c was taken by AFM. In Fig. 2-5a, some SWNTs are visible in a separated state as outlined by the line of red dashes.

However, SWNTs are difficult to locate in Fig. 2-5b. One can speculate that most of the SWNTs are entangled by the amorphous carbon (the grey block) and wrapped by the nickel nanoparticles (the dark points). In Fig. 2-

5c, differentiating the SWNTs from the impurities is even more difficult than doing so in Fig. 2-5a.

AFM-FCA was performed in the scanning area, and the data for all three materials are shown in Fig. 2-5d-i. According to the specific range of the adhesion force values for the associated standard material, the data can be separated into three sections, with each one standing for one standard material. For instance, all the points marked by the red dots in Fig. 2-5d represent the amorphous carbon with an adhesion force range from 28.8 to 38.3*nN*, while the red dots in Fig. 2-5f and h represent the SWNTs with an adhesion force range from 23.1 to 25.3*nN,* and the nickel nanoparticles with an adhesion force range from 7.5 to 20*nN*, respectively. After the results of performing AFM-FCA are compared with the information extracted from the TEM images shown in Fig. 2-5a and b, more direct and detailed information about the material distribution in the accumulation area can be obtained. A comparison of the distribution of the three materials on the substrate confirms that the SWNTs are surrounded by the amorphous carbon and nickel nanoparticles.

(2) Sample after SDS Treatment

Fig. 2-6 presents the status of the SWNTs during the SDS treatment. Fig. 2-6a shows that the original SWNTs are not water-soluble. SDS is a highly effective surfactant used here to assist the dispersion process. Sonication

further disperses the accumulation of amorphous carbon and nickel nanoparticles. It is assumed that SDS will quickly surround the separate nanoparticles to make them water-soluble after sonication has fragmented the accumulated block shown. The resulting SWNTs are temporarily dispersed in the solution (see Fig. 2-6b). However, some impurities are too large and heavy for SDS to ensure good solubility. By centrifuging the solution at 10000*RPM*, many large impure particles are removed (see Fig. 2-6c). Fig. 2-6d and e show the TEM images of the SWNTs after the SDS treatment. More SWNTs are observed, again supporting our hypothesis that the SWNTs were initially embedded in the accumulation of impurities.

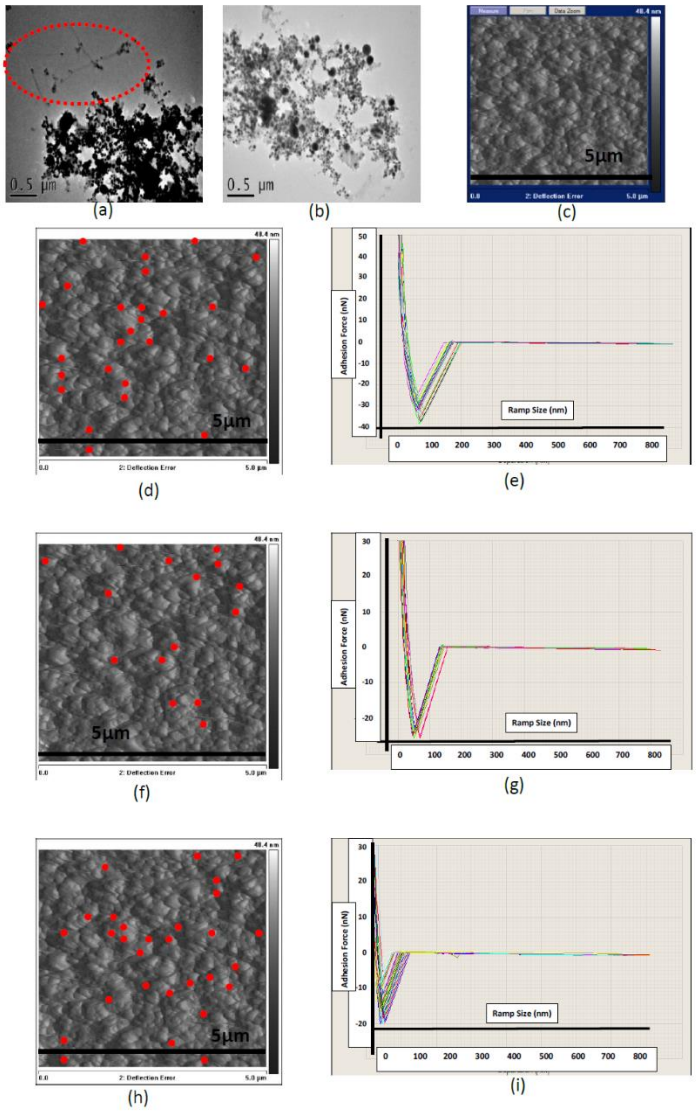

Figure 2-5 (a), (b) TEM image of the original SWNTs; (c) AFM deflection image of the original SWNTs; (d), (e) AFM-FCA of original SWNT, sample points represent amorphous carbon; (f), (g) AFM-FCA of original SWNT, sample points represent SWNT; and (h), (i) AFM-FCA of original SWNT, sample points represent nickel nanoparticle.

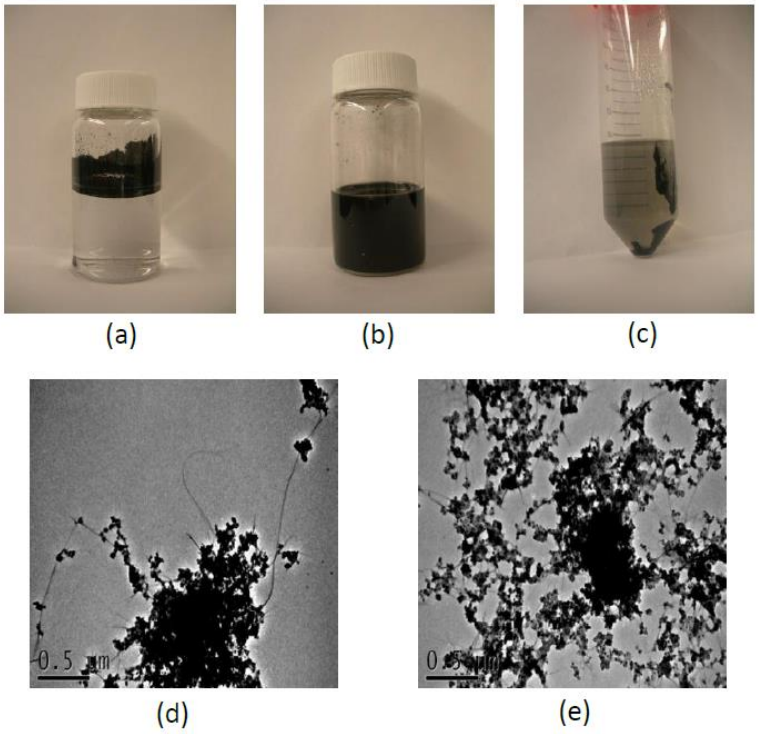

Figure 2-6 Experimental process of SDS treatment: (a) original SWNT in DI water; (b) original SWNT mix with SDS; (c) SWNT solution after centrifugation; and (d), (e) TEM image of SWNT after SDS treatment.

(3) Sample after Organic Solvent Treatment

Fig. 2-7a-c presents the SWNT distribution and morphology after the organic solvent treatment. Fig. 2-7d and i present the AFM-FCA result. After the organic solvent treatment, the condition of the SWNTs greatly changes. Fig. 2-7a and b show that with TEM technology, the accumulation blocks further divide into smaller pieces, while many SWNTs are still entangled. The amorphous carbons now exhibit loose structures. Fig. 2-7c, which was taken by AFM, shows many small particles, and one

bundle of SWNTs, inside the red circle, can be directly identified in the right bottom corner.

Although DMF is usually used to disperse SWNTs [77], DMF is suspected to cause the accumulated impurities to be fluffy. In the block morphology shown in Fig. 2-7a and b, more and more organic solvents are adsorbed into the accumulation blocks, leading to further loosening of the accumulation structure. Since the amorphous carbon is no longer firmly packed, releasing the entrapped SWNTs will be easier.

The AFM image also validates our speculation. Sonication breaks the accumulation into many separate nanoparticles. Based on the AFM-FCA measurements shown in Fig. 2-7d, e, h, and i, these nanoparticles are composed of nickel nanoparticles or amorphous carbons. For the amorphous carbon sample points, the adhesion force is from 28.2 to 36*nN*, while for the nickel nanoparticles, the adhesion force ranges from 11.3 to 19.8*nN*. As mentioned above, in the right bottom of Fig. 2-7c, one tube can be clearly identified by its morphology. The other tubes' whole structure cannot be identified only from the morphology, but AFM-FCA provides additional information about the embedded SWNTs. Fig. 2-7f shows the sample points representing the SWNTs. The adhesion forces on these SWNTs range from 22.5 to 26*nN*.

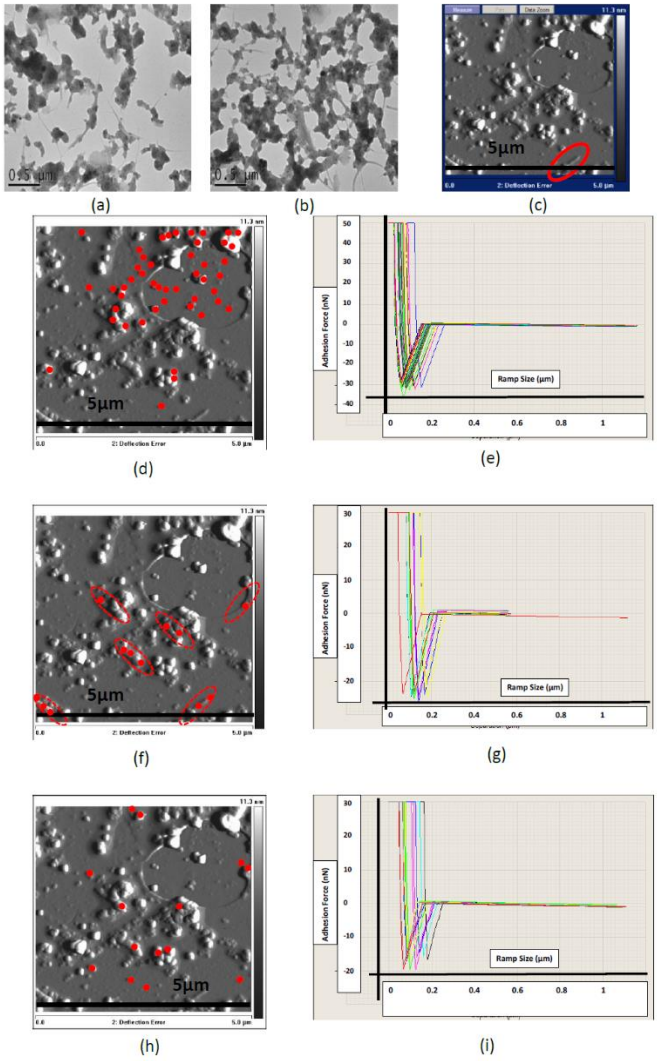

Figure 2-7 (a), (b) TEM image of SWNT after organic solvent treatment; (c) AFM deflection image; (d), (e) AFM-FCA of SWNT after organic solvent treatment, sample points represent amorphous carbon; (f), (g) AFM-FCA of SWNT after organic solvent treatment, sample points represent SWNT; and (h), (i) AFM-FCA of SWNT after organic solvent treatment, sample points represent nickel nanoparticles.

The overall morphology of the SWNTs is estimated and marked by the red dashed circle. These SWNTs are not totally purified. According to Fig. 2-7c, some small accumulations still exist on the SWNTs' surface. Based on

the AFM-FCA result shown in Fig. 2-7d and h, the dots sampled on these accumulations are associated with the amorphous carbon and nickel nanoparticles. This finding indicates that the SWNTs are covered by the impurity.

(4) Samples after H_2O_2 Treatment

Feng has shown that H_2O_2 can help oxidize amorphous carbon at room temperature [78]. Since after the organic treatment, the amorphous carbon become loose scaffolding, removing them becomes much easier. Fig. 2-8a-c presents the distribution and morphology of the SWNT, while Fig. 2-8d and 8e show the result of the AFM-FCA. After the H_2O_2 treatment, which is the last purification stage, most amorphous carbon and scattered nickel nanoparticles are removed, and thus the SWNTs are free in solution, with the nickel nanoparticles attached onto their surface. As Fig. 2-8a shows, almost no amorphous carbon is left in the solution. The short SWNTs are observed for the first time and are evenly distributed in the image. 82% of the SWNTs have a dark point in the tip, indicating the presence of nickel nanoparticles. The magnification of a specific SWNT is shown in Fig. 2-8b. Two images are shown for comparison in Fig. 2-9. Fig. 2-9a presents the results after the first two purification steps proposed in this thesis were completed and the material was sonicated with H_2O_2 for 2*hrs*. Although the CNT is similar to the one shown in Fig. 2-8a, many

impure particles still remain in the sample. Based on their status in the image, most of the scattered particles might be composed of amorphous carbon. The mCNTs shown in Fig. 2-9b were treated under a different purification step. Instead of the SDS treatment and organic solvent treatment, the mCNT raw material was first directly sonicated in HNO_3 and H_2SO_4 for 40*mins*. The resulting solution was then sonicated with H_2O_2 for 4*hrs*. The comparison of the resulting mCNTs (Fig. 2-9b) with the ones in Fig. 2-8a shows that the nickel particles are obviously much smaller after acid treatment. Clearly more nickel particles are oxidized under the strong acid treatment. Although treated with the strong acid method, some amorphous carbon still remains around the mCNT. To further demonstrate the purification result, Thermal Gravity Analysis (TGA) analysis was performed. The result is shown in Fig. 2-10, where the black curve is the weight-loss curve as the temperature increases, while the blue curve is its derivative, which shows the weight-loss velocity. After the original raw SWNT (Fig. 2-10a), is heated to 1000^oC, nearly 40% of the original weight remains while the peak weight-loss velocity is around 420^oC. For our purified SWNT, as Fig. 2-10b illustrates, the weight-loss velocity peak is around 550^oC which has significantly shifted. This result indicates that most of the amorphous carbon has been removed. Compared to the weight of the raw material sample, the remaining weight in the purified

sample accounts for less than 5% after TGA, so that after the purification process, a large portion of the metal nanoparticles are also removed. The change in the TGA curve before and after the purification of the CNT accords with the result reported by Dillon [79].

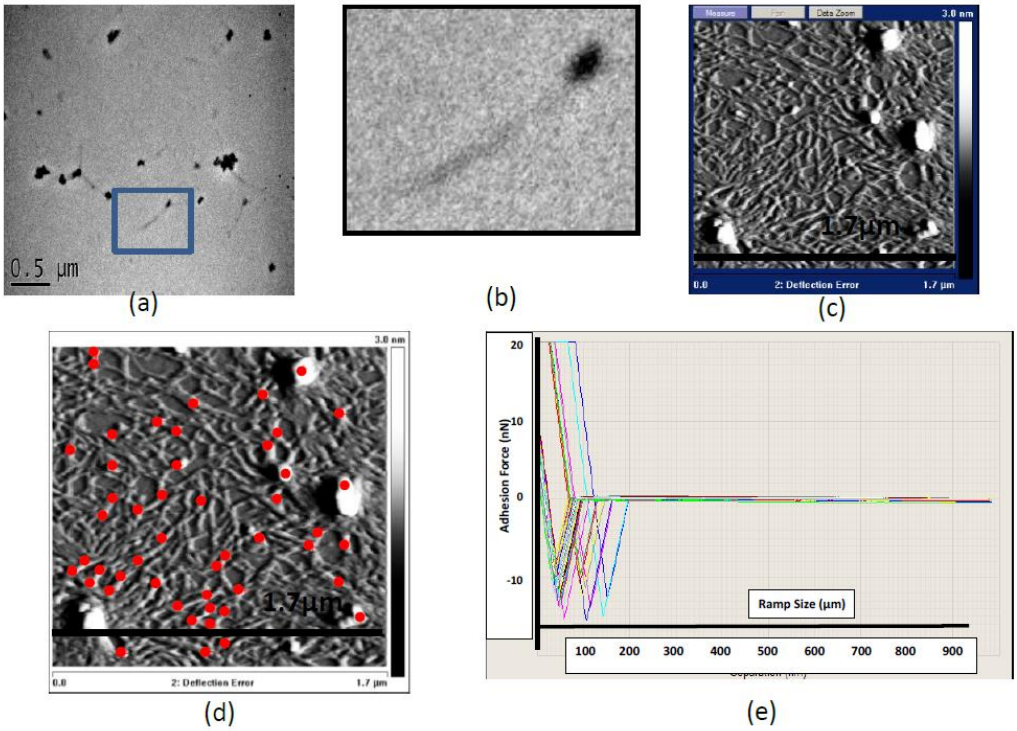

Figure 2-8 (a), (b) TEM image and (c) AFM deflection image of mCNT after H_2O_2 treatment for 4*hrs*; (d), (e) AFM-FCA of mCNT after H_2O_2 treatment for 4*hrs*, sample points represent nickel nanoparticles.

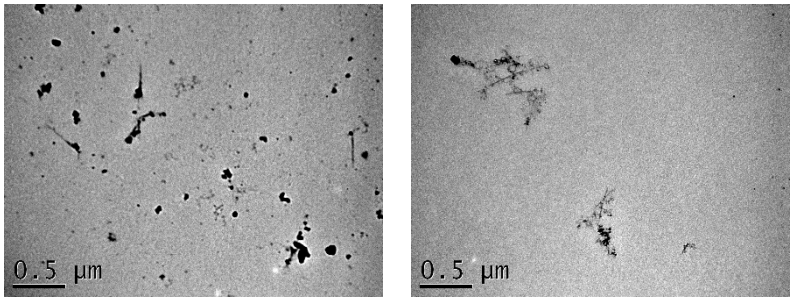

(a) (b)

Figure 2-9 TEM images of mCNT under different purification steps: (a) after the first two steps, the mCNT was sonicated with H_2O_2 for 2*hrs*; (b) the mCNT raw materials was sonicated in HNO_3 and H_2SO_4 (1:3) for 40*mins*, and then sonicated with H_2O_2 for 4*hrs*.

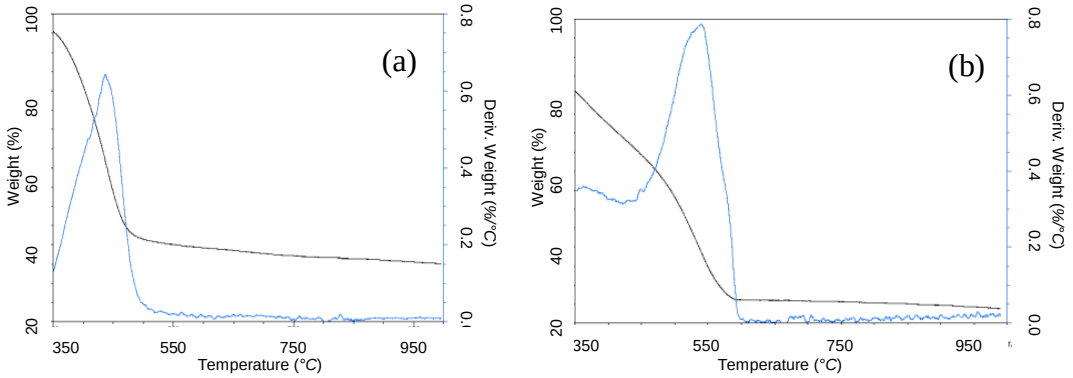

Figure 2-10 TGA analysis of mCNT: (a) before purification and; (b) after purification.

The AFM image shown as Fig. 2-8c reveals many SWNTs, and also some large particles in the solution. In Fig. 2-8d and e, the AFM-FCA classifies these large particles as nickel nanoparticles because the values of the defined adhesion forces on the large particles range from 8.9 to 15.5*nN*, which drop into the experimentally measured adhesion force range for nickel nanoparticles. Since the SWNT sample solution has gone through three filtration stages, most of the small nickel nanoparticles in the filtrate have been removed. As SWNTs at some point may block the pores on the

PTFE membrane, some of the large nickel particles may still remain in the sample solution.

At the red dots shown in Fig. 2-8d, the adhesion forces on the SWNTs also fall into the range for nickel nanoparticles, possibly due to the nickel nanoparticles that are still attached onto most of the CNTs. The nickel particles are added as a catalyst during the SWNT production stage. According to Gavillet et al., the SWNTs' growth mode is not really understood even though some models have been proposed to explain it [80]. Based on Gavillet et al.'s research, when the particle diameter is within the order of a few tens of nm, which it definitely is in our case, many nickel nanoparticles will precipitate on the surface of the SWNTs [80]. However, sonication is harsh, especially for the prolonged sonication in our case. Therefore, in addition to the precipitate, some catalyst particles might be trapped in the tip of the SWNT, thus leading to a firm combination. Gavillet et al. also mention this possibility [80]. Since nickel is sensitive to a magnetic field, the nickel nanoparticles on the SWNTs might make the SWNTs sensitive to a magnetic field. If the SWNTs have to be further purified, a specially designed oxidation method could be used to remove the remaining nickel from the SWNTs. Potential oxidation methods are described in [81-83].

2.4 Increase of cell membrane permeability by mCNT

2.4.1 Cell membrane permeability evaluation standard

The cell membrane presents most biomaterials from entering the cell cytoplasm. If material which is considered not to be able normally to pass through the cell membrane is located inside a cell, then the cell membrane is considered to be permeabilized. Although cell membrane permeability is essentially determined by the membrane's mechanical characteristics, it is usually quantified as the ratio of the desired material concentration inside and outside the cell membrane [84]. In studies of cell membrane permeability, especially in the intracellular delivery field, researchers usually focus on how many cells are permeabilized instead of how much one cell is permeabilized. To quantify how many cells are permeabilized, fluorescent materials are usually delivered through the cell membrane, since identifying their position inside the cells is relatively easy. The scientific equipment that could be used to count the fluorescent cells includes a flow cytometer, a fluorescent microscope, and a confocal microscope. In all cases, the delivery efficiency is defined as the number of fluorescent cells divided by the total number of cells counted. This number is usually expressed in a percentage. The study of the cell

membrane structure and the proper methods for increasing cell membrane permeability has a direct impact on fields like drug delivery, pharmacology and nano-toxicology.

2.4.2 Methods and materials

(a) Cell preparation

MCF-7 cells were cultured in a RPMI1640 medium supplement with 10% FBS and 1% P/S at 37^{o}C and 5% CO_2. One day before the experiment, 2×10^5 MCF-7 cells were harvested by using Trypsin-EDTA and seeded in new petri dish. On the day of the experiment, the cell confluency should reach 80%.

THP-1 cells were cultured in a RPMI1640 (11875-093, Gibco) medium supplemented with 10% fetal bovine serum (FBS) and 1% Penicillin and streptomycin (P/S) in 750mL flasks at 37^{o}C and 5% CO_2. Before the experiments, 4×10^4 THP-1 cells were harvested and resuspended in PBS. The cells were later attached onto the petri dish by using poly-L-lysine (P4832, Sigma).

KG-1 were cultured in IMDM (12440-053, Gibco) medium supplement with 20% FBS and 1% P/S in 750mL flasks at 37^{o}C and 5% CO_2. Before the experiments, 4×10^4 KG-1 cells were harvested and resuspended in PBS.

The cells were later attached onto the petri dish by using poly-L-lysine (P4832, Sigma).

(b) Delivery protocol

With the help from one research associate in our lab, the mCNTs were chemically connected with FITC. The free FITC which was not connected with mCNT might attach onto the cell membrane and induce interference when testing the fluorescent signal. To remove the free FITC, the mCNT-FITC solution was treated under dialysis for at least one day. The solution was then mixed with cells and placed on an Nd-Fe-B permanent magnet for 1*hr* at room temperature. Next, the cell petri dish was transferred from the Nd-Fe-B permanent magnet to an incubator and incubated for 3*hrs*. In the last step, the solution in the petri dish was replaced by a fresh cell culture medium. The cell culturing continued for 24*hrs*. The results were checked on the next day.

(c) FITC comparison experiments

To evaluate the FITC interaction with the cells, MCF-7 cells were chosen as a model. Because these cells are the largest among all three cell lines and have the most active endocytosis ability. The MCF-7 cells were prepared as mentioned above. 50μL FITC solutions with concentrations of 10^{-1}, 10^{-2}, 10^{-3}, 10^{-4}, 10^{-5}, 10^{-6}, 10^{-7}, 10^{-8}, 10^{-9}*mg/mL* were mixed with the

cells on the experiment day. After 1*hr* incubation at room temperature, the mixed solution was then transferred to the incubator and incubated for another 3*hrs*. The solution was then changed with a fresh cell culture medium and cultured for another 24*hrs*.

(d) Assessment of mCNT-FITC delivery efficiency and FITC comparison experiments using FACS

On the next day of the experiment, the cells were harvested and resuspended in a 300*μL* PBS solution. The mCNT-FITC delivery efficiency and FITC comparison experiments were evaluated by counting the number of fluorescent cells by using a FACSCalibur (Becton-Dickinson) at an excitation wavelength of 488*nm*.

(e) Assessment of mCNT-FITC delivery efficiency and FITC comparison experiments using fluorescent microscope

On the next day of the experiment, the cells were directly observed under a CW225A fluorescent microscope (Leica) with a DXM1200 digital camera (Nikon) under 40X magnification.

(f) Assessment of FITC comparison experiments using confocal microscope

1*mL* 2*%* paraformaldehyde (158127, Sigma-Aldrich) was employed to fix the MCF-7 cells for 2*hrs*. Next, the cell membranes were stained with

Rhodamine Phalloidin (Molecular Probes®, Invitrogen) for 40*mins*. Finally, the cell sample was flipped on a slide with the Vectashield® mounting medium with DAPI (H-1200, Vector). Confocal images were taken by using a Leica TCS SP5 II confocal microscope.

(g) Assessment of cell viability

On the next day of the experiment, MCF-7 cells were harvested by using a 0.25% trypsin solution and resuspended in a PBS solution, while the THP-1 and KG-1 cells were directly resuspended in a PBS solution. The number of viable cells was counted on a haemocytometer. The cell viability was calculated by dividing the cell number with the one in the control sample.

2.4.3 Results and discussion

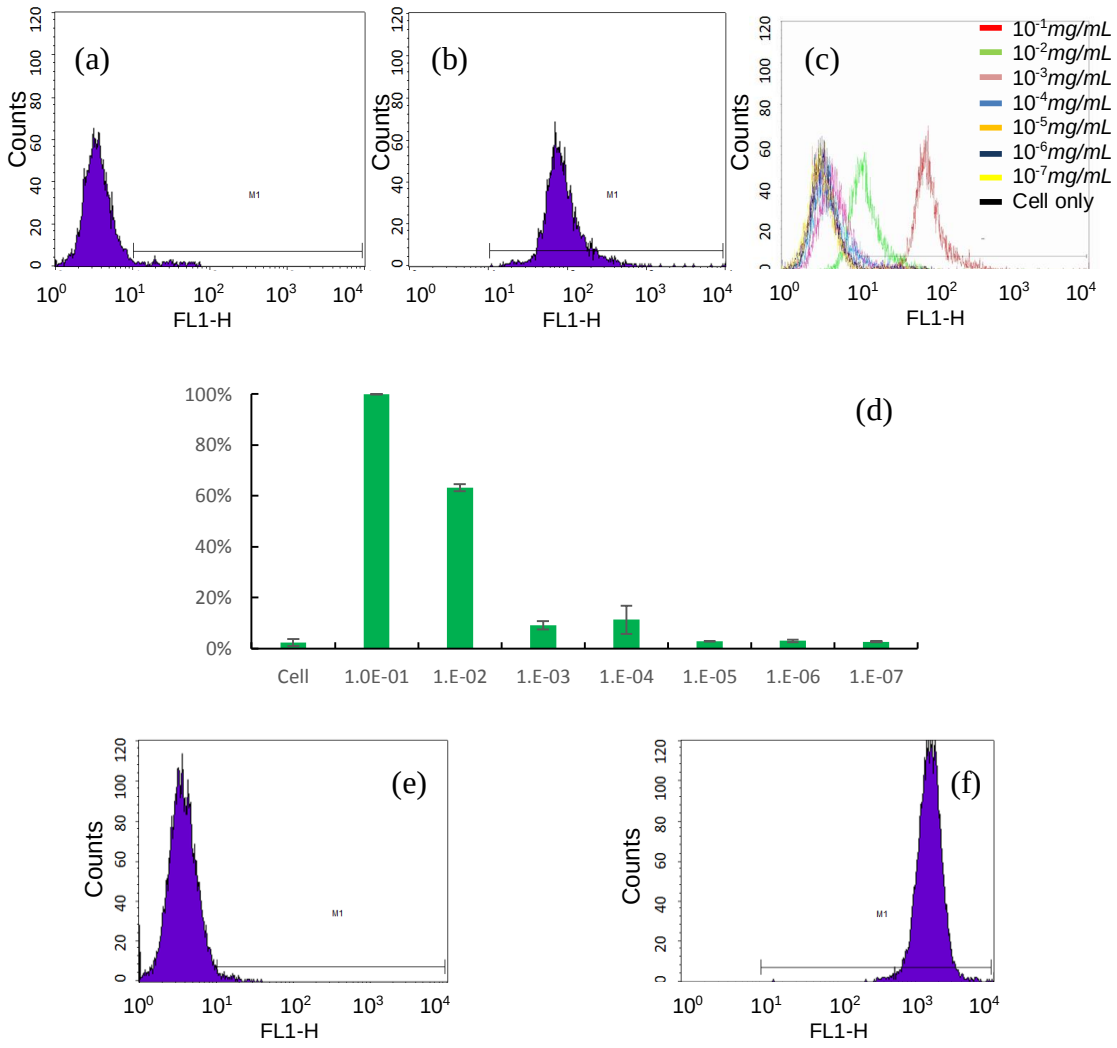

Figure 2-11 (a) FACS diagram of MCF-7 cells alone; (b) FACS diagram of MCF-7 cells with 10^{-1}*mg/mL* FITC solution; (c) FACS diagram of MCF-7 cells with different concentrations of FITC solution; (d) delivery efficiency of MCF-7 cells with different concentrations of FITC solution; (e) FACS diagram of MCF-7 cells with mCNT only; (f) FACS diagram of MCF-7 cells with mCNT-FITC solution.

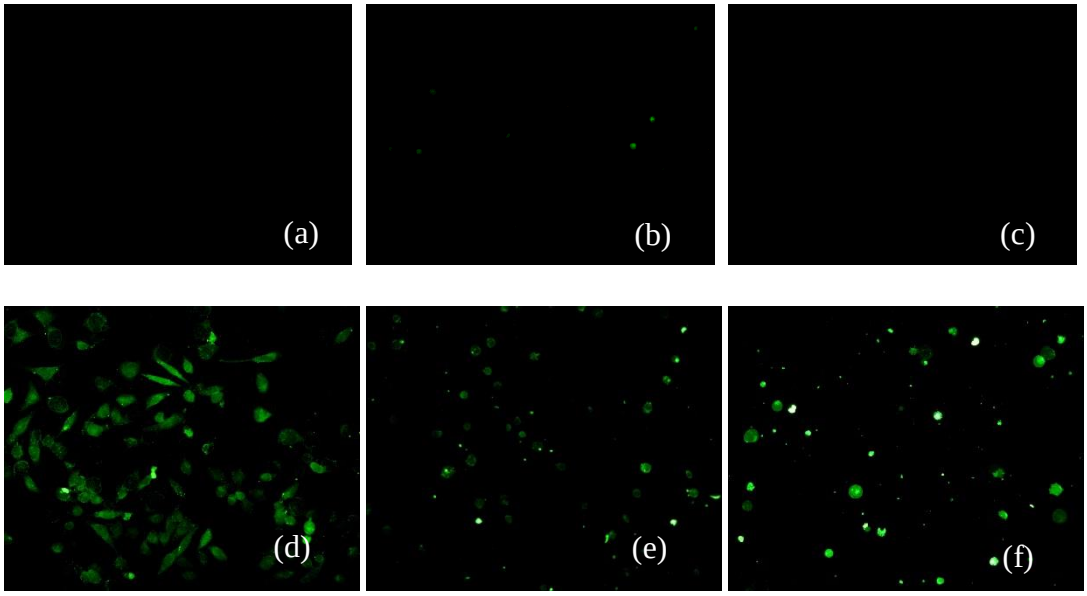

Figure 2-12 Fluorescent images of (a) MCF-7 cells alone; (b) MCF-7 cells with 10^{-1}*mg/mL* FITC solution; (c) MCF-7 cells with 10^{-7}*mg/mL*; (d) MCF-7 with mCNT-FITC; (e) THP-1 with mCNT-FITC (f) KG-1 with mCNT-FITC.

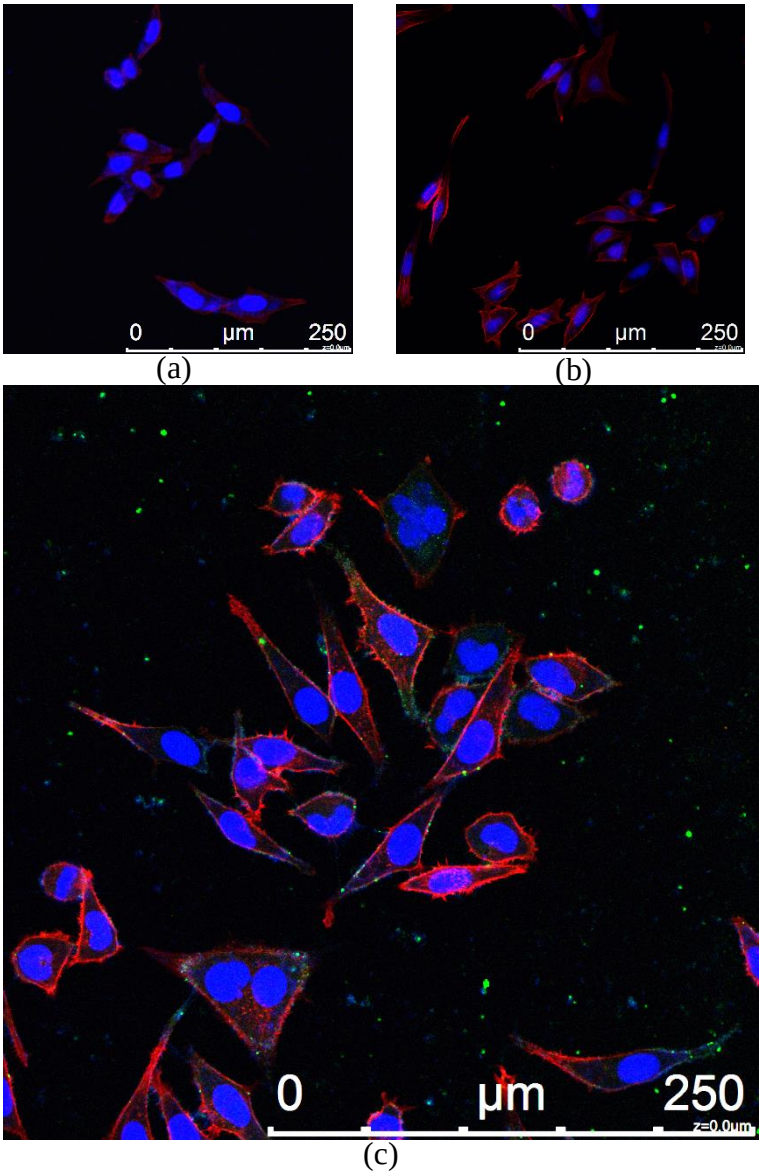

Figure 2-13 Confocal microscope image of MCF-7 cells: (a) MCF-7 cell only; (b) MCF-7 cell with 10^{-7}*mg/mL* FITC solution; (c) MCF-7 cell with 10^{-1}*mg/mL* FITC solution.

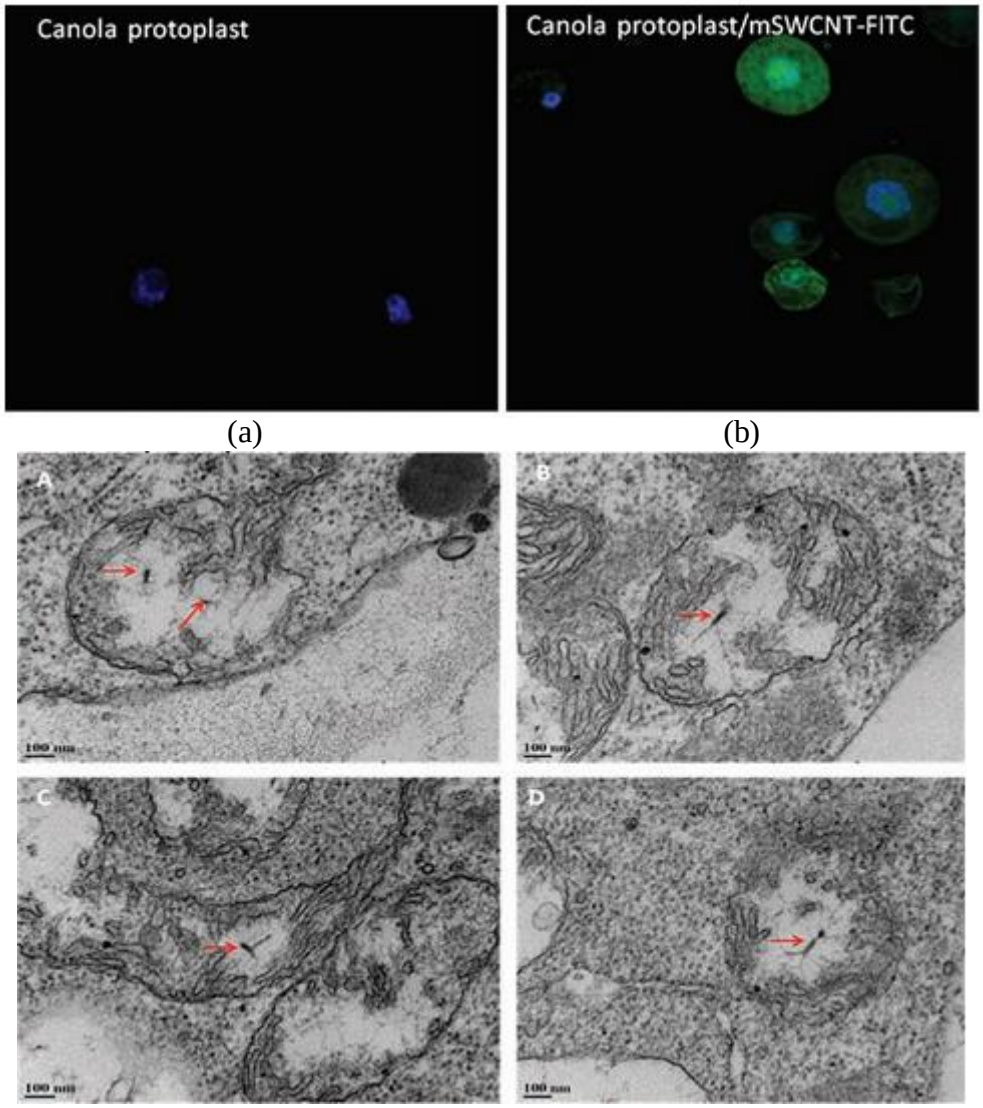

Figure 2-14 (a) and (b) Confocal microscope images of canola protoplast with mCNT-FITC; (c) Sectional TEM images of canola protoplasts with mCNT-FITC [85].

Cell lines	MCF-7	THP-1	KG-1
Cell Viability	86.4%	84%	72.6%

Table 2-1 Cell viability of mCNT-FITC on various cell lines

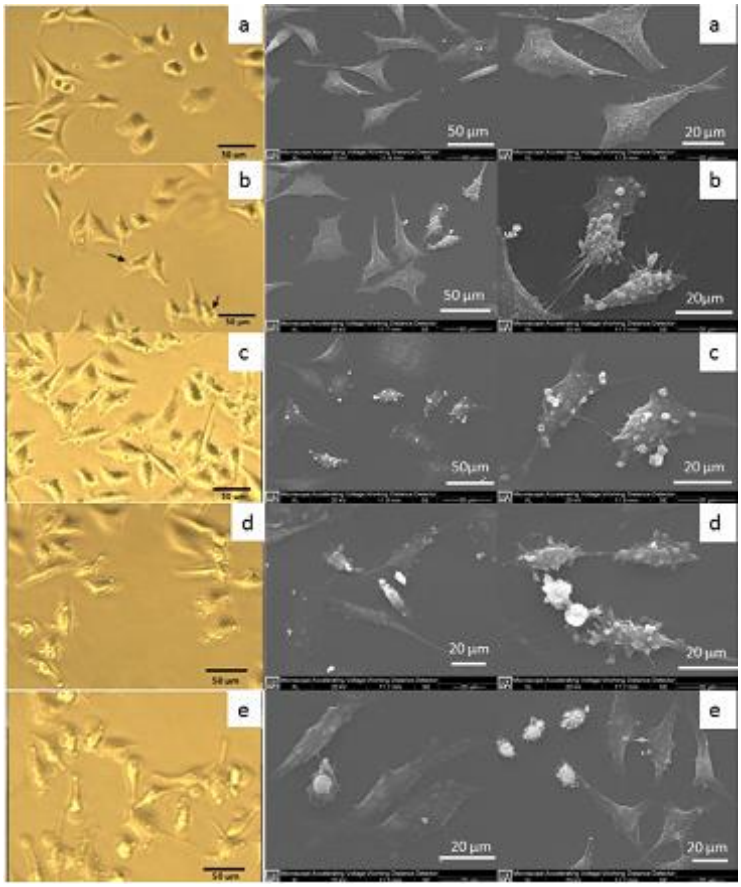

Figure 2-15 Microscope and SEM images of MCF-7 cells after incubation for different times with 0.5*mg/mL* EDC: (a) before incubation; (b) incubated for 10*mins*; (c) incubated for 20*mins*; (d) incubated for 45*mins*; (e) incubated for 210*mins* [86].

Typical FACS diagrams of the MCF-7 cells delivered with FITC are shown in Fig. 2-11. The MCF-7 cells alone (Fig. 2-11a) and MCF-7 cells with mCNT (Fig. 2-11e) give out a very low fluorescent signal, while for the sample treated with mCNT-FITC (Fig. 2-11f), the fluorescent curve shifts greatly to the high-intensity fluorescent region. When the MCF-7 cells were mixed with the FITC solution, they might also have induced a fluorescent shift as shown in Fig. 2-11b. Fig. 2-11c and Fig. 2-11d show

the FACS diagrams of the MCF-7 cells with different concentrations of FITC solution ranging from 10^{-1} to 10^{-7}*mg/mL* and the resulting fluorescent cell percentage, respectively. These figures show that the number of fluorescent cells decreases as the FITC solution concentration decreases. Even under the highest FITC concentration (10^{-1}*mg/mL*), the fluorescent intensities of the cells (Fig. 2-11e) are much lower compared to the intensity achieved with mCNT (Fig. 2-11f). This finding is also observed in the fluorescent microscope images as shown in Fig. 2-12. For the sample mixed with 10^{-1}*mg/mL* FITC solution, only a few cells show a green fluorescent signal, while for the MCF-7, THP-1 or KG-1 cells treated with mCNT-FITC, almost every cell has a green fluorescent signal. Higher-resolution images of the MCF-7 cells mixed with the FITC solution are shown in the confocal microscope image in Fig. 2-13. The cell membrane is stained in red, while the cell nucleus is stained in blue. The sample mixed with 10^{-7}*mg/mL* FITC solution is almost the same as the sample of cells only. No fluorescent color is observed. For the sample mixed with 10^{-1}*mg/mL* FITC solution, most of the green fluorescent spots are located outside the cells. Some of the green spots are located right on the cell membrane of the MCF-7 cells. It is hypothesized that although some MCF-7 cells are detected as fluorescent cells under FACS analysis, this result is due mainly to the FITC sticking or attaching onto the cell membrane, not

because of the green signal from the cell inside. Hao et al. demonstrated the ability of mCNT to penetrate the cell membrane. These researchers used the mCNT developed in this thesis to deliver FITC into canola protoplasts [85]. Based on their confocal microscope images, as shown in Fig. 2-14a and b, the mCNT efficiently delivered FITC into the canola protoplasts as a strong green fluorescent signal was detected from the inside of the cells. Based on the sectional TEM images shown in Fig. 2-14c, the mCNTs were located in the endosomes of the canola protoplasts, as pointed out by the red arrows. These sectional TEM images also indicate that the mCNT entered the cells through the cell endocytosis process.

Although the mCNTs developed are efficient when delivering the FITC, the cell numbers in the sample mixed with mCNT-FITC are much smaller compared to the numbers in the control. Because mCNT didn't show any toxicity to the cells, the decrease of cell number is due to the FITC. A later study by our group found that 1-ethyl-3-(3-dimethylaminopropyl) carbondiimide (EDC), which is a common agent for connecting CNT with small molecules like genetic materials, greatly affected cell viability by damaging the cell membrane and inducing cell necrosis [86]. As Fig. 2-15 shows, when the incubation time of EDC and MCF-7 increases, the

number and size of the pimple structures on the cell membrane also keep growing.

2.4.4 Disadvantages of the proposed mCNT method to increase cell membrane permeability

Although the mCNT method was found to effectively increase the cell membrane permeability of MCF-7, THP-1 and KG-1 cells, this method has two major drawbacks. First, as mentioned in the last section, certain toxic chemical reagents are needed to combine the molecules with mCNT, and these chemicals are very easily absorbed onto the carbon nanotube surface. Second, the mCNT will enter the cell with the delivered molecules. Since CNT is a very stable material, it will remain in the cell for a long time. Its long-term toxicity for the cell is unknown at this time. These two limitations inhibit the future application of mCNT on the human body. However, this method might be a great candidate to use in plant transformation technology.

2.5 Conclusions

An innovative purification method to extract mCNTs from purchased raw arc-discharged nanotube materials was demonstrated. The process was divided into three main procedures: SDS treatment, organic solvent treatment, and H_2O_2 treatment. To ensure that the SWNTs retained their

magnetic properties, a harsh acid treatment was avoided although it is commonly used in traditional oxidation methods. In addition, AFM-FCA combined with TEM images was applied to monitor the purification process. Our experimental results are in line with the theoretical results. The advantage of this method is that it can directly differentiate materials once the standard material analysis is performed.

The developed mCNT was tested on various cell lines. FITC was used to assist the quantification and observation of the delivery result. Based on the FACS and fluorescent images, mCNT was found to increase the cell membrane permeability of almost every cell being tested.

In summary, a new purification method and a new analysis method which is efficient and reliable for this mCNT purification process were proposed in this Chapter. The developed mCNTs were capable of increasing the cell membrane permeability.

Chapter 3

III. Development and analysis of microbubble-assisted high centrifugation field for increasing cell membrane permeability

3.1 Introduction

3.1.1 Physical-based methods to increase cell membrane permeability

As the name suggests, physical-based methods utilize temporary physical stimulations on the cell membrane to create intracellular pathways into the cell cytoplasm. The reported methods include electroporation, laser beam gene transduction, sonoporation, gene gun and liquid jet injection.

Electroporation is a technique which increases cell membrane permeability by utilizing a controlled voltage (typically 200*mV*-1*V*) on the cell membrane [87]. The electrical voltage stimulation has been found to

temporarily produce transient holes on the cell membrane if the electrical voltage is applied in a short duration within a limited value [88, 89]. Wegener et al. reported that if the electric field magnitude applied did not exceed a threshold, the cell surface eventually recovered through the cells' self-repairing mechanism [90]. However, this recovery stage usually has a longer duration (on a time-scale of seconds) compared to the pore formation stage (on a time-scale of 10*ns*) [91, 92]. After intracellular pores are temporarily formed, biomaterial such as pDNA can diffuse into the cytoplasm [93, 94]. The geometric size, shape, and electric charge of the biomaterial are all key factors relating to the transport efficiency [95]. Electroporation is very effective on many cell lines including those with extremely low endocytosis ability [96]. Electroporation is particularly useful for delivering biomaterials to superficial areas, but invasive surgical procedures are required to deliver biomaterials to specific organs [3]. Kamary et al. found that Easy Vax™, a clinical electroporation system, was safe and tolerated when administered to adults [97], while Thomson et al. used electroporation to treat patients with liver cancer. No damage to the healthy organs was found during the treatment [98].

Laser beam gene transduction (LBST) utilizes short laser pulses to stimulate the cell membrane. The increased cell membrane permeability achieved by LBST is comparable that achieved by electroporation [99], but

the side-effect is much smaller compared to that from electroporation [3]. However, to precisely control a laser beam, large and specific equipment is needed. This limitation has discouraged the development of this technology.

Sonoporation is defined as the transient increase of cell membrane permeability and delivery of extracellular biomaterials into cells with the assistance of ultrasound [100]. The use of ultrasound to help deliver biomaterials into cells can be dated back to 1992 [101]. Since then, this topic has generated great interest among researchers. Later researchers found that microbubbles, which are an agent usually used for ultrasound imaging, could greatly enhance the delivery efficiency [102]. The mechanism of sonoporation is not clear. Some researchers have claimed that in the ultrasound field, the movement of microbubbles initiates the endocytosis of cells, while others consider that the cavitation effect increases the cell membrane permeability. The cavitation effect of microbubbles can be classified into stable cavitation and inertial cavitation. In stable cavitation, the microbubbles periodically expand and contract. This process generates microstreaming around the cell membrane nearby. Microstreaming has been found to be one of the causes of the increase in cell membrane permeability [103]. In inertial cavitation, the microbubbles burst and result in liquid jets, which can create pores up to 16μm on the

cell membrane [104]. Although both mechanisms increase cell membrane permeability [105-107], the stable cavitation effect is considered to be more harmless as the pores formed under stable cavitation are recoverable [108]. For application focusing on inertial cavitation, researchers are trying to increase the delivery efficiency while reducing the lethal effect. Significant progress has been made on the ultrasound signal generation stage. It was found that the critical parameters include frequency, duty cycle, intensity and ultrasound duration [109]. Sonoporation is another effective method for cell lines with low endocytosis ability. Compared to electroporation, sonoporation is better focused and capable of penetrating into deeper regions. Taniyama et al. reported that clinical angiogenetic gene therapy using plasmid DNA gene transfer was attempted in patients with peripheral artery disease. However, the Phase III clinical trial did not show sufficient efficiency [110].

Gene gun and liquid jet injection share almost the same mechanism. A gene gun uses “bullets” to shoot the cells. Usually, the bullets are gold nanoparticles coated with biomaterial [111]. The impact force is so large that even a plant cell wall can be deeply penetrated. Thus, the gene gun is widely used for plant cell transformation [112]. In liquid jet injection, the “bullet” is liquid. To perform liquid jet injection, one has to first dissolve biomaterial in a very small volume of liquid and then inject the solution into

the cell at high pressure [3]. Compared with the other physical-based methods, the gene gun and liquid jet injection can target only very small areas. Thus, the total number of cells treated at one time is limited [3].

Overall, the physical-based methods deliver biomolecules by actively inducing real-time transient cell membrane damage. Thus, they are more applicable than other methods for universal cell-lines. Physical-based methods usually involve expensive equipment. However, once the appropriate equipment is purchased, the continuing cost of physical-based methods is relatively cheaper than that of chemical-based methods.

3.1.2 Centrifugation on cells

Centrifugation is a normal technique used almost in every bio-lab around the world. In microbiology and cytology studies, one typical example is using the differential centrifugation to collect and separate certain organelles from whole cells [113]. Since the cell organs have variable densities, similar organs accumulate in certain regions during the centrifugation process, thus differentiating themselves from the others. A similar mechanism can be applied to separate CNTs or microbubbles [114, 115]. For animal cells, centrifugation is used mainly for collection purposes. As a rule of thumb, the centrifugation of cells should never exceed 2000*RPM (447g)* if the purpose is to collect the cells. Hoffman et al. used

a high- speed camera to observe cell morphology change at high centrifugation speeds [116]. At 11,000*RPM*, the cells totally changed from a round morphology to a spindle-like shape. When the centrifugation speed was decreased to 200*RPM*, most of the cells returned to their usual round morphology [116]. Richter et al. centrifuged the Xenopus oocytes at 10,000*g* for 5*mins* and detected the electrophysiological properties of cells after centrifugation. It was found that the cell membrane resistances were preserved if the centrifugation did not exceed 10,000*g* for 5*mins* [117].

3.1.3 Background of microbubbles

3.1.3.1 Microbubble history

The discovery of microbubbles' application on ultrasound imaging can be traced back to 1960. Since a normal liver, spleen, or kidney has similar acoustic properties to those of many tumors, ultrasound alone has great difficulty differentiating between healthy and diseased tissue [118]. Some researchers accidently increased the ultrasound image contrast after injecting fluids like saline into a patient's blood [119]. However, the duration of this increase effect was very short. Later on, researchers found that a patient's blood, which usually contains serum albumin, could also increase the duration of the image contrast enhancement [120]. Further investigation showed that the increase of the temporary image contrast

was due to the small-scale air bubbles, such as microbubbles, in the liquid. Microbubbles, as the name indicates, are gas bubbles stabilized by surfactant or lipid materials at the micro-scale. The high compressibility and non-linear response to an unstable pressure environment caused by ultrasound enable microbubbles to better scatter ultrasound and distinguish themselves from the surrounding tissue [121]. The ultrasound response closely relates to the microbubble size, shell material and shell thickness [122]. The first commercialized ultrasound contrast agent, Albunex®, is normal gas microbubbles capsulated by albumin. This agent increases the image contrast, but is not stable enough to be consistent in the pulmonary passage [100], because in the human body, the important properties for the stability of microbubbles, such as viscosity, temperature, and hydrostatic pressure, differ from those in an *in-vitro* environment [100]. To make microbubbles more stable in the body, researchers focused on choosing suitable materials for the microbubbles' shell and microbubble gas. Shell-coating materials such as phospholipids, polymer-protein bilayer, and palmitic acid were found to be better than albumin [123]. Microbubble shell materials can be classified into hard materials and soft materials. Both are intended to form special structures to counter the Laplace pressure formed in the gas core [124]. Although the special shell structure material greatly increases microbubble stability, the gas core is

still important. For example, both Optison™ and Albunex® use albumin as the microbubble shell, but the former microbubble with an inner gas core of octafluoropropane is much more stable than the latter one with air. Because any gas continuously diffuses outwards from a microbubble. This process, as Kabalnov et al. pointed out, is determined mainly by the diffusivity of the gas in the surrounding liquid [125]. As the diffusivity of air into saline water is much higher than that of octafluoropropane, microbubbles with air as the gas core will shrink faster and finally collapse earlier. For a $2\mu m$ microbubble composed of normal air, the air fully dissolves into water after $8ms$, while a perfluoropropane microbubble needs $90ms$ to finish this process and a decafluorobutane microbubble needs $900ms$ under the same condition [126]. Today's commercialized ultrasound contrast agents all choose gas with low solubility in water or blood as the gas core of microbubbles.

3.1.3.2 Microbubble manufacture methods

Microbubbles can be manufactured in many ways. One of the most commonly used methods is sonication or mechanical agitation [127-129]. The coating solution is sonicated or agitated while the filling gas is floating above the solution surface. The gas is first emulsified in the solution, then the coating material will sediment on the gas liquid interface to stabilize the microbubble. If the sonication method is used to manufacture

microbubbles, the size of the microbubbles generated depends on the frequency, power and duty cycle of the ultrasound [130]. Usually, the formed microbubbles are in a broad range of sizes, but a filtering process can be used to obtain microbubbles of a desired size [131].

Another method for manufacturing microbubbles is membrane emulsification. This method produces microbubbles by forcing the material solution repeatedly through a porous membrane [132]. Microbubbles produced by this method have a narrower range of size distribution than those produced by using other methods [133]. In this process, the characteristics of the membrane such as pore size, stiffness, and wettability are key for making the microbubbles stable and mono-dispersed [134].

Microfluidic devices are also used to prepare microbubbles. The two main types of microfluidic devices for bubble preparation are a flow-focusing unit produced by MEMS manufacture techniques and a T-junction device assembled by using several capillaries [135-137]. By controlling the solution flow rate and gas flow rate, a liquid jet is formed. The jet pinches-off at a certain distance from the orifice, resulting in the formation of microbubbles [138]. This method can produce highly mono-dispersed microbubbles of an almost identical size, but the production rate is very low. The size of the microbubbles produced is also relatively larger than

that of the ones produced by the other methods mentioned above [123]. Microbubbles of a size around 2-5μm now can be manufactured by using a novel configured microfluidic device [139].

3.1.4 Basic intermolecular force review

3.1.4.1 VDW force between molecules

The VDW force is the sum of the attractive or repulsive forces between molecules (or between parts of the same molecule) other than those due to covalent bonds, the hydrogen bonds, or the electrostatic interaction of ions with one another or with neutral molecules or charged molecules [140]. This force can be generally divided into three categories: (1) the force between two permanent dipoles, known as the Keesom force; (2) the force between a permanent dipole and a corresponding induced dipole, known as the Debye force; and (3) the force between two instantaneously induced dipoles, known as the London dispersion force [72]. To evaluate the VDW force between different surfaces, Hamaker proposed that the VDW interaction forces between pairs of atoms are additive. Hamaker constant A_H is thus defined as Eq. 3-1[72]:

$$A_H = \pi^2 C_{AB} \rho_A \rho_B, \tag{3-1}$$

where C_{AB} is the coefficient in the particle-particle pair interaction, while ρ_A, ρ_B are the atom number densities of materials A and B. However, this additive assumption is not accurate, because it ignores the influence of neighboring atoms on the interaction between any pair of atoms. The accurate calculation of the VDW force can be obtained by treating the material as continuous media as described in the Lifshitz theory. Interestingly, the VDW force calculated from the Lifshitz theory is very similar to the one calculated from the Hamaker additive assumption, except for how the Hamaker constant is calculated. The Lifshitz theory predicts the accurate Hamaker constant based on the materials' dielectric constant ε and reflective index n. The equation is given as

$$A_{123} \approx \frac{3}{4} kT \left(\frac{\varepsilon_1 - \varepsilon_2}{\varepsilon_1 + \varepsilon_2}\right)\left(\frac{\varepsilon_3 - \varepsilon_2}{\varepsilon_3 + \varepsilon_2}\right) + \frac{3h\nu_e}{8\sqrt{2}} \frac{(n_1^2 - n_2^2)(n_3^2 - n_2^2)}{\sqrt{(n_1^2 + n_2^2)(n_3^2 + n_2^2)}\left(\sqrt{n_1^2 + n_2^2} + \sqrt{n_3^2 + n_2^2}\right)} \quad (3\text{-}2)$$

Where "1" and "3" denote two interacting bodies inside medium "2". Based on the theory mentioned above, the interaction energy between two plane surfaces is calculated by using Eq. 3-3. The VDW force is equal to the derivative of the interaction energy, as in Eq. 3-4 [72]:

$$W_{plane-plane}(D) = -\frac{A_H}{12\pi D^2} \quad (3\text{-}3)$$

$$F_{plane-plane}(D) = -\frac{dW_{plane-plane}(D)}{dD}. \quad (3\text{-}4)$$

If the value of Eq. 3-4 is positive, then the VDW force is attractive between the two plane surfaces. If it is negative, the VDW force is repulsive. The VDW force between two sphere surfaces can be calculated by using the Derjaguin approximation. In the Derjaguin approximation, the VDW force between spherical surfaces can be related to the interaction energy between two planes with a factor of $2\pi\left(\frac{R_1R_2}{R_1+R_2}\right)$. Thus, the VDW force between two sphere surfaces is obtained as in Eq. 3-5 [72]:

$$F_{sphere-sphere}(D) = 2\pi\left(\frac{R_1R_2}{R_1+R_2}\right)W_{plane-plane}(D) = -\frac{A_H}{6D^2}\left(\frac{R_1R_2}{R_1+R_2}\right). \quad (3\text{-}5)$$

3.1.4.2 Electric double layer force

When a plane is immersed in a liquid, the plane's surface is usually charged. The charged surface might due to the dissociation of ionic groups of the surface molecules into the liquid or the adsorption of the ionic groups in liquid onto the surface. This process forms the first electric layer. This charged surface will also attract ions with the opposite sign (named counter ions) onto its surface and form another charged layer, but with the opposite sign. These two layers are thus named electric double layers. To model the electric double layers' status in a liquid, two models are generally proposed. The first model is the Helmholtz model, in which,

the attracted counter ions on the second layer equally cancel all the surface charges on the first layer. Thus, the electric double layers can be modeled as a capacitor. The length between the middle lines of the two charged layers is defined as the gap distance of the equivalent capacitor. The electric potential drops linearly from the middle line of the first charged layer to the middle of the second charged layer. An obvious disadvantage of this model is that it neglects the thermal motion of the counter ions, especially for the ones near the second layer boundary [141]. The second model is the Gouy-Chapman model. Compared to the Helmholtz model, this model is closer to the real world because of the consideration of the ions' thermal motions. As the distance from the surface increases, some of the counter ions are not firmly attracted to the charged surface. Due to their thermal motion, they are free to diffuse in and out of the ambient medium. As a result, the amount of counter ions on the second layer is generally smaller than the total amount of charges on the first layer; thus, the counter ions cannot totally neutralize the surface. This phenomenon creates a region named the diffuse layer [142, 143]. The potential along with the distance from the surface decays with an exponential $1/\kappa$, which is called the Debye length. It regulates the exponential decaying speed. The physical meaning of the Debye length can be considered as the boundary beyond which the concentration of the counter ions is almost the

same as that in a bulk solution. Adding extra materials into the solution or changing the medium concentration can modify the Debye length of the medium or the charge density on the surface. Since the Derjaguin approximation can be also applied to estimate the electric double layer force, once the medium is determined, for two charged sphere surfaces, the electric double layer interaction force between spheres “1” and “3” in a medium “2” can be calculated as in Eq. 3-6 and Eq. 3-7:

$$W_{plane-plane}(D) = 2\varepsilon_0\varepsilon_2\kappa\psi_1\psi_3 e^{-\kappa D} \tag{3-6}$$

$$\begin{aligned} F_{sphere-sphere}(D) &= 2\pi\left(\frac{R_1R_2}{R_1+R_2}\right)W_{plane-plane}(D) \\ &= 4\pi\left(\frac{R_1R_2}{R_1+R_2}\right)\varepsilon_0\varepsilon_2\kappa\psi_1\psi_3 e^{-\kappa D} \end{aligned}, \tag{3-7}$$

where ψ_1 and ψ_3 are surface potentials; $1/\kappa$ is the Debye length; ε_0 and ε_2 are the vacuum dielectric constant and relative dielectric constant.

3.1.4.3 Derjaguin-Landau-Verwey-Overbeek (DLVO) force

The DLVO force describes the interaction force between the charged surfaces in a liquid medium and contains two components, the VDW force and the electric double layer force. As the VDW force will always be attractive between similar molecules, the electric double layer force helps disperse the particles in the solution. When the electric double force becomes weaker, the particles tend to accumulate together, thus breaking

the balance of the solution. This result is very important, especially when the two charged surfaces are separated by only a small gap.

3.1.5 Work description

In this chapter, a method to increase cell membrane permeability by combining the centrifugation and microbubbles as shown in Fig. 3-1 is discussed. It is well known that a cell membrane is composed mainly of a lipid bilayer. The flexibility of the cell membrane is due largely to this structure. Because of the cell membrane flexibility, cell morphology changes in high-speed centrifugation fields [116]. This morphology change might be due to a squeezing effect. The changes in shape for most cells are reversible, and the membrane properties remain the same. The cells that adopt special morphologies during the centrifugation process will be discussed in this chapter. The mechanisms of sonoporation in opening the pores on the cell membrane are known to be related to the cavitation effect due to the bursting of the microbubbles [105-107, 144, 145].

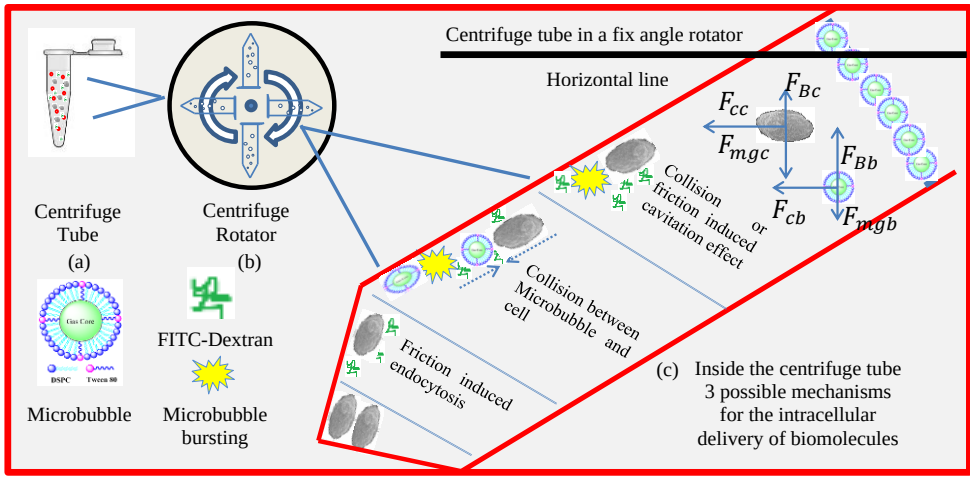

Figure 3-1 Schematic of microbubble-assisted high centrifugation field to enhance the cell membrane permeability: (a) 1.5*mL* centrifuge tube contains FD, microbubbles and cells; (b) centrifuge tube allocation in a centrifuge rotator; (c) the material motion inside the centrifuge tube. Three possible mechanisms for the intracellular delivery of biomolecules are proposed and illustrated in the separated regions.

In addition, the cells and microbubbles moving towards each other in a centrifuge tube have unavoidable collisions. Therefore, the delivery efficiency of extracellular molecules in centrifugation fields of varied strengths and different amounts of microbubble solutions is explored in this chapter. FD (40*kDa* and 70*kDa*) is normally used as membrane-impermeable biomolecules [146]. It also has a unique advantage. For instance, FD, as a fluorescent tag, can visibly trace its location inside the cells. This study focus on mammalian cell platform by choosing THP1-cells as a model for the suspension cells, while MCF-7 cells were used as a model for the adherent cells. A simplified model was built to simulate the interaction between the microbubbles and cells. The results indicated that

the relative velocity between the cells and microbubbles was related to the centrifugation field and that this velocity was critical for the increase in cell membrane permeability.

3.2 Microbubble preparation and detection

3.2.1 Microbubble preparation

1, 2-Distearoyl-sn-glycero-3-phosphocholine (DSPC) (850365P, Avanti Polar Lipids) and Tween-80 (P1754, Sigma-Aldrich) were dissolved in chloroform (288306, Sigma-Aldrich) at a ratio of 10:1 (w/w). The solution was then processed in a rotary evaporator (LABOROTA 4000, Heidolph) to form a thin film. PBS buffer (14190-250, Gibco) was added into the vial afterwards to hydrate the thin film. The solution was stirred at 60^{o}C for 2.5*hrs*. The solution at this point could then be stored at -20^{o}C for further processing. For application, in the final step, glycerol (G5516, Sigma) was added to the solution with a ratio of 1:1 (v/v), and the mixture was then stirred at 60^{o}C for another 1.5*hrs* to form the microbubble solution. To activate the microbubbles, the microbubble solution was transferred into a 1.5*mL* centrifuge vial, which was activated on Vialmix® for 45 seconds. To label the microbubbles with fluorescence, a 20μL FITC solution (46950, Fluka) was added into the microbubble solution. After activation, the fluorescent microbubble image was observed by using a CW225A

fluorescent microscope (Leica) with a DXM1200 digital camera (Nikon) under 40X magnification. To observe a microbubble image under a bright-field, 10*μL* of activated microbubble solution was transferred to a haemocytometer and observed under an AE31 microscope (Motic) with 20X magnification. To measure the size of the microbubbles, a 100*μL* activated microbubble solution was diluted into a 50*mL* beaker and passed through a 20*μm* aperture to obtain size distribution information by using a Multisizer™3 Coulter Counter®. The microbubble size was also determined by using the dynamic light scattering technique (DLS). After activating, 100*μL* microbubble solution was diluted into 10*mL* DI water. Then the solution was measured by using ZetaSizer NanoZS (Malvern).

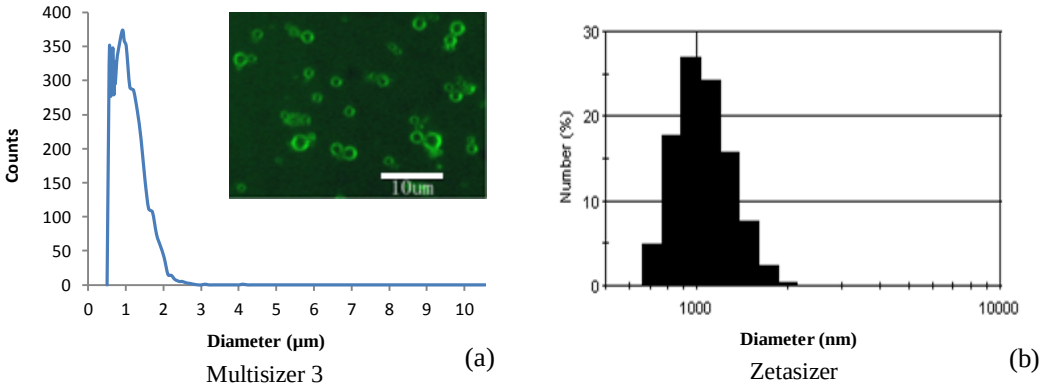

Multisizer 3 (a) Zetasizer (b)

Figure 3-2 Morphology and size distributions for activated microbubbles: (a) microbubble size distribution measured by using Multisizer™3, in the top-right corner, an image of fluorescent microbubbles observed under fluorescent microscope is presented; (b) microbubble size distribution measured by using ZetaSizer.

3.2.2 Microbubble detection - morphology and size distribution

The microbubbles were marked by FITC and observed with a fluorescent microscope. The result is shown in the top-right corner of Fig. 3-2a. The microbubble shell was stained with a bright fluorescent green color, while the dark region inside the microbubbles was composed mainly of air. The particles' size distribution measured by using the ZetaSizer and Multisizer 3 ranges from 500*nm* to 3*μm* diameter (Fig. 3-2). For the Multisizer 3, since the measurement was performed under a 20*μm* aperture with a proper measurement range from 0.4-12*μm*, the microbubble size distribution curve was cut off at around 500*nm*. Although the Multisizer utilizes electrical impedance sensing of the volume of electrolytes displaced by a microbubble as it passes through an orifice [115], while the ZetaSizer measures size based on the dynamic light scattering induced by the particles' random motion, the measurement results are very similar. Both of the size distribution measurement results show a peak value of around 1*μm*.

3.3 Experimental methods

3.3.1 Cells preparation

THP-1 cells were cultured in a RPMI1640 (11875-093, Gibco) medium supplement with 10% FBS and 1% P/S in 750*mL* flasks at 37*ºC* and 5% CO_2. The cells were harvested and resuspended in PBS for the subsequent experiments.

MCF-7 cells were cultured in a RPMI1640 medium supplement with 10% FBS and 1% P/S at 37*ºC* and 5% CO_2. The cells were harvested by using Trypsin-EDTA and resuspended in PBS for the subsequent experiments.

3.3.2 Cell membrane permeability enhancing protocol

The THP-1 cells were harvested and resuspended in 800*μL* PBS at a concentration of 7.5×10^5 *cells/mL* in each 1.5*mL* centrifuge tube. The MCF-7 cells were harvested by using Trypsin and resuspended in 800*μL* RPMI 1640 without FBS and P/S at a concentration of 5×10^5 *cells/mL* in each 1.5*mL* centrifuge tube. A 15*μL* 5*mg/mL* FD (40*kDa*) solution (FD40S, Sigma-Aldrich) or 15*μL* 2.5*mg/mL* FD (70*kDa*) and the microbubble solution were in turn added to the cell suspension individually. The influences of the microbubble-assisted high centrifugation field parameters on the cell membrane permeability were studied at various centrifuge

speeds (expressed in relative centrifugal force (RCF)) and volumes of microbubble solution. In each case, the cell mixture was centrifuged at 4^{o}C with the designed parameters (Allegra™ 25R centrifuge, rotator: TA-15-1.5, Beckman Coulter). The varied ranges for the centrifuge speeds and volumes of microbubble solution were 252g (1500RPM) to 9056g (9000RPM) for THP-1, 28g (500RPM) to 2795g (5000RPM) for MCF-7, and 5 to 85μL for both of the cell lines, respectively. The RCF was calculated based on Eq. 3-8, where g is the earth's gravitational acceleration; r is the rotational radius; and N is the rotations per second:

$$RCF = \frac{r\pi^2 N^2}{900g}. \tag{3-8}$$

The cell control sample was centrifuged in the same way as other samples, but without microbubbles. After exposure to the microbubble-assisted high centrifugation field, the cells were washed three times by centrifuging at 4^{o}C with 7155g (8000RPM) for 10$mins$ in PBS and then collected. The delivery efficiency of FD was directly evaluated by using a FACSCalibur (Becton-Dickinson). For the cell viability evaluation, the THP-1 and MCF-7 cells were cultured for 24hrs and then underwent colorimetric assays. For the confocal microscope investigation, all of the cells were immobilized, dehydrated and stained onto a slide and investigated. For SEM

assessment, all the samples were immediately dehydrated, coated and assessed.

3.3.3 Assessment of FD delivery efficiency

After the washing step, the cells were resuspended in a 300*μL* PBS solution. The FD delivery efficiency was evaluated by counting the number of fluorescent cells with a FACSCalibur (Becton-Dickinson) at an excitation wavelength of 488*nm*.

3.3.4 Assessment of cell viability

A colorimetric assay is a technique used to determine the concentration of colored compounds in a solution [147]. By mixing the MTS and MTT solutions with the THP-1 and MCF-7 cells, the active reductase enzymes located inside the cells convert the MTT and MTS dyes to formazan dyes, giving a purple color. As a result, a sample with high viable cell number produces more formazan dye and has a darker color. By measuring the absorption of the formazan solution under a certain wavelength, the relative cell number can be identified. After 24*hrs'* incubation, the THP-1 and MCF-7 cells were harvested and resuspended in a PBS solution. A 100*μL* THP-1 PBS suspension was mixed with a 100*μL* RPMI1640 supplement with 10% FBS and a 10*μL* MTS solution in each well of 96 plates. The plates were then incubated for 3*hrs*. The plates were read in a

96-plate reader (BioTek, ELx800) at a wavelength of 490*nm*. For the MCF-7 cells, a 1*mL* MTT solution was added into the petri dish and incubated for 3*hrs*. Next, the supernatant was replaced with 1*mL* DMSO. All the samples were left to stay for 10*mins* in order to completely dissolve the formed formazan salts. Then, 200*μL* solution was transferred into each well of 96-plate and the plate was read under a 96-plate reader at a wavelength of 550*nm*. The cell viability number was calculated by dividing the number of absorbance of cells treated with microbubbles by the number of absorbance of cells without microbubbles treatment.

3.3.5 Investigation of FD location inside cells with confocal microscope

To investigate the FD location inside the cells, they were imaged with a confocal microscope. After the exposure to the microbubble-assisted high centrifugation field, the THP-1 and MCF-7 cells were resuspended in PBS and attached to the coverslip by using poly-L-lysine (P4832, Sigma). Then 1*mL* 2% paraformaldehyde (158127, Sigma-Aldrich) was employed for 2*hrs* to fix the cells. Next, the cell membranes were stained with Rhodamine Phalloidin (Molecular Probes®, Invitrogen) for 40*mins*. Finally, the cell sample was flipped onto a slide with the Vectashield® mounting medium with DAPI (H-1200, Vector). Confocal images were taken by using a Leica TCS SP5 II confocal microscope.

3.3.6 Evaluation of cell membranes by using SEM

To evaluate the microbubble-assisted high centrifugation field's effect on the cell membranes, THP-1 cells were prepared as mentioned above and centrifuged with 9056*g* (9000*RPM*) plus a 45*μL* activated microbubble solution. After the experiment, the THP-1 cells were collected and attached to the plates by using poly-L-lysine. The cells were then fixed in 2*%* glutaraldehyde in a 4*%* PEA*/* cacodylate buffer for 2*hrs* at room temperature. A graded ethanol series (50, 70, 90 and 100*%*) and a graded mixture series of ethanol and hexanethydisilazane (HMDS) (75:25, 50:50 and 25:75) were used to dehydrate all the samples. After the dehydration process, the cells were kept overnight in 100*%* HMDS at room temperature until a HUMMER 6.2 sputtering system was used to coat them with gold-palladium. The SEM images were taken by an XL 30 SEM (Philips) operated at 20*kV*.

3.4 Results

3.4.1 The influence of centrifugation speed and volume of microbubble solution on the enhancement of cell membrane permeability and cell viability of THP-1 and MCF-7 cells

The influence of the centrifugation speed and the volume of the microbubble solution on cell membrane permeability and cell viability was determined by using various centrifugation speeds and different volumes of microbubble solution. As previously mentioned, FD is a commonly used marker for increases in membrane permeability [146].

Fig. 3-3 shows a typical FACS diagram of THP-1 cells under treatment. Based on the result, the THP-1 cells centrifuged alone show a very low fluorescent background, while the sample centrifuged with FD40*kDa* shows a slight shift to the right, possibly because some of the FD40*kDa* attached onto the THP-1 cell surface. For the sample centrifuged with FD40*kDa* and microbubbles, the THP-1 cells have a very strong fluorescent signal, and the peak of the fluorescence curve shifts greatly to the right. This phenomenon means that for the THP-1 cell centrifuged with

microbubbles and FD40*kDa*, the fluorescent signal was retained even though several washing steps had been performed.

Fig. 3-4a-d shows the delivery efficiency and cell viability of THP-1 cells under varied centrifugation speeds and volumes of microbubble solution. During the evaluation of the effect of the centrifugation speed, the volume of the microbubble solution was set at 45*μL*. Fig. 3-4a shows that the delivery efficiency increases with the increasing of the centrifugation speed. Although the delivery efficiency increases slightly from 23.4*%* to 37.5*%* ($p<0.05$) when the centrifugation speed increases from 252*g* (1500*RPM*) to 1006*g* (3000*RPM*), the efficiency increases significantly to 71.4*%* ($p<0.05$) when the solution is treated under 2795*g* (5000*RPM*).

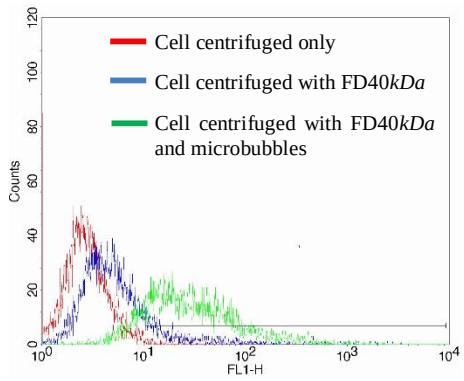

Figure 3-3 A typical FACS diagram of the THP-1 cells under treatment. The red curve stands for THP-1 cells centrifuged alone. The blue curve stands for THP-1 cells centrifuged with FD40*kDa*, while the green curve stands for THP-1 cells centrifuged with FD40*kDa* and microbubbles.

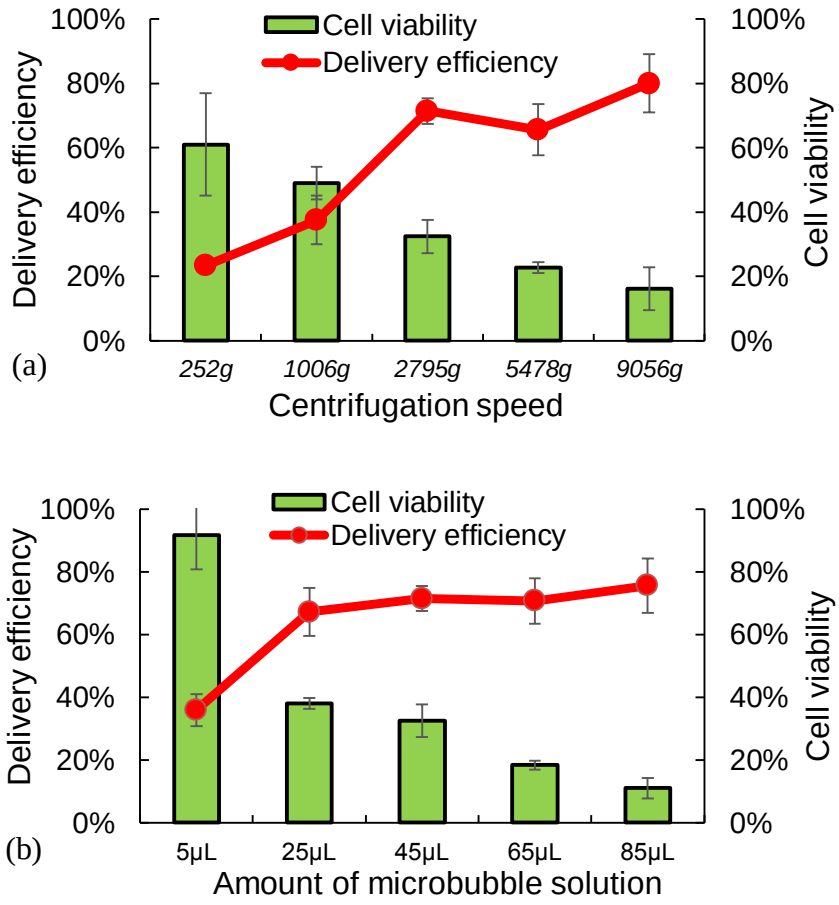

Figure 3-4 FD delivery efficiency and cell viability of THP-1 cells: (a) delivery efficiency of FD40*kDa* (the red curve) and cell viability (the green bar) of THP-1 cells at different centrifugation speeds, microbubble solution is set at *45μL*; (b) delivery efficiency of FD40*kDa* (the red curve) and cell viability (the green bar) of THP-1 cells with different volumes of microbubble solution, centrifugation speeds is set at 2795*g*.

Meanwhile, the cell viability (the green bar) continues to drop with the increasing of the centrifugation speed. The lowest cell viability occurs at 9056*g* (9000*RPM*), which is only 16.2%. To investigate the effect of the volume of microbubble solution on delivery efficiency and cell viability, the

centrifugation speed was set at 2795*g* (5000*RPM*). Starting from a 5*μL* microbubble solution, as Fig. 3-4b shows, the delivery efficiency (red curve) increases from 35.9% to 67.1% and then reaches a plateau of around 70% with 45, 65 and 85*μL* of microbubble solution being used. The cell viability (Fig. 3-4b, the green bar) exhibits a decreasing trend when the volume of the activated microbubble solution increases from 5 to 85*μL*.

The influences of the centrifugation speed and the volume of microbubble solution on cell membrane permeability and cell viability of MCF-7 cells were investigated in a similar way as that used for the THP-1 cells. Typical FACS diagrams of the MCF-7 cells under treatment are shown in Fig. 3-5. Based on the FACS image, the fluorescent signal shifts greatly only when the MCF-7 cells are centrifuged with microbubbles. Both FD40*kDa* and FD70*kDa* were exploited to evaluate the increase in cell membrane permeability. In Fig. 3-6a, the delivery efficiency of FD40*kDa* is presented by the red curve while the delivery efficiency of FD70*kDa* is shown by the blue curve. In both conditions, the delivery efficiency shows an increasing trend as the centrifugation speed increases. This result is similar to the result obtained for the THP-1 cells (Fig. 3-4a).

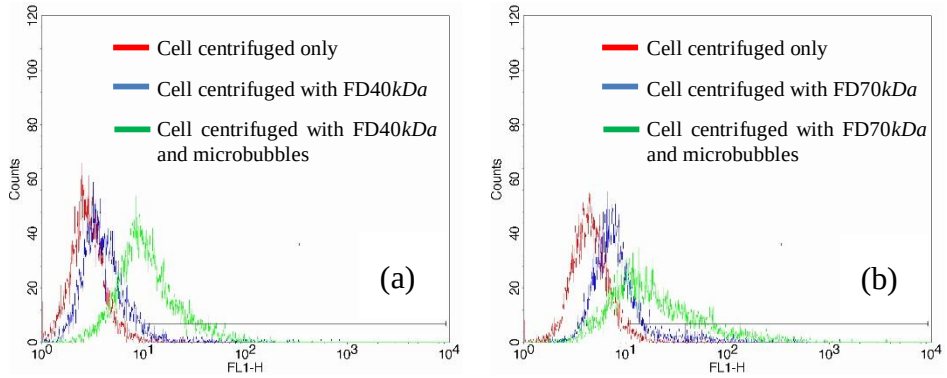

Figure 3-5 A typical FACS diagram of MCF-7 cells: (a) the red curve stands for MCF-7 cells centrifuged alone. The blue curve stands for MCF-7 cells centrifuged with FD40*kDa*, while the green curve stands for MCF-7 cells centrifuged with FD40*kDa* and microbubbles; (b) the red curve stands for MCF-7 cells centrifuged alone. The blue curve stands for MCF-7 cells centrifuged with FD70*kDa*, while the green curve stands for MCF-7 cells centrifuged with FD70*kDa* and microbubbles.

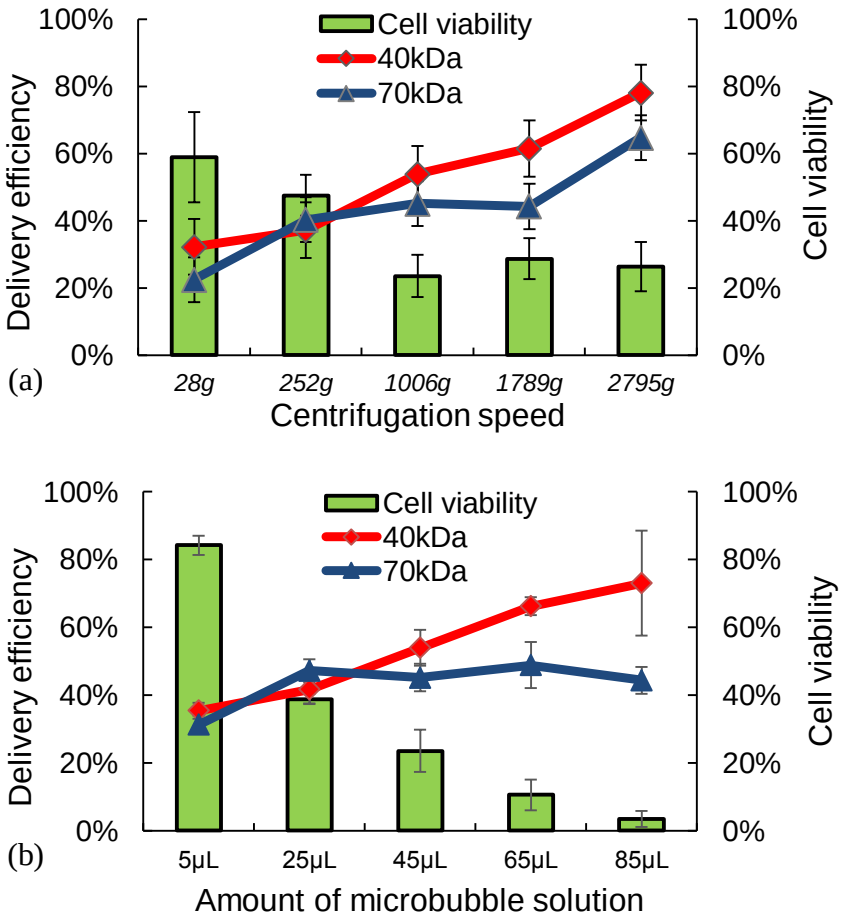

Figure 3-6 FD delivery efficiency and cell viability of MCF-7 cells: (a) delivery efficiency of FD (red curve: 40*kDa*, blue curve: 70*kDa*) and cell viability of MCF-7 cells at different centrifugation speeds, microbubble solution is set at 45*μL*; (b) delivery efficiency of FD (red curve: 40*kDa*, blue curve: 70*kDa*) and cell viability of MCF-7 cells with different volumes of microbubble solution, centrifugation speed is set at 1006*g*.

However, for the samples delivered with FD70*kDa* (the blue curve), the absolute value of the delivery efficiency is always smaller than that of the samples treated with FD40*kDa* (the red curve). The cell viability is shown by the green bar. The cell viability values drop significantly when the

centrifugation speed increases to 1006*g* (3000*RPM*). There is no significant difference for the cell viabilities obtained when treated above 1006*g* (3000*RPM*) (Fig. 3-6a). As shown in Fig. 3-6b, the delivery efficiency can also be increased by increasing the volume of the microbubble solution. The delivery efficiency of the samples treated with FD70*kDa* (the blue curve) is still lower than that of the samples treated with FD40*kDa* (red curve) and fluctuates around 45% as the volume of the microbubble solution increases. The cell viability (the green bar) exhibits a decreasing trend as the volume of the microbubble solution increases. The lowest cell viability is only 3.5% when the sample is treated with 85*μL* microbubble solution.

3.4.2 Confocal microscope images of THP-1 and MCF-7 cells

The observation of FD inside cells directly indicates an increase in cell membrane permeability. In this work, the cell membranes of MCF-7 and THP-1 cells were stained red, while the cell nucleus was stained blue. The images were taken by a Leica SP5 confocal microscope. The THP-1 cell centrifuged alone exhibits a spindle-like shape instead of a round shape (Fig. 3-7a). A similar situation can be found in Fig. 3-7b, which presents the results of treating the THP-1 cells with FD40*kDa* and centrifugation. Some FD40*kDa* (the green spots) are attached to the cell membrane, but

no FD40*kDa* appears inside the THP-1 cells. However, for samples centrifuged with the microbubbles, FD40*kDa* is located inside the cells (see Fig. 3-7c). Interestingly, the FD40*kDa* is inside the cells in two different forms. In the first condition, the FD40*kDa* accumulated in several small regions and is located near the cell membrane (See Fig. 3-7c). The FD also spread freely in the cytoplasm, even in the cell nucleus, as indicated by the red arrows and the dissection view (See Fig. 3-7d). Similarly for the MCF-7 cells, FD70*kDa* is found attached onto the cell membrane when centrifuged without the microbubble solution (See Fig. 3-7e). When treated with microbubbles in the centrifugation field, the FD70*kDa* is located inside cells. Some of the FD70*kDa* is inside the cell nucleus while other FD70*kDa* surrounded the nucleus or accumulated in small regions.

3.4.3 SEM images of THP-1 cells

Fig. 3-8a and b show that the THP-1 cell centrifuged alone has an intact and smooth surface. Fig. 3-8c and d show the membrane status after exposure to microbubble-assisted centrifugation process. Several large holes appear on the cells' membrane, as indicated by the red arrows. The diameters of the holes are from around 1μm in Fig. 3-8c to 3μm in Fig. 3-8d. The cell surface also becomes rougher than that of the cells centrifuged alone. Interestingly, the THP-1 cell morphology is spindled-like

when treated with or without microbubbles (See Fig. 3-8a and d). This result accords with the observation obtained by using the confocal microscope.

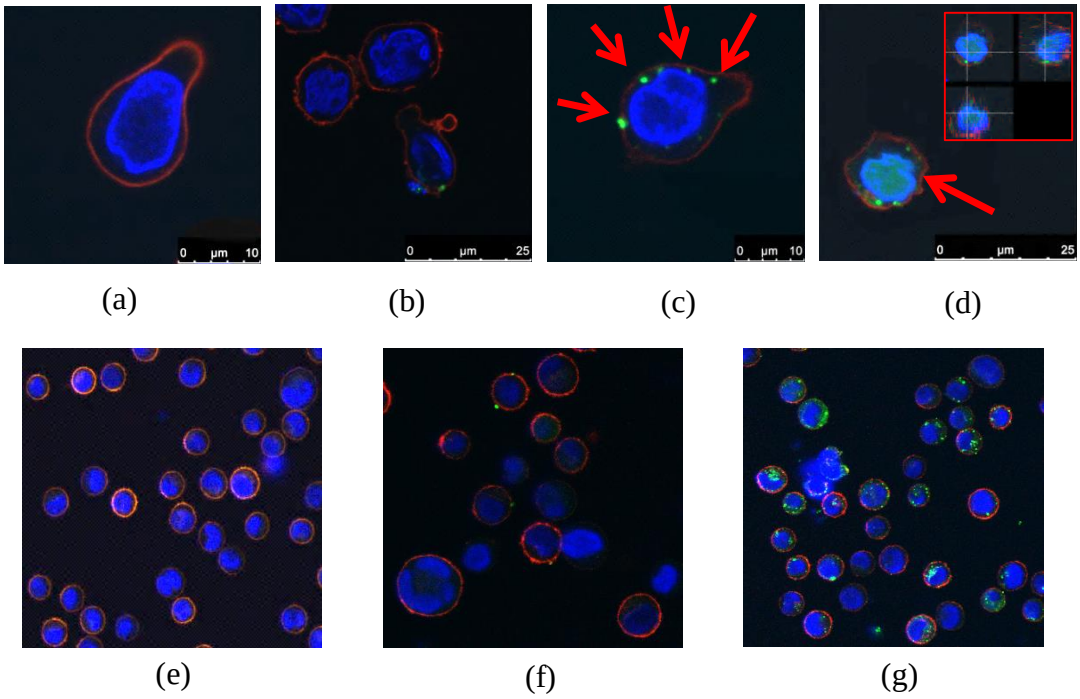

Figure 3-7 Confocal microscope images of THP-1 and MCF-7 cells: (a) THP-1 cells centrifuged without microbubble and FD; (b) THP-1 cells centrifuged with FD; (c) and (d) THP-1 cells centrifuged with microbubbles and FD. A dissection image is shown on the top-right corner of Fig. 3-7d; (e) MCF-7 cells centrifuged without microbubbles and FD; (f) MCF-7 cells centrifuged with FD; (g) MCF-7 cells centrifuged with microbubbles and FD.

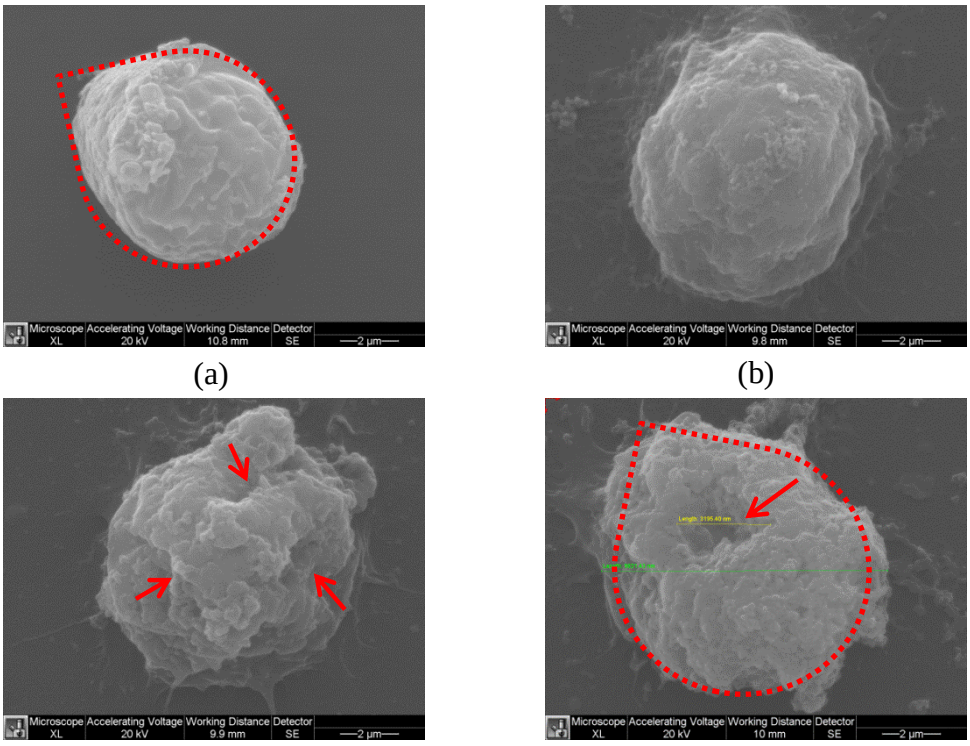

(a) (b)

(c) (d)

Figure 3-8 SEM images of THP-1 cells: (a) and (b) THP-1 cells centrifuged without microbubbles; (c) and (d) THP-1 cells centrifuged with microbubbles. The red dashed lines in Fig. 3-8a and 8d show the cell has a spindle-like morphology after centrifugation.

3.5 Discussion

3.5.1 Results and images analysis

The above results indicate that centrifuging cells with microbubbles greatly increased the cell membrane permeability. The spindle-like morphology observed in the confocal microscope image (Fig. 3-7) and the SEM image (Fig. 3-8) is due to the centrifugation field. As shown in Fig. 3-7a-d, not all the cells have this abnormal morphology. A possible explanation is that

due to the complex pressure environment during centrifugation, different cells experienced different pressure forces. Although most cells might recover their initial round shape immediately after centrifugation, some cells take a longer time for recovery.

The degree of permeability or delivery efficiency and cell viability are strongly correlated to the centrifugation speeds and the volume of microbubble solution. Increasing the centrifugation speed creates a greater degree of elongation in the cells or an increase in the relative velocity between the microbubbles and the cells. The higher the volume of microbubbles introduced into the cell cultures, the larger the number of microbubble bursts produced or the greater the frequency of the collisions between the cells and the microbubbles. It is reasonable to assume that the permeability of the membranes increases more in the presence of stronger microbubble collisions or microbubble bursts. Also, when a certain level of microbubble bursts is reached, the more the cell membrane loosens, the more fragile the cell becomes. Unlike the force in sonoporation, where the force impacts only on the cell membrane, the centrifugal force also affects the components inside the cells. Therefore, the above speculations can also be applied to the cell nucleus, whose outside layer is similar to that of the cell membrane.

An extremely high centrifuge speed and volume of microbubble solution was used in order to observe the THP-1 monocyte cell membrane surface after treatment. There is no doubt that the large and deep holes shown in Fig. 3-8c and d caused a devastating and unrecoverable effect on the cells, and that this effect probably explains the 10% cell viability. The red dashed line indicates that the cell has a spindle-like morphology, which accords with the spindle-like cell images in Fig. 3-7. One can imagine that, with such a big pathway, any therapeutic material can easily be transferred or diffused into the cells. Logically, with a lower centrifugation speed and less microbubble solution, the hole will be much smaller, and the cell will be able to recover. As a result, cell viability will be higher, although the delivery efficiency will definitely be lower.

3.5.2 Mechanism analysis

A major mechanism leading to the increasing of cell membrane permeability is the collisions between the microbubbles and cells due to their opposite movements in the centrifugation field. The collision process can be analyzed as follows: The velocity of a buoyant particle relative to the bulk fluid under the creeping flow condition is as follows, based on Kvale [148]:

$$V = \frac{2(\rho_p - \rho_l)}{9\eta} R^2 g\,, \tag{3-9}$$

where ρ_p is the density of the particle; ρ_l is the density of the liquid; g is the relative centrifugal force; R is the radius of the particle; η is the viscosity of the liquid. The positive sign of the velocity is defined towards the bottom of the centrifuge tube. As the cell density is larger than the liquid density, the cells move towards the bottom of the centrifuge tube. On the contrary, since the microbubbles are composed mainly of air, their density is much smaller than that of the surrounding liquid. This result leads to a negative sign on the velocity generated, so the microbubbles travel towards the top until reaching the surface of the liquid.

THP-1 cells were used as the cell model. To estimate the interaction between the microbubbles and the THP-1 cells, a simplified indentation model was developed to analyze the surface interaction forces before the microbubble bursting, as shown in Fig. 3-9. Chan and Horn showed that the normal hydrodynamic interaction force $F_{\perp}$ can be approximately given by Eq. 3-10. $V_{\perp}$ is the normal approaching velocity, R_1 is the radius of the cell, R_2 is the radius of the microbubble, D is the gap distance, and η is the viscosity of the suspending fluid [149]:

$$F_{\perp,hydrodynamic} \approx \frac{6\pi\eta R_H R_G V_{\perp}}{D}, \tag{3-10}$$

where $\frac{1}{R_H} = \frac{1}{2}(\frac{1}{R_1} + \frac{1}{R_2})$, $R_G = \sqrt{R_1 R_2}$.

The VDW force and the electrical double layer force between the two sphere surfaces can also play a role in the interactions during the approach. For surfaces 1 and 2 interacting in medium 3, the VDW force and electrical double layer force can be described by Eq. 3-11 and Eq. 3-12, respectively, based on the Derjaguin approximation. The sum of the these forces is normally referred to as the DLVO force given by Eq. 3-13, where A_{123} is the Hamaker constant given by Eq. 3-2; ψ_1 and ψ_3 are the surface potential; $1/\kappa$ is the Debye length; ε_1, ε_2 and ε_3 are the dielectric constants; and n_1, n_2 and n_3 are the refractive indexes [72]:

$$F_{123}^{vdw} = -\frac{A_{123}}{6D^2}(\frac{R_1 R_2}{R_1 + R_2}) \tag{3-11}$$

$$F_{123}^{dl} = 4\pi\left(\frac{R_1 R_2}{R_1 + R_2}\right)\varepsilon_0 \varepsilon_2 \kappa \Psi_1 \Psi_3 e^{-\kappa D} \tag{3-12}$$

$$F_{123}^{DLVO} = -\frac{A_{123}}{6D^2}\left(\frac{R_1 R_2}{R_1 + R_2}\right) + 4\pi\left(\frac{R_1 R_2}{R_1 + R_2}\right)\varepsilon_0 \varepsilon_2 \kappa \Psi_1 \Psi_3 e^{-\kappa D} \tag{3-13}$$

$$P = \frac{2C_{fl}(K_B T)^2}{\kappa_b D^3}, \tag{3-14}$$

where κ_b is the bending rigidity (10-25K_BT for common bilayers), and C_{fl} is a numerical constant equal to about 0.1 [150].

For the microbubbles interacting with a lipid bilayer, 1, 2 and 3 represent the air, water and lipid bilayer, respectively. The cell membrane undulation might also induce a repulsive pressure, which can be quantified by Eq. 3-14 [150]. The maximum undulation force F_{MU} induced between the two membranes can be roughly estimated as $F_{MU} = P\pi R_2^2$, where πR_2^2 is the projected area of the microbubble.

The hydrodynamic force $F_{\perp hydrodynamic}$, DLVO force F_{123}^{DLVO} and membrane undulation force F_{MU} for several approaching velocities at different separation distances between the microbubbles and cells are shown in Fig. 3-9e, where R_1 is 5μm and R_2 is 0.5μm. The viscosity for the PBS buffer solution is about 0.001Pa·s [151]. The surface potentials of the (air) sphere and lipid membrane were assumed to be ψ_1=-20 mV and ψ_3=-45 mV, and κ for the PBS solution is around 0.75nm [152]. To evaluate the Hamaker constant, "1" denotes air, "2" denotes medium, while "3" denotes lipid layer. ε_1 is 1, ε_2 is 80, while ε_3 is 2.2. n_1 is 1, n_2 is 1.33, and n_3 is 1.46 separately. At 4^oC, K_BT is 3.82×10$^{-21}N\cdot m$.

Fig. 3-9e shows that both the DLVO force and the membrane undulation force act as repulsive forces for bubbles interacting with a bilayer surface in water. These two forces dominate the interaction up to 2*nm* if the approaching velocity is below 10^{-4}*m/s*. For $V_{\perp}$ >0.001*m/s*, the hydrodynamic force plays a more dominant role compared to that of the DLVO force and the membrane undulation force.

For the indentation of a hard spherical tip against a supported lipid bilayer with thickness ($T_{membrane}$), the normal indentation force is dominated mainly by the area compressibility modulus K_a of the lipid bilayer, and the normal force F_i can be approximately given by Eq. 3-15 (for $R \geq 1.5T_{membrane}$, where *z* is the indentation depth, and R_0 is the radius of the indentation tip, which in our case is the microbubble. However, Eq. 3-15 shows the force diverges as z approaches $T_{membrane}$ [153]. The area compressibility modulus K_a of the bilayer is related to the bending modulus *k* and thickness $T_{membrane}$ by Eq. 3-16. For the lipid bilayer, $\gamma \approx$ 20-50mJ/m^2 [72]; thus, one expects that $K_a \approx 4\gamma \approx$ 80-200mJ/m^2 for the bilayers [72].

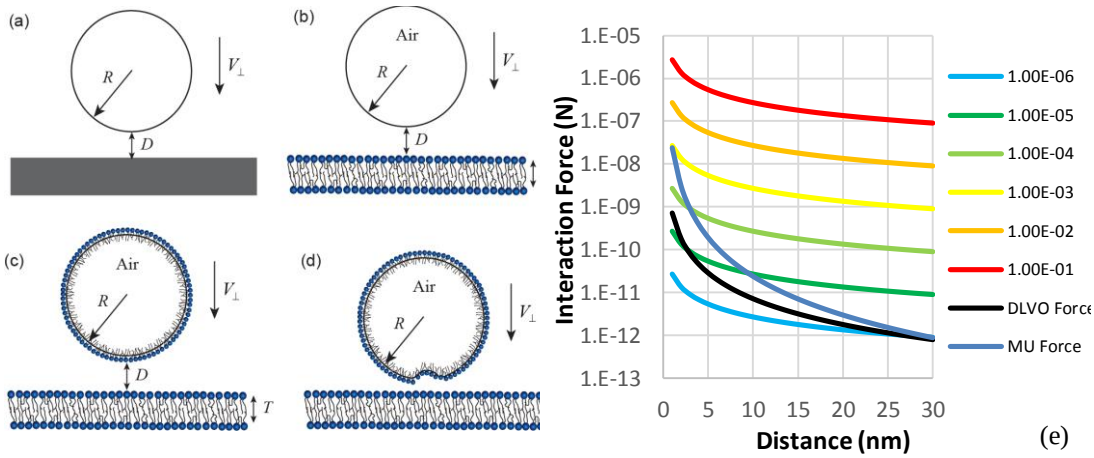

Figure 3-9 Schematic models for interactions between a microbubble and a cell membrane in aqueous solution: (a) a solid sphere approaching a flat solid surface; (b) a spherical bubble approaching a lipid bilayer; (c) a spherical bubble covered by a lipid monolayer interacting with a lipid bilayer; (d) complex interfacial deformations associated with the interactions of Fig. 3-9c; (e) the hydrodynamic force (solid symbols) for six different approaching velocities ($=10^{-6}$, 10^{-5}, 10^{-4}, 10^{-3}, 10^{-2} and $10^{-1} m/s$), the DLVO force and the MU force as a function of the separation distance D between a sphere (of radius R=500*nm*) and a flat surface.

$$F_i = \frac{\pi K_a R_0}{4}\left(\frac{2z}{T_{membrane} - z}\right)^2 \tag{3-15}$$

$$K_a = \frac{24k}{T_{membrane}^2} \approx 4\gamma \tag{3-16}$$

The lipid bilayer can become unstable if the penetration depth $z \geq T_{membrane}/2$, leading to membrane failure. Indentation will occur and continue when

$$F_{overall} = \left|F_{\perp,hydrodynamic}\right| - \left|F_{123}^{DLVO}\right| - \left|F_{membrane\ undulation}\right| > F_i . \tag{3-17}$$

The many receptors, glycocalyx molecules, and other biomacromolecules on the cell membrane may induce a relatively long-range steric force at a distance D of ~10*nm* or even longer [72, 150]. The critical velocity at the microbubble-cell separation distance of 10*nm* can be evaluated by using Eq. 3-17 by taking $\rho_l = 10^3 kg/m^3$, $\rho_{cell} = 1.08\times10^3 kg/m^3$ [154], $\rho_{bubble} = 1 kg/m^3$, while γ can be approximated as $30 mJ/m^2$. By using all the other values in Eq. 3-17, a critical velocity is obtained with $V_{critical} = 0.0148 m/s$. This result means that when the relative velocity between the microbubbles and cells reaches this value, membrane failure will occur and pores will form due to the hydrodynamic force applied on the lipid bilayer.

Centrifugation fields	252*g*	1006*g*	2795*g*	5478*g*	9056*g*
Velocity (*m/s*)	0.00126	0.00502	0.014	0.0274	0.0452

Table 3-1: Relative velocity between microbubbles and cells in various centrifugation fields

For the experiments performed on the THP-1 cells, the centrifugation field was varied from 252*g* to 9056*g*. The resulting relative velocities between the microbubbles and cells are listed in Table 3-1. When the centrifugation field is increased to 2795*g*, the resulting velocity is 0.014*m/s*, which is on the same order of magnitude as the critical velocity $V_{critical}$ estimated above. In other words, when the centrifuge field reaches 2795*g*, the collisions between the microbubbles and cells help increase the membrane

permeability. If one compares the velocities with the delivery efficiency results as shown in Fig. 3-4, an obvious delivery efficiency increase can be observed between the values obtained under 1006*g* and 2795*g*, due to the collision effect mentioned above. When the centrifugation field is strengthened by increasing the centrifuge speed, $V_{\perp}$ will be greater than $V_{critical}$. Theoretically, this result will further enhance the collision-induced membrane permeability. In addition, even though polymers and proteins are embedded on the cell membrane, when the microbubbles and cells are colliding with each other, the equivalent distance can be pushed to a few nanometers, resulting in a much higher hydrodynamic force on the cell membrane compared to that evaluated at a distance of 10*nm*. The calculation results obtained above indicate that the collision-induced hydrodynamic force is sufficiently large to create intracellular pathways.

The real surface interactions between the microbubbles and cell membranes are much more complicated than those in the above simplified model, as shown by the recent experimental studies and theoretical analyses of bubbles interacting with a solid substrate [155-157]. (1) In the above simplified analysis, the cell is assumed to have a round morphology; however, complex interfacial deformations can occur in real interactions [155]. The real cell morphology is flexible and undulating. The stretching of the bilayer also plays an important role in pore formation. (2) Lipid

molecules can self-assemble and form a monolayer on the bubble-water interface, as illustrated in Fig. 3-9c. This result can change the rigidity of the bubble-water interface, the VDW and electrostatic interactions between the microbubbles and cell membranes, and may also change the hydrodynamic boundary conditions. (3) The presence of various receptors, glycocalyx molecules and other biomacromolecules in the cell membrane can lead to relatively long-range steric interactions during the interaction of microbubbles and cells, contributing an additional repulsive force to the collisions of the microbubbles and cells in a centrifugation field [72, 150]. A more rigorous analysis that includes all these effects will provide a more comprehensive picture of the interaction mechanisms between microbubbles and cell membranes, as well as bubble formation, but this kind of analysis is beyond the scope of this thesis.

In addition, the bursting of the microbubbles might also help to increase cell membrane permeability. This mechanism might take a dominant role when the collision-induced hydrodynamic force is insufficient to increase the cell membrane permeability. Two conditions might induce the bursting of microbubbles. Prentice et al. found that when microbubble moving towards a rigid surface, they would probably burst and release a liquid jet [104]. Moreover, the microbubbles manufactured for this thesis are composed mainly of air trapped by a monolayer of lipid particle. This

structure is very sensitive to breaking under a shear force [158]. The shell force might be the friction force between a microbubble and the centrifuge tube surface, a microbubble and another microbubble or a microbubble and a cell. If cells are nearby when the microbubbles are bursting due to the friction force, the resulting liquid phenomenon might also create a pathway on the cell membrane.

Finally, the experiments suggested that some of the cells' endocytosis might be stimulated during the centrifugation process. After this process starts, the cells will first move horizontally onto the centrifuge tube side wall and then slide towards the bottom of the centrifuge tube. The friction between the cells and the centrifuge tube side wall surface might be the endocytosis stimuli. This hypothesis may also explain why FD is observed on the membranes of the THP-1 and MCF-7 cells when they are centrifuged without microbubbles. As shown in Fig. 3-5b and f, the FD seems to enter the cells through the endocytosis process. This mechanism should not be considered as the major contributor to the increase in cell permeability. Comparison of Fig. 3-5f and g, indicates that the microbubbles obviously play a key role in delivering FD into the cytoplasm.

Some researchers have utilized DSPC or tween80 in some liposome structures to induce cell endocytosis for drug delivery [159, 160]. However,

the liposomes formed are in nano-scale, which is very different from the micro-scale microbubbles manufactured for this thesis. In addition, FD40*kDa* and FD70*kDa* were not wrapped inside the microbubbles before the experiment. As a result, the endocytosis might not be due to the material stimulation.

The microbubble-assisted high centrifugation field developed in this study are very effective in increasing cell membrane permeability. Compared to electroporation and sonoporation, the proposed method has the following advantages: (1) No special and expensive equipment is required. The only equipment used is a centrifuge, which is available in almost every laboratory. (2) The proposed method is easy to scale up. Sonoporation experiments are usually performed in a petri dish or tube. To perform large-scale sonoporation, special containers are required. Moreover the ultrasound transducer allocation and power present cost issues. With a centrifuge, several tubes can be used simultaneously. One could easily scale up by changing to an appropriate rotator. Overall, our method could easily be widely implemented and would require no special costs.

3.6 Conclusions

The discussion in this chapter showed that microbubbles can enhance cell membrane permeability in a high centrifugation field. The increase in cell

membrane permeability is measured by the successful and highly efficient delivery of FD40*kDa* into hard-to-deliver THP-1 cells and FD40*kDa* and FD70*kDa* into MCF-7 cells. A simplified model of the cell-bubble interaction force in high centrifugation field estimated that once the relative velocity between the cells and microbubbles reaches a critical value, the collision-induced hydrodynamic force will be large enough to create the intracellular pathway. The cavitation effects from the bursting of the microbubbles might also be a major contributor to the intracellular delivery process. Future studies can focus on either building a more accurate simulation model to discover the interaction mechanism behind this method or exploring the method's potential for gene delivery into plant cells.

Chapter 4

IV. Development and analysis of microbubble-assisted high centrifugation field for increasing plant cell membrane permeability

4.1 Introduction

Although numerous studies have been performed on the delivery of biomaterial into mammalian cells, normal methods usually do not achieve the desired results for plant cells [161] mainly because, unlike mammalian cells, plant cells have a solid cell wall.

A cell wall is a special structure which is usually used to distinguish plant cells from animal cells. The main functions of the cell wall include protecting the cell, maintaining plant cell shape, and preventing plant cells from uptaking excessive water. The cell wall also helps to hold the plant against the force of gravity [162]. The thickness of a plant cell wall varies

from 0.1 to several *μm* thick [162]. A plant cell wall is composed of a matrix of polysaccharides and proteins with microfibrils embedded between them. Some channels like plasmodesmata on the cell wall help to connect adjacent plant cells together and allow for chemical or electrical communication between them. The special structure of a cell wall makes a very tough protection shield. In addition, the cell wall restricts the plant cells' endocytosis ability [163]. As a result, the probability that plant cells will automatically uptake biomaterial is very limited when chemical carriers, like polymers or lipids, approach the cell surface.

The biolistic or particle bombardment system has a long history of being used to increase plant cell membrane permeability [164-166]. In this method, biomaterials along with gold bullets enter the target cells through air pressure acceleration [167, 168]. Electroporation and sonoporation have also been used to increase plant cell membrane permeability. For instance, Blackhall et al. delivered FD (150kD) into plant protoplasts by using electroporation [169], while Azencott et al. investigated the effect of electroporation transmembrane potential, acoustic energy exposure, uptake molecule size, and the presence of a cell wall on intracellular uptake and cell viability [170]. These methods can achieve high delivery efficiency, but cell viability is usually low as a trade-off.

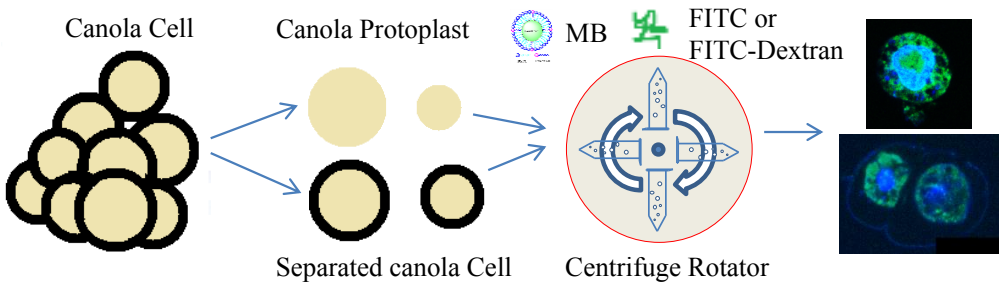

Figure 4-1 Illustration of the proposed delivery method: The thick black circle stands for the cell wall surrounding the canola protoplasts.

4.1.1 Work description

In this thesis, a new method of delivering biomolecules such as FITC and FD into canola protoplasts is developed by using the microbubble assisted centrifuge process. FITC has been widely used as a cell labeling tool for a long time [171, 172], and FD is usually considered as a membrane impermeable molecule [173, 174]. In this thesis, both FITC and FD of molecule weight 70*kDa* and 250*kDa,* respectively, were used for a delivery study. As Fig. 4-1 shows, the canola protoplasts are first extracted from the original canola cell clusters. The protoplasts were then centrifuged with a mixture of microbubbles and biomolecules. The role of the microbubbles is similar to that in their application in sonoporation: the bursting of microbubbles in a high pressure environment induces cavitation or liquid streaming resulting in the formation of pores on the cell membrane [105-107, 144, 145, 175]. In this system, the microbubbles were broken

possibly due to the centrifugation field or the collisions with the canola cells. The FACS histograms and confocal microscope images demonstrated that the biomolecules chosen in our experiment entered the protoplasts after the treatment. The delivery efficiency was around 90%, and the cell viability was around 100% based on cell counts after staining by fluorescein diacetate (FDA). Overall, FITC and FD with a molecular weight of around 70*kDa* and 250*kDa*, respectively, were efficiently delivered into the protoplasts with no compromise in cell viability. The pores formed on the protoplast, as shown in the SEM image, confirmed the delivery mechanism of this method.

4.2 Experimental methods

4.2.1 Cell culture and protoplast preparation

The culturing of canola cells is based on Dr. Hao's report [85]. Generally, a canola cell suspension was maintained on a rotary shaker (160*RPM*) at 20˚C in NLN media (pH 6.0, containing 6.5% sucrose, 30*mg/L* glutathione, 800*mg/L* glutamine, 100*mg/L* L-serine, 0.5*mg/L* a-naphthaleneacetic acid (NAA), 0.05 *mg/L* 6-benzylaminopurine (BA) and 0.5*mg/L* 2,4-D). To extract the protoplasts, the protoplast is based on Kaler's work [176]. plant cells were first incubated with a CPW13M solution, consisting of 27.2*mg/L* KH_2PO_4 (P5655, Sigma-Aldrich), 101*mg/L* KNO_3 (P8291, Sigma-Aldrich),

1480*mg/L* $CaCl_2 \cdot 2H_2O$ (C7902, Sigma-Aldrich), 246*mg/L* $MgSO_4 \cdot 7H_2O$ (63138, Sigma-Aldrich), 0.16*mg/L* KI (60399, Sigma-Aldrich), 0.025*mg/L* $CuSO_4 \cdot 5H_2O$ (C3036, Sigma-Aldrich), and 130*g/L* mannitol (M1902), pH 5.8 for 1*hr* at room temperature. The solution was then replaced with a digestion solution consisting of MS salts, 0.06% 2-(N-Morpholino) ethanesulfonic acid (MES), 13% mannitol, 0.025% Pectolyase Y23 (Kanematsu-Gosho, Tokyo, Japan) and 0.4% cellulase onozuka R-10 (Yakult Honsha Co., Japan), pH 5.8. The solution was then incubated for 5*hrs* at 25*°C* in the dark. The digestion mixture was then filtered through a sterile nylon cell strainer (40*μm*, BD Falcon, USA) to remove the large cell clusters, and centrifuged (40*g*) for 8*mins* afterwards. The resulting pellet was resuspended in a CPW13M solution.

4.2.2 Microbubble-assisted centrifugation process

Microbubbles were prepared as described in Chapter 3. Before the experiment, 1×10^6 canola protoplasts were first transferred to a 1.5*mL* centrifuge tube. A small amount of CPW13M solution was left to submerge the small canola protoplast pellets in the bottom of the centrifuge tube. A 5*μL* FITC solution (0.01*mg/mL*, dissolved in CPW13M) was added into the centrifuge tube and mixed with the microbubble solution. The solution was then centrifuged at different speeds expressed in relative centrifugal force (RCF)/ centrifuge speeds (1*g*/100*RPM*, 28*g*/500*RPM*, 112*g*/1000*RPM*,

252*g*/1500*RPM* and 447*g*/2000*RPM*) in an Allegra™ 25R centrifuge (Beckman Coulter) for 2*mins*. The process was repeated three times. The final amount of FITC solution added was 15*μL*, and the final amount of microbubble solution tested was 5, 15, 25, 45 and 65*μL*. Finally, the canola protoplasts were centrifuged at 252*g* (1500*RPM*) for an additional 4*mins*. Before checking the delivery results, a 400*μL* CPW13M solution was used to wash the sample at 252*g* (1500*RPM*) for 4*mins*.

To deliver FD, the experiment procedures were the same as those for the delivery of FITC. In short, each time, 10*μL* 100*μM* FD70*kDa* or FD250*kDa*, dissolved in CPW13M) was mixed with a 5*μL* microbubble solution and centrifuged at 252*g* (1500*RPM*) for 2*mins*. Overall, the final amount of FD solution added was 30*μL*, and the final amount of microbubble solution was 15*μL*. Next, the canola protoplast solution was centrifuged at 252*g* (1500*RPM*) for 4*mins*. FD is sticky. To wash down the FD remaining on the protoplasts' membranes, the canola protoplasts were washed in 400*μL* CPW13M at 252*g* (1500*RPM*) for 4*mins*.

Comparison experiments were performed in a similar way as the delivery experiments, except that, after 1×10^6 protoplasts were submerged in a CPW13M solution which just covered the cell pellets' surfaces, 15*μL* FITC (0.01*mg/mL*, dissolved in CPW13M) or 30*μL* 100*μM* FD (FD70*kDa* or FD250*kDa*, dissolved in CPW13M) was directly added in the protoplast

solution and left for 6*mins*. The solution was replaced with a 300*μL* CPW13M solution and washed at 252*g* (1500*RPM*) for 4*mins* afterwards.

4.2.3 FACS analysis and cell viability detection

The protoplasts were resuspended in a 300*μL* CPW13M solution after the delivery and washing in order to evaluate the delivery efficiency by using a FACSCalibur (Becton-Dickinson). For a cell viability assay, the protoplasts were stained with 3*μL* FDA, and a 10*μL* protoplast solution was then transferred onto a haemocytometer [85]. Images were taken under both the bright and fluorescent fields, and finally merged together by using Photoshop CS4. Only the fluorescent cells were considered as living. The number of fluorescent cells was counted based on the merged image.

4.2.4 Confocal microscope images and SEM analysis

The canola protoplasts were first attached onto the cover slip by using poly-L-lysine (P4832, Sigma). The protoplasts were then dehydrated by 4% paraformaldehyde for 1.5*hrs*. The cover slip was then turned over and transferred to a slide by using a Vectashield mounting medium containing DAPI (H-1200, Vector). Images were taken under a Leica SP5 II confocal microscope. For the SEM images, 4×10^5 canola protoplasts were centrifuged with a 45*μL* microbubble solution at 1006*g* (3000*RPM*) as mentioned before. Next, the protoplasts were fixed in pure methanol for

5~10*mins*, and then underwent critical point drying as mentioned in [177]. SEM images were taken by a JSM 6301 FX SEM (JEOL) operated at 5*kV*.

4.3 Results and discussion

4.3.1 FITC delivery into canola protoplasts

The effect of centrifugation speed and the amount of microbubble solution on the delivery efficiency was separately identified and quantified by using FACS. Fig. 4-2a shows the delivery efficiency at different centrifugation speeds: different centrifugation speeds have no significant impact on delivery efficiency. The delivery efficiency can reach 90% even when the centrifugation speed is only 1*g* (100*RPM*). Similarly, the delivery efficiencies are independent of the amount of microbubble solution, as shown in Fig. 4-2b. The efficiencies are around 85%-90%. The FACS histograms of the cell fluorescence are shown in Fig. 4-2c and d. The horizontal axis is the fluorescence strength, while the vertical axis stands for the cell number at a certain fluorescence strength. In Fig. 4-2c, the protoplasts centrifuged alone are shown as a single population with low fluorescent intensity on the left. The peak of the fluorescence distribution of the protoplasts mixed with FITC for 6*mins* (the blue curve) shifts slightly to the right. The fluorescence distribution of the protoplasts centrifuged with microbubbles at 1*g* (100*RPM*) (the green curve) shows two peaks

and shifts to the far right. This phenomenon shows that the protoplasts treated with the microbubble-assisted centrifugation process have a stronger fluorescence signal. This result means that the microbubble-assisted centrifugation process did help increase cell membrane permeability. To clearly present the differences between the samples centrifuged with different amounts of microbubble solution, the FACS histograms of the samples centrifuged with 5*μL* and 65*μL* of microbubble solution were compared as shown in Fig. 4-2d.

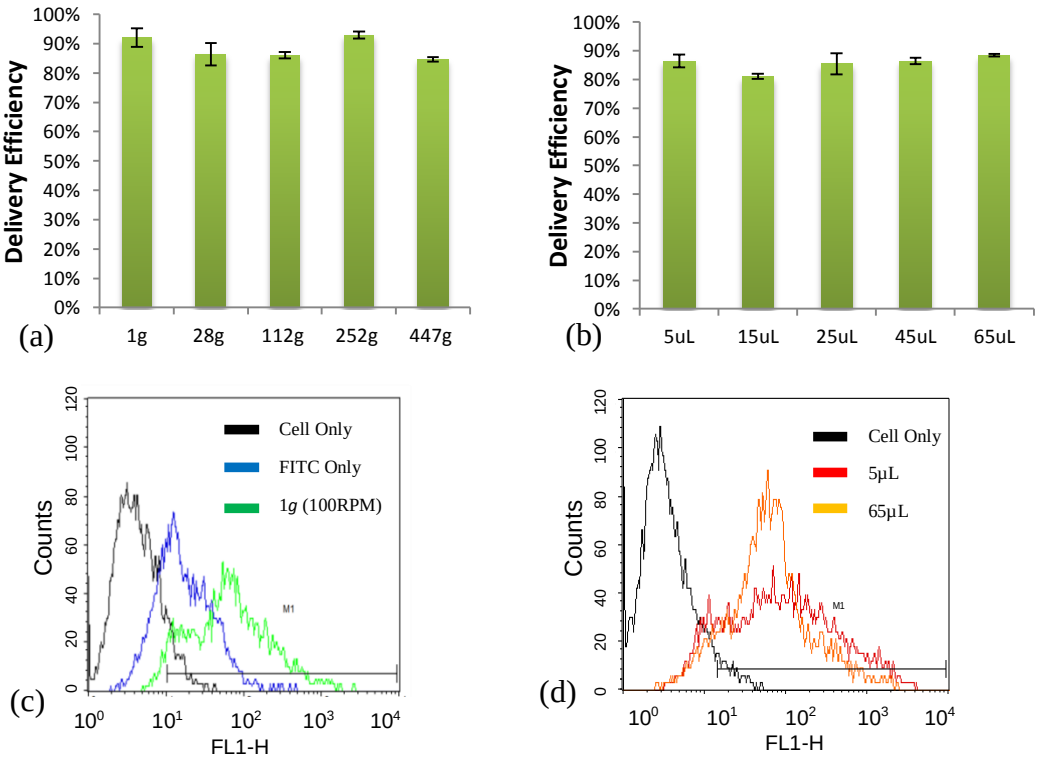

(e) 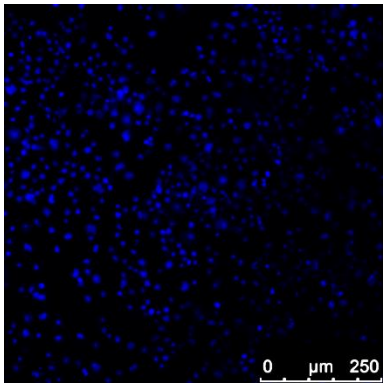

(f) 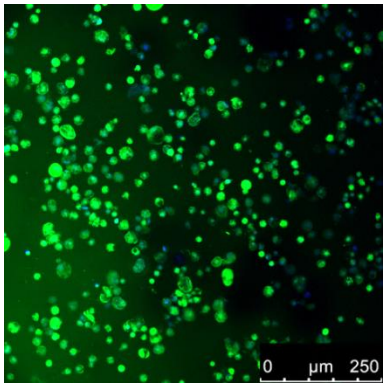

Figure 4-2 FITC delivery into canola protoplasts: (a) delivery efficiency of FITC into canola protoplasts with different centrifuge speeds, microbubble solution is set at 15*µL*; (b) delivery efficiency of FITC into canola protoplasts by using different amounts of microbubble solution, centrifugation speed is set at 112*g*; (c) FACS histogram of canola protoplasts under various conditions. The black curve stand for the canola protoplasts centrifuged alone, while the blue and green curves stand for the result obtained by mixing FITC with canola protoplast only and FITC centrifuged with microbubbles at 1*g* (100*RPM*) 15*µL*, respectively; (d) FACS histogram of delivery efficiency centrifuged at 112*g* with 5*µL* and 65*µL* of microbubble solution. The black curve stands for the canola protoplasts centrifuged alone, while the red and orange curves stand for the results obtained by using a 5*µL* and 65*µL* microbubble solution, respectively; (e) confocal microscope image of canola protoplasts centrifuged alone; (f) confocal microscope image of canola protoplasts centrifuged by the mixture of microbubbles and FITC.

Although the peaks of the two fluorescent distributions seem to coincide with each other, the fluorescence distribution for the canola protoplasts centrifuged with 65*µL* of microbubble solution is much sharper than the one with 5*µL* of microbubble solution. In other words, under a certain fluorescent intensity, the number of fluorescent canola protoplasts from the sample centrifuged with 65*µL* of microbubble solution is higher than that from the sample centrifuged with 5*µL* of microbubble solution. The reason might be that the extra amount of microbubbles created more

pores on the cell membrane of one single protoplast, or a greater population of overall protoplasts. Fig. 4-2e and f show the confocal microscope images of the canola protoplasts centrifuged alone and the canola protoplasts with FITC delivered by the microbubble-assisted centrifugation. The blue color stands for the cell nucleus, while the green fluorescent color was emitted by FITC under the proper laser stimulation. In Fig. 4-2f, since FITC was delivered into the protoplasts, most of the canola protoplasts are green. This result confirms the increase of canola protoplast membrane permeability.

4.3.2 FD delivery into canola protoplasts

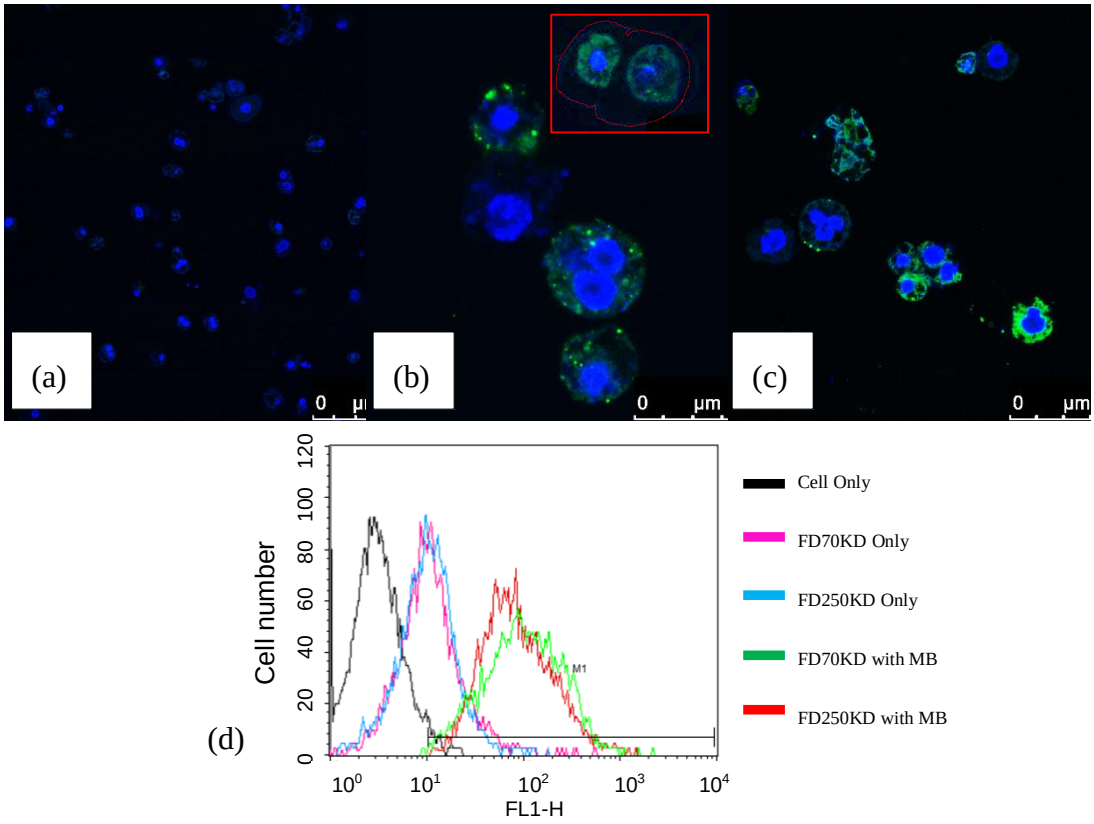

Figure 4-3 Confocal microscope images of canola protoplasts with delivered FD: (a) canola protoplasts centrifuged alone; (b) canola protoplasts centrifuged with microbubbles and FD70*kDa*; the image on the top-right corner of Fig. 4-3b shows the FD70*kDa* was delivered even into canola cells with cell walls. The cell wall is marked by the red dashed line; (c) canola protoplasts centrifuged with microbubbles and FD250*kDa*. (d) FACS histogram of canola protoplasts under various conditions: the black curve stands for the canola protoplasts centrifuged alone, the pink and blue curve stand for the canola protoplasts mixed with FD70*kDa* and FD250*kDa* respectively, while the red curve and green curve stand for the canola protoplasts centrifuged with microbubbles and FD70*kDa* or FD 250*kDa*, respectively.

Fig. 4-3b and c show the confocal microscope images of the samples centrifuged with the mixture of microbubbles and FD. Both images show

an intense green fluorescent signal released by FD closely surrounding the cell nucleus (the blue color). In the top-right corner of Fig. 4-3b, the image shows that the FD could even enter walled canola cells after treatment using microbubble-assisted delivery. A small population of individual walled canola cells are present because some of the cell walls were not fully removed by the enzyme solution. Unlike canola protoplast cells, the walled cells usually do not have a round morphology. FACS histogram is shown in Fig. 4-3d. Similar to the results obtained under the FITC delivery experiment, the results for the FD delivery show that when the cells were centrifuged with microbubbles, the fluorescence distribution clearly shifted to the right compared to the canola protoplasts centrifuged alone or the canola protoplasts mixed only with FD70*kDa* or FD250*kDa*.

4.3.3 Viability of canola protoplasts treated with the microbubble-assisted centrifugation process

The canola protoplast viability was checked by using the FDA staining method. Only the fluorescent protoplasts were considered to be viable, and the number of fluorescent cells was counted on a haemocytometer. Although different amounts of microbubble solution were used, the number of live cells was not significantly different from the number in cell control, as shown in Fig. 4-4a. The percentages of the number of viable

protoplasts in various amounts of microbubble solution compared to the protoplasts centrifuged alone are also shown in Fig. 4-4a.

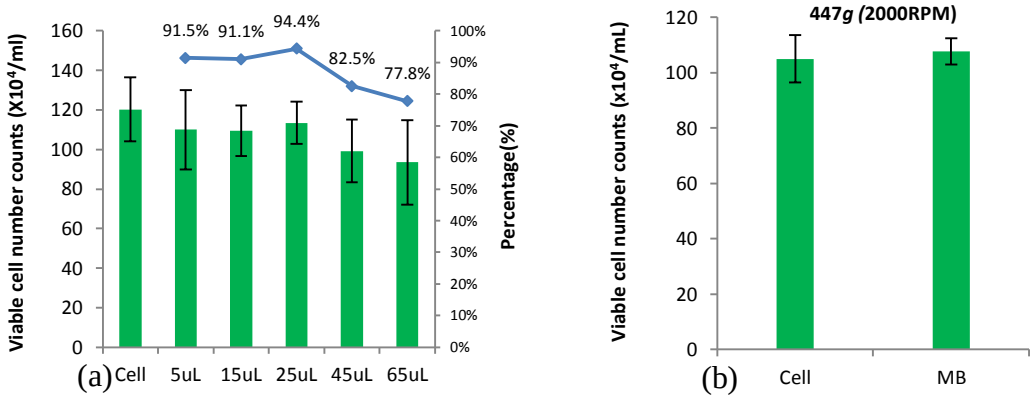

Figure 4-4 Cell viability of canola protoplasts detected by the FDA staining method: (a) viable cell count with different amounts of microbubble solution; (b) viable cell count after centrifuging at 447*g* (2000*RPM*) with microbubble solution.

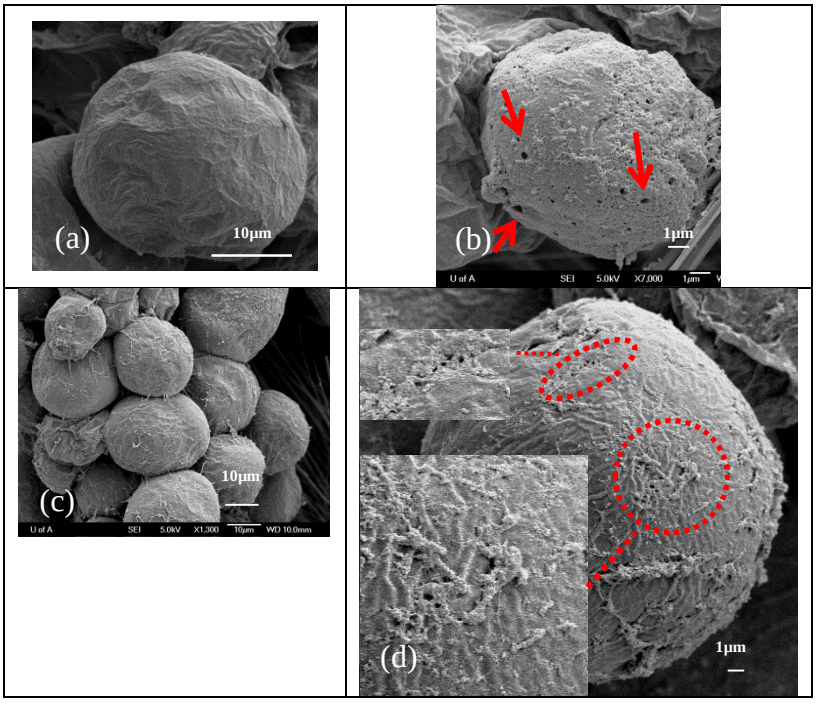

Figure 4-5 SEM images of canola cells: (a) a canola protoplast with centrifugation alone; (b) canola protoplasts treated by microbubble- assisted centrifugation; the pores formed are pointed out by the red arrows; (c) canola cells with cell wall centrifuged alone; (d) canola cells with cell wall centrifuged with microbubbles. The red dashed circle marks the area with small pore.

Except at the point where 25*µL* of microbubble solution was used, the values of the percentage decreased as the amount of microbubble solution increased. The number of viable cells of the sample treated with 447*g* (2000*RPM*) was also counted by using the same method. The result is shown in Fig. 4-4b. Under 447*g*, the number of viable canola protoplasts centrifuged with microbubbles is very similar to the number of viable canola protoplasts centrifuged alone. These data indicate that the microbubble-assisted centrifugation process caused very limited damage

to the canola protoplasts. As mentioned in Chapter 3, the collision between microbubbles and cells or microbubble bursts can induce pores on the cell membrane. However, the protoplasts might recover from this temporary pore opening, since most of the protoplasts survive after the treatment.

4.3.4 SEM images of canola protoplasts treated with the microbubble-assisted centrifugation process

Fig. 4-5a shows the canola protoplasts' morphology after the protoplasts were centrifuged alone. The cell surface is intact and smooth. The canola protoplasts' surfaces change significantly when centrifuged with microbubbles (Fig. 4-5b). Many small pores are visible on the cell surface, as pointed out by the red arrows. The cell surface also becomes rougher. For canola cells with cell walls, the cells accumulate together and attach to each other (Fig. 4-5c and d). When centrifuged alone, the canola cells show an integral cell wall (Fig. 4-5c). After the cells were centrifuged with microbubbles, pores were discovered on plant cell wall. Unlike the pores scattered on the canola protoplasts' membranes, the pores on the cell walls are formed only in certain regions and are much smaller when the cells are centrifuged with microbubbles. The regions marked by the red dashed line are magnified and shown in the left part of Fig. 4-5d. The protoplasts' membranes are composed mainly of a lipid double layer, while

the cell walls are made of cellulose. As a result, the cell wall is much more rigid than the cell membrane. The pores created by the impact force are therefore much smaller on the cell wall than on the cell membrane. The pores formed on the protoplasts' membranes and cell walls might be due to the bursting of microbubbles or the collision between microbubbles and cells during the centrifuge process. Once the intracellular pathway was created, biomaterials such as FITC or FD could diffuse into the cytoplasm.

4.4 Conclusions

Not much research has been reported so far on biomaterial delivery into plant cells. In this Chapter, biomaterials with molecular weight up to 250*kDa* were successfully delivered into canola protoplasts by using a microbubble-assisted delivery method. The delivery efficiency was around 90%. Although the delivery efficiency is high within a broad range of centrifugation speeds and amounts of microbubble solution, the FACS histogram showed that a higher amount of microbubble solution could lead to stronger fluorescence. The confocal microscope images showed that FD could be delivered even into canola cells with intact cell walls. This method's applications in plant cell biology and transformation technology are the subject of our future investigations.

Chapter 5

V. Investigation of the effect of cell deformed morphology and mechanical properties on cell membrane permeability

5.1 Introduction

Cell response to mechanical forces is a hot topic in several biomedical areas. In bioreactor design, since the interaction force between a cell and a bubble might induce cell death, researchers study this interaction in order to design more efficient bioreactors and production processes. In sonoporation research, studying the interaction between cells and microbubbles is very important for understanding the intracellular delivery mechanism. The understanding of the sonoporation mechanism could help to further increase cell membrane permeability and, thus, also to increase the intracellular delivery efficiency. It has been reported that microbubble flow and microbubbles' effects on the lung epithelium cells

are the direct cause of the acute respiratory distress syndrome (ARDS), a condition commonly treated by mechanical ventilation [178]. Studying the interaction of microbubble flow with EpC cells could help researchers to understand the pathology of ARDS and to develop treatments for it. In all the cases mentioned above, the cell membrane is the component in direct contact with any external force. Therefore, researchers investigating the effects of external forces on cell membrane permeability or cell membrane destruction ignore the cells' biochemical responses.

Both theoretical and experimental studies have been performed to investigate the cell membrane responses to mechanical forces. A general summary is provided below.

5.1.1 Experimental studies on the responses of cell membrane permeability to external force

5.1.1.1 Mechanical properties measurement

Many experimental studies have focused on measuring cell mechanical properties. Traditional testing includes the use of cytoindentation and pipette aspiration. As technology progresses, devices like AFM, MTC, and optical tweezers have also been developed to measure cell mechanical properties. For example, Alcaez et al. used AFM to measure the shear modulus of A549 cells, while Balland et al. used optical tweezers, and

Trepat et al. used magnetic tweezers to test the same cell line [179-182]. However, the measurement results differ. Even when the same equipment is used on the same cell line, the resulting values cover a broad range. These large value differences are caused by the individual cell variance rather than by equipment differences. The modulus of cell mechanical properties needs to cover a broad range when theoretical cell models are built to investigate the cell membrane responses to external forces.

5.1.1.2 Optical observation

Optical techniques are widely used to observe cell morphology or structure change. Normally, these techniques are rarely used alone. An optical technique is usually considered as a supporting tool for theoretical or experimental analysis. The cell imaging quality depends on the cell staining method and the imaging equipment. A more efficient cell staining method creates an image with much higher color contrast and stronger ability to counter the bleach effect. These advances provide more potential for observing cell details under a fluorescent microscope. Some of the staining agents can help to stain cells even when they are still alive [183]. The development of the confocal microscope enables the three-dimensional structure of cells to be observed in real time, while high speed camera can help to capture the cell deformation process [184]. Neither of these results could have been achieved in the past.

5.1.2 Theoretical studies on the responses of cell membrane permeability to external forces

Theoretical studies on the responses of cell membrane permeability to external forces have different emphases depending on the application area. In sonoporation studies, a cell is usually modeled with simple shape like a circle. The main focus is on using fluid dynamics to calculate the streamline, pressure or shear force induced by the liquid motion around the microbubbles [185]. Once the resulting value of a force is beyond the threshold, the cell membrane is considered to have been penetrated. Simulations can also be based on a molecular dynamics perspective [186]. In this case, cell morphology is neglected, and only the regional cell membrane interacting with the mechanical force is considered. Cell morphology is a more critical element to consider when investigating the structural behavior of a cell. To investigate cell structure behavior, many simulations have been performed on either two-dimensional or three-dimensional scales by using the finite element method [187-190]. Although cell morphology has been considered to be irregular in some studies, the real cell morphology, especially the surface structure, is still over-simplified. This problem significantly limits cell structure modeling. As a result, it rarely can provide any intuitive guidance for real world applications.

5.1.2.1 Cell modeling method

To study cell structure behavior, cells and cell membranes need proper models. Although a cell has a complex and heterogeneous structure, several research groups have used continuum mechanics to model cells [191-196]. In continuum mechanics, the matter on the atomic scale is neglected as the length scale of the object is much larger than the atom size, and only collective contributions are considered. For example, although individual cytoskeletal components might have different mechanical contributions, only the summation of the contributions from all cytoskeleton components is used to estimate cell mechanical properties. The major three parameters in continuum mechanics are stress, displacement and strain. Stress is the value of the force per unit area experienced from its adjacent particle. Displacement is the difference between the final and initial position due to an external force. Strain is a dimensionless parameter measuring the deformation compared to its original size.

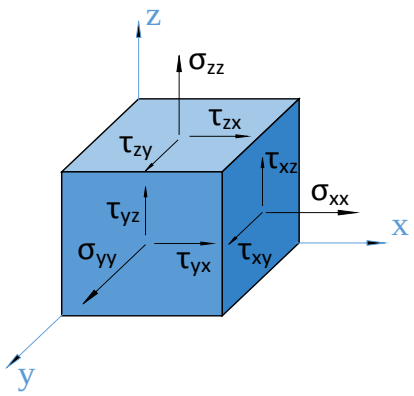

Figure 5-1 Cartesian Cauchy stress components in three dimensions.

If one considers a three-dimensional object aligned with the axes x, y, z in Cartesian coordinates, as shown in Fig. 5-1, under the steady state, the different components of the stress will follow the equilibrium equations Eq. 5-1:

$$\begin{bmatrix} \frac{\partial \sigma_{xx}}{\partial x} + \frac{\partial \tau_{xy}}{\partial x} + \frac{\partial \tau_{xz}}{\partial x} \\ \frac{\partial \tau_{yx}}{\partial y} + \frac{\partial \sigma_{yy}}{\partial y} + \frac{\partial \tau_{yz}}{\partial y} \\ \frac{\partial \tau_{zx}}{\partial z} + \frac{\partial \tau_{zy}}{\partial z} + \frac{\partial \sigma_{zz}}{\partial z} \end{bmatrix} = 0, \tag{5-1}$$

where $\sigma_{xx}, \sigma_{yy}, \sigma_{zz}$ are the normal stress, and $\tau_{xy}, \tau_{xz}, \tau_{yx}, \tau_{yz}, \tau_{zx}, \tau_{zy}$ are the shear stress. The stress is related to the strain through the constitutive equation, which varies based on the material model. If a cell is modeled as isotropic linear elastic material [195], the constitutive equation in the three-dimensional scale can be written in a matrix form as Eq. 5-2:

$$\begin{bmatrix} \varepsilon_{xx} \\ \varepsilon_{yy} \\ \varepsilon_{zz} \\ \gamma_{xy} \\ \gamma_{yz} \\ \gamma_{zx} \end{bmatrix} = \begin{bmatrix} \frac{1}{E} & -\frac{\nu}{E} & -\frac{\nu}{E} & 0 & 0 & 0 \\ -\frac{\nu}{E} & \frac{1}{E} & -\frac{\nu}{E} & 0 & 0 & 0 \\ -\frac{\nu}{E} & -\frac{\nu}{E} & \frac{1}{E} & 0 & 0 & 0 \\ 0 & 0 & 0 & \frac{1}{G} & 0 & 0 \\ 0 & 0 & 0 & 0 & \frac{1}{G} & 0 \\ 0 & 0 & 0 & 0 & 0 & \frac{1}{G} \end{bmatrix} \begin{bmatrix} \sigma_{xx} \\ \sigma_{yy} \\ \sigma_{zz} \\ \tau_{xy} \\ \tau_{yz} \\ \tau_{zx} \end{bmatrix}, \quad (5\text{-}2)$$

where $\varepsilon_{xx}, \varepsilon_{yy}, \varepsilon_{zz}$ are the normal strain; $\gamma_{xy}, \gamma_{yz}, \gamma_{zx}$ are the shear strain; v is the Poisson ration; E is the elastic modulus; and G is the shear modulus. For a typical isotropic elastic material, the elastic modulus E can be related to the shear modulus G as shown in Eq. 5-3:

$$E = 2G(1+\nu). \quad (5\text{-}3)$$

A cell membrane can also be modeled as isotropic material in a simulation, but Dailey et al. found that the theoretical value did not match the experimental values under the isotropic model. Therefore, these researchers proposed modeling the cell membrane as orthotropic material [197]. The constitutive equation for orthotropic material is similar to the one for isotropic material, as shown in Eq. 5-4. However, Young's modulus and the shear modulus have no relationship, and their values vary on different axes.

$$\begin{bmatrix} \varepsilon_{xx} \\ \varepsilon_{yy} \\ \varepsilon_{zz} \\ \gamma_{xy} \\ \gamma_{yz} \\ \gamma_{zx} \end{bmatrix} = \begin{bmatrix} \frac{1}{E_x} & -\frac{\nu_{yx}}{E_y} & -\frac{\nu_{zx}}{E_z} & 0 & 0 & 0 \\ -\frac{\nu_{xy}}{E_x} & \frac{1}{E_y} & -\frac{\nu_{zy}}{E_z} & 0 & 0 & 0 \\ -\frac{\nu_{xz}}{E_x} & -\frac{\nu_{yz}}{E_y} & \frac{1}{E_z} & 0 & 0 & 0 \\ 0 & 0 & 0 & \frac{1}{G_{xy}} & 0 & 0 \\ 0 & 0 & 0 & 0 & \frac{1}{G_{yz}} & 0 \\ 0 & 0 & 0 & 0 & 0 & \frac{1}{G_{zx}} \end{bmatrix} \begin{bmatrix} \sigma_{xx} \\ \sigma_{yy} \\ \sigma_{zz} \\ \tau_{xy} \\ \tau_{yz} \\ \tau_{zx} \end{bmatrix} \quad (5\text{-}4)$$

5.1.3 The key factors in studying the responses of cell membrane permeability to external forces

5.1.3.1 External forces

Obviously, the value and type of an external mechanical force are important when evaluating the cell membrane responses. An external force can exist in different forms such as pressure or shear stress. The type of force dominating the interaction with a cell depends on the local cell environment and the interaction condition. In the early reports of scale-up cultures of mammalian cells, HeLa S3 and mouse L929 cells were passed through capillary tubes of different diameters [198-200]. In this condition, shear force (10-200N/m^2) is the dominant force leading to cell

death. Midler and Finn found that the shear force exposure time might also contribute to the cell damage [201]. However, when bubbles were introduced into the bioreactor, the major cell membrane damage was found to be due to the bubble ruptures at the gas-liquid interface [202-204]. The value of the shear stress derived from bubbles was very small and thus could be neglected [205]. In sonoporation studies, as mentioned in section 3, when a microbubble is in the stable cavitation stage, the liquid around the microbubble forms microstreaming, which induces shear stress on the cell membrane. If the acoustic pressure is sufficiently high, the microbubble will change from stable cavitation into inertial cavitation, which will cause the microbubble to burst. The bursting microbubble will produce a liquid jet. The high intense pressure induced by the liquid jet is sufficiently high to create pores on a cell membrane. In ARDS disease, the microbubble flow above the EpC cells generates both pressure and shear force on the cell surface. The computational results directly relate the spatial gradient in the pressure with the cell membrane rupture [206]. While the microbubble flow velocity is a critical factor in determining the value of the maximum pressure or shear stress, parameters like fluid viscosity, the surface tension of the air-liquid interface, and channel half-height will also play important roles in determining the resulting pressure value range.

5.1.3.2 Cell morphology

When investigating cell structural behavior, cell morphology is a key element in determining the cell membrane responses to an external force. Studies have shown that the confluent type I and subconfluent type II EpC cells, which were different in morphology, structural and typological had different injury responses to cyclic stretching [207]. Ghadiali and Dailey proposed that changes in cell morphology amplify the hydrodynamic stress applied on subconfluent cells compared to the magnitude of the stress on confluent cells [178]. In a computational study, Jacob and Gaver demonstrated that the stress amplification is a function of the aspect ratio [208]. Slomka and Gefen found that the localized tensile strain in the cell membrane and nuclear surface area were very different under compression although the cells were from the same type and culture [209].

5.1.4 Confocal microscope image-based method to rebuild cell morphology

Experimental methods can directly measure the cell membrane responses to external forces, but cannot provide any guidance for future applications. Although theoretical methods can provide more detailed and quantitative results for cell membrane response, these methods' accuracy and guidance rely heavily on the complexity of the simulation model. To

compare the structural behaviors of cells with different morphologies, the normal theoretical models, which consider cells as just irregular circles, are too simplified. In order to obtain more meaningful and accurate simulation results, a detailed model to represent cell morphology, especially the surface structure, is required.

Recently, researchers developed a confocal microscope image-based method to study cell structure behavior [210-212]. This method involves using the confocal microscope images to model the cell first. To take confocal microscope images, the lipid double layer of the cell membrane or the major proteins on the membrane need to be stained. Then the cell sample is prepared and viewed under a confocal microscope, which has the ability to focus on one layer by filtering the scattered and reflected fluorescent lights from other layers. Thus, a stack of images taken from different layers or heights of the cell can be collected. After transferring the stack of images to computer aided design (CAD) software such as SolidWorks2012, one needs to draw the cell membrane contour based on the colored outline of the cell membrane on each image. Then the cell surface can be generated by lofting the cell membrane contours onto different layers. Using this method, one can obtain real-time cell morphology with a detailed cell surface structure. Applying external force with this model is then more meaningful than doing so with other models.

5.1.5 Work description

In Chapter 3 and Chapter 4, it was reported that by using microbubble-assisted high centrifugation field, the membrane permeability of mammalian cells and plant cells could be increased [213, 214]. Two mechanisms behind this method were hypothesized.

In our microbubble-assisted high centrifugation field system, the first mechanism to increase cell membrane permeability is the collision between microbubbles and cells. It is known that cell density is greater than the culture medium, and that microbubbles are much lighter because of their large portion of air. As a result, the cells go down to the bottom of the centrifuge tube, while the microbubbles move towards the liquid surface. This opposite movement causes unavoidable collisions between the microbubbles and cells. When the cells and microbubbles are going to collide with each other, the liquid between the microbubbles and the cell membrane outer layer is squeezed and induces a hydrodynamic force on the cell membrane [149]. This force is highly likely to break the cell membrane, especially near the collision region. However, if the distance between the microbubble and cell membrane is sufficiently small, the DLVO force and membrane undulation force should also be considered [150]. The DLVO force is composed of the VDW force and the electrostatic forces. The membrane undulation force is due to the entropic thermal

undulation of the cell membrane. All these three factors provide a repulsive force to impede the microbubble from colliding with the cell. The value of the hydrodynamic force is directly related to the relative velocity between the microbubble and the cell. By comparing the hydrodynamic force with the force needed to penetrate the membrane, one can obtain the critical velocity needed for the membrane penetration to happen. For example, when the interaction forces are evaluated at a separation distance between the microbubble and cell of 10*nm*, the critical relative velocity between the microbubble and cell is 0.0148*m/s*. If the relative velocity between the microbubbles and cells is greater than this value, the hydrodynamic force will penetrate the cell membrane [214]. Since this effect is due mainly to the collision, this force will be referred to as the collision induced impulsion (CII) force.

Microbubble bursting is the second proposed mechanism. Microbubbles might burst due to the collision between a microbubble and a cell, a microbubble and another microbubble, or a microbubble and the side-wall of the centrifuge tube. Microbubble bursting will lead to similar situation as that in microbubble-assisted sonoporation. The experimental results from Geers et al.'s work showed that the microbubble bursting helps to deliver the virus vector directly into the cytosol [215]. Microbubble bursting leads to a high pressure and high temperature environment resulting in the

generation of shock waves and liquid jets [106,107,145]. The cell membrane penetration due to shock waves or liquid jets has been investigated both theoretically and experimentally. Kodama et al. investigated the interaction of shock waves with the cell lipid membrane by applying acoustic theory and molecular dynamics simulation [186]. These researchers found that as the shock wave impulse increased, the number of water molecules delivered into the cell membrane also increased. Lokhandwalla et al. found that the haemolysis of red blood cells was directly related to the gradient of the shock strength and validated shearing as a cell lysis main mechanism [216]. Ohl et al. used a high speed camera to observe the microbubble cavitation process and found that the liquid jet could induce pores on the cell membrane [185]. Kudo et al. directly viewed the pores generated by the cavitation of microbubbles under SEM. These researchers found that a single shot of pulsed ultrasound with a duration of several microseconds was sufficient to perforate the membrane in the presence of microbubbles [217].

In addition to the above two proposed mechanisms, cell morphology is also a key element which determines the responses of cell membrane permeability to external forces. In our proposed method, a cell experiences a highly deformed state. Hoffman and Inoue centrifuged cells under conditions similar to those in our experiments, using a high speed

camera to observe cell morphology change at high centrifugation speeds [116]. These researchers found that, under high speed centrifugation, the cell morphology was transformed into a spindle shape. This morphology change might have been due to a squeezing effect. After the centrifugation speed was decreased to normal speed, most cells recovered their original shape. Although these shape changes are reversible for most cells, cells with special morphologies during the centrifugation process are of interest in this thesis, especially because of the influence of pressure on structural behavior. Investigating the interaction between microbubbles and deformed cells is critical for understanding the role of centrifugation and microbubbles during the process.

To rebuild a cell's deformed morphology, Dailey and Gefen developed a new method using confocal microscope images to construct three-dimensional finite element models for *in-vitro* cell morphologies and analyzed cell mechanics by using these models [210-212]. In this thesis, the same method was used to build two types of deformed cells under the centrifugation field. Because an increased strain in the cell membrane is correlated with an increase of cell membrane permeability [218], the value range of the strain and strain distribution on the cell membrane, especially those induced by the CII force, were compared for the two types of deformed cells. Cell mechanical properties including the cell elastic

modulus E_{cell} , the membrane elastic modulus $E_{membrane}$, shear modulus $G_{membrane}$, and the membrane thickness h were also systematically considered. Our results indicate that cell morphology and mechanical properties play an important role in cell membrane strain distribution and in the magnitude of the average or the maximum localized strain. This result demonstrates that centrifugation induced cell deformation is critical in the increase of cell membrane permeability under a microbubble CII force.

5.2 Simulation methods

5.2.1 Cell preparation

MCF-7 cells were cultured in RPMI1640 (11875-093, Gibco) with 10% FBS and 1% P/S and incubated in incubator with 20% CO_2. On the day of the experiment, MCF-7 cells were detached from the cell culture dish by using trypsin. These cells were then washed and suspended in a RPMI1640 solution. $4x10^5$ cells were transferred to one centrifuge tube and centrifuged at 4^oC with 9075g (9000RPM) for 6$mins$. The cells were then extracted and attached to the cover slip by using poly-L-lysine (P4832, Sigma) and dehydrated in 4% paraformaldehyde (158127, Sigma-Aldrich) for 10$mins$. Rhodamine Phalloidin (Molecular Probes®, Invitrogen) was used to stain the cell membrane actins for 1hr. Finally, the cell sample

was flipped onto a slide by using the Vectashield® mounting medium with DAPI (H-1200, Vector). The images were taken in z-stacks with intervals of 0.4μm by using a Leica SP5 II confocal microscope.

5.2.2 Rebuilding cell morphology

To rebuild the cell morphology, the z-stack images were transferred to CAD software SolidWorks2012. First, parallel planes with an interval of 0.4μm were created at different heights, then the image was inserted onto the plane following the sequence. Since most microbubble collisions happen on the cell surface facing the liquid, only the images of the upside body of the cells were selected for the model building. After inserting the image onto the corresponding plane, the contours of the cell membrane were manually drawn on each image, as shown in Fig. 5-2a, c. The cell membrane surface was then formed by lofting the spline contours onto different planes as shown in Fig. 5-2b, e. Several geometry parameters were measured on the cell model. The base area is the project area of the model. The volume is the space occupied by the cell model. The height is measured from the model's top surface to the bottom area. The maximum length is defined the as greatest length of the line measured between two cell edges. The width is the distance determined by the cell edges and drawing a line vertical to and intersecting at the middle of the maximum

length line. The geometrical information for the two generated cell models is listed in Table 5-1.

	Base area (μm^2)	Volume (μm^3)	Height (μm)	Max length (μm)	Width (μm)
Deformation type I cell	322.2	1522.4	8.3	23.7	17.6
Deformation type II cell	356.1	852.9	8.4	35.3	10.3

Table 5-1 Quantitative geometry data for the deformation type I and deformation type II cell

5.2.3 Finite element models

The rebuilt cell morphology models were transferred to ANSYS® to generate the finite element models. Both the deformation type I and deformation type II cells were meshed with four-node tetrahedral isotropic solid elements (node 285) for the cell body and three-dimensional four node shell elements (node 181) for the cell membrane. The deformation type I cell model had 19417 elements in the cell solid and 2641 elements in the cell membrane. The deformation type II cell model had 11364 elements in the cell solid and 2690 elements in the cell membrane. The cell model after the meshing process is shown in Fig. 5-2c, f.

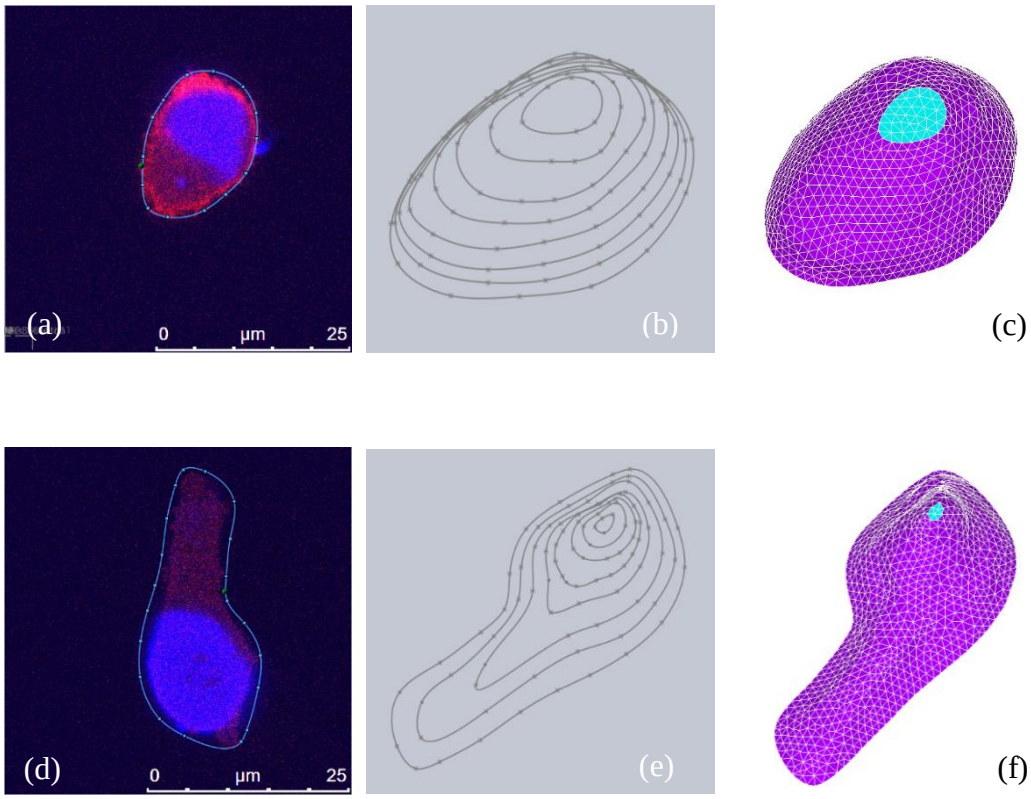

Figure 5-2 Operation process for reconstructing deformation type I and deformation type II cells: (a) and (d) confocal microscope images, the contours are drawn on the image to define the cell boundary; (b) and (e) a stack of boundary contours, these contours were used to generate the cell membrane; (c) and (f) cell models after meshing in ANSYS®.

5.2.4 CII force on cell membrane

The hydrodynamic force between two curved surfaces can be estimated by using Eq. 3-10. The VDW force and electrical double layer force can be calculated by using Eq. 3-11 and Eq. 3-12, respectively. Under 9056*g* (9000*RPM*), taking η=0.001, R_{cell} =8.2μm, $R_{microbubble}$ =0.5μm, ρ_{cell} =1080kg/m^3 and $\rho_{microbubble}$ =1kg/m^3 into Eq. 3-9, the microbubble has a

velocity of $5.03\times10^{-3}m/s$, while the velocity of the MCF-7 cell is $0.109m/s$. When the two velocities are added together, the relative velocity between the microbubble and the cell is $0.114m/s$. Many receptors, glycocalyx molecules, and other biomacromolecules are on the cell membrane and may induce a relatively long-range steric force at a distance D of ~$10nm$ or even longer [72, 150]. To completely ignore the effect of the steric force, the microbubble and cell separation distance D was set at $30nm$. The surface potentials of the lipid membrane and (air) sphere were assumed to be ψ_1=$-45mV$ and ψ_3 =$-20mV$ respectively, $1/\kappa$ for the PBS solution was around $0.75nm$ [152]. ε_1 is 1, ε_2 is 80, while ε_3 is 2.2. n_1 is 1, n_2 is 1.33, and n_3 is 1.46 separately. At 4^oC, K_BT was $3.82\times10^{-21}N\cdot m$. As a result, if the collision area is considered to be the microbubble project area, the CII pressure will be $1.73\times10^5N/m^2$.

5.2.5 Cell models and cell membrane mechanical properties

In ANSYS®, cell deformation follows a standard stress balance relationship as shown in Eq. 5-1. In this study, the cell solid was modeled as an isotropic elastic material because many other researchers have done so [191-194, 196, 197]. The strain and stress obey the constitutive equations as in Eq. 5-2. Trickey et al. measured the Poisson ratio for the

cell as around 0.36-0.38 [219]. The values of $E_{membrane}$ and $G_{membrane}$ were defined based on the experimental testing results. Dailey et al. performed a detailed survey of the experimental measurements. The published results range from tens of N/m^2 to a few kN/m^2 [197].

In addition to the lipid double layer, the cortex region, typically with a thickness of 100*nm* below the cell membrane, also contributes greatly to the cell structure behavior [197]. In this thesis, the cortex and cell membrane are considered together as a shell surrounding the cell solid. To closely match the theoretical membrane properties with the measured membrane resistant for expansion, bending or angular movement, Dailey et al. proposed modeling the cell membrane as an orthotropic material with the strain-stress relationship in Eq. 5-4. In this thesis, $E_{membrane}$ and $G_{membrane}$ are made identical on the *x*, *y* and *z* three directions.

$E_{membrane}, G_{membrane}, E_{cell}$ and *h* are varied in order to explore the cell structure behavior. When one property is changed, the other parameters are set at basic values. The basic values for these four properties are listed in Table 5-2.

Cell mechanical property	Basic value
$E_{membrane}$	$4.5\times10^{6}N/m^{2}$
$G_{membrane}$	$20N/m^{2}$
E_{cell}	$200N/m^{2}$
h	$100nm$

Table 5-2 Basic values for cell mechanical properties

5.2.6 Evaluation method

For the results calculated in this study, cell membrane permeability was evaluated based on the equivalent strain or Von Mises strain on the membrane. The equivalent strain could be obtained by following Eq. 5-5: where $\varepsilon_1, \varepsilon_2, \varepsilon_3$ are the principal strains from the ANSYS® calculation results and ν is the pre-set Poisson's ratio.

$$\varepsilon_e = \frac{1}{1+\nu}\left\{\frac{1}{2}\left[(\varepsilon_1-\varepsilon_2)^2+(\varepsilon_2-\varepsilon_3)^2+(\varepsilon_3-\varepsilon_1)^2\right]\right\}^{1/2} \quad (5\text{-}5)$$

After equivalent strain was calculated in all the nodes, the strain distribution on the cell membrane was plotted. The maximum value on the strain distribution plot was defined as the maximum localized strain, while the average strain was defined as the average value of all the equivalent strains available. The effect of cell deformed morphology and cell

mechanical properties on the structural behavior was evaluated by comparing the resulting average strain and maximum strain.

5.3 Simulation results

The comparison was first made by varing the cell membrane elastic modulus $E_{membrane}$ on the two deformed cell types. Fig. 5-3 shows the average and maximum strain on the cell membrane as the $E_{membrane}$ increases. Generally, increasing $E_{membrane}$ decreases the average strain for both deformation type I and deformation type II cells (See Fig. 5-3a). For the deformation type I cell, the greatest average strain is around 14%. When $E_{membrane}$ is increased to $4.5\times10^{8} N/m^{2}$, the average strain for the deformation type I cell is just 2%. The deformation type II cell experienced a higher average strain than deformation type I cell under the same $E_{membrane}$, except at the starting point where $E_{membrane}$ =$4.5\times10^{4} N/m^{2}$. The gap of the average strain between the deformation type I and deformation type II cells fluctuates at around 2%-4%. Fig. 5-3b presents the results of the maximum strain on the cell membrane of both types of deformed cells. The deformation type I and deformation type II cells show different trends for the maximum strain as the $E_{membrane}$ changes. Overall, the maximum strain for the deformation type I cell decreases as $E_{membrane}$ increases. By

contrast, the maximum strain for the deformation type II cell fluctuates as $E_{membrane}$ increases. No consistent trend is observed on this curve. The maximum strain for the deformation type I cell is higher than that for the deformation type II cell in the relatively low $E_{membrane}$ region. The turning point is located at $E_{membrane}$ =9×10^4N/m^2. After that, the maximum strain from deformation type II cell is always higher than the one for deformation type I cell.

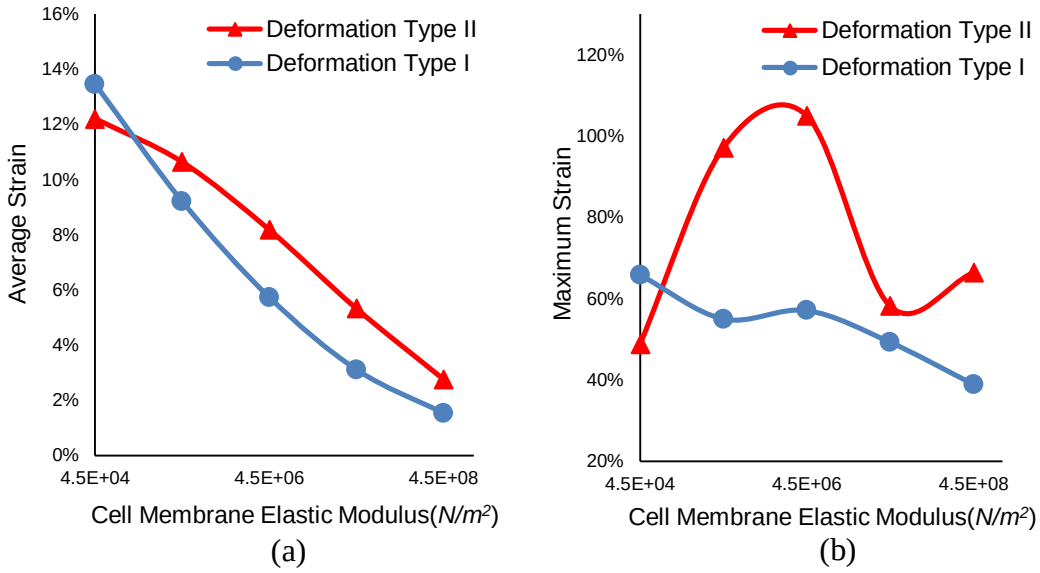

Figure 5-3 (a) average strain on cell membrane of deformation type I and deformation type II cell by varing cell membrane elastic modulus $E_{membrane}$; (b) maximum strain on cell membrane of deformation type I and deformation type II cell by varing cell membrane elastic modulus $E_{membrane}$.

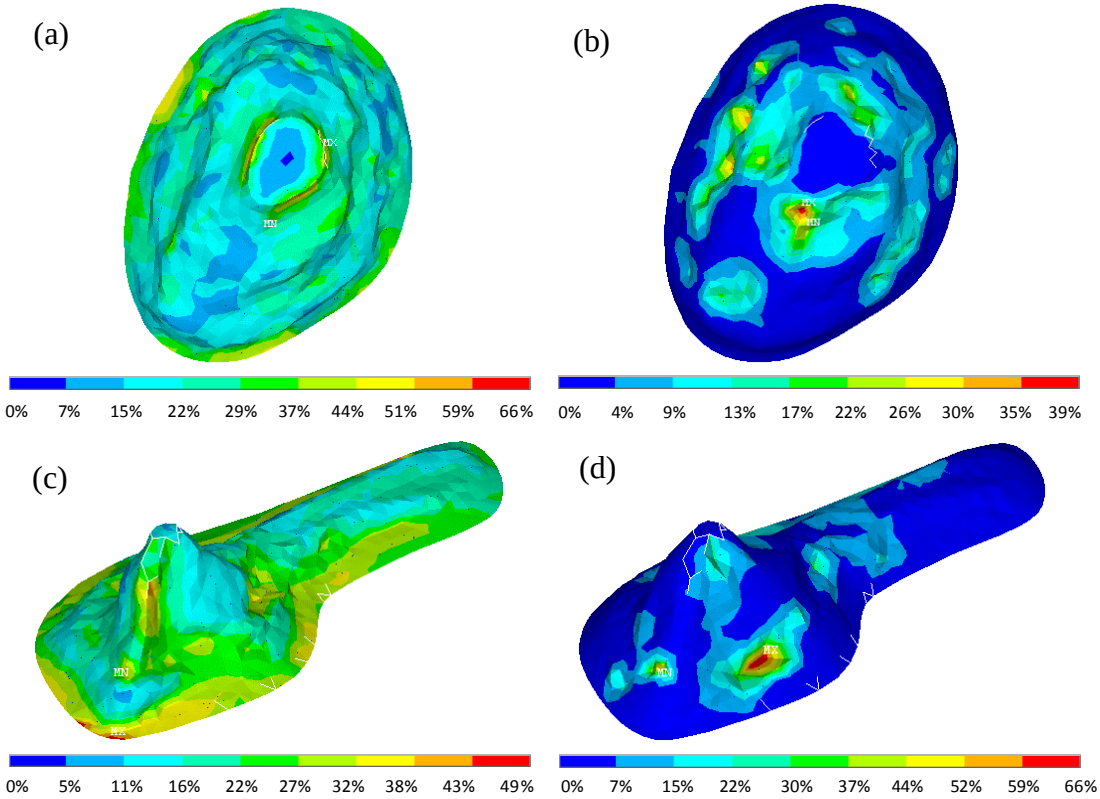

Figure 5-4 (a) equivalent strain distribution on the cell membrane of deformation type I cell when $E_{membrane}$ =4.5×10^4*N/m*^{2}; (b) equivalent strain distribution on the cell membrane of deformation type I cell when $E_{membrane}$ =4.5×10^8*N/m*^{2}; (c) equivalent strain distribution on the cell membrane of deformation type II cell when $E_{membrane}$ =4.5×10^4*N/m*^{2}; (d) equivalent strain distribution on the cell membrane of deformation type II cell when $E_{membrane}$ =4.5×10^8*N/m*^{2}.

Fig. 5-4a-d, reveals a clear change in the equivalent strain distribution on the cell membrane as the cell membrane elastic modulu $E_{membrane}$ increases. When the cell membrane is set with a low cell membrane elastic modulus $E_{membrane}$, all the cell surfaces of both the deformation type I and deformation type II cells undergo relatively large and uniform deformations.

After the cell membrane elastic modulus $E_{membrane}$ reaches $4.5\times10^{8} N/m^{2}$, the equivalent strain distribution is greatly changed. The high equivalent strain area, instead of spreading on the whole cell membrane, is very localized only in certain regions on the cell membrane. The highest equivalent strain of the deformation type I and deformation type II cell is both located on the side wall of the cell model.

The results of the average strain and maximum strain by varying the cell membrane shear modulus $G_{membrane}$ are shown in Fig. 5-5. When $G_{membrane}$ is varied, all the other cell mechanical properties are set at baseline values. By increasing $G_{membrane}$, both the average strain and maximum strain in the two deformed types of cells are decreased. The deformation type II cell undergoes a general 2% larger average strain than the deformation type I cell under all the $G_{membrane}$ tested.

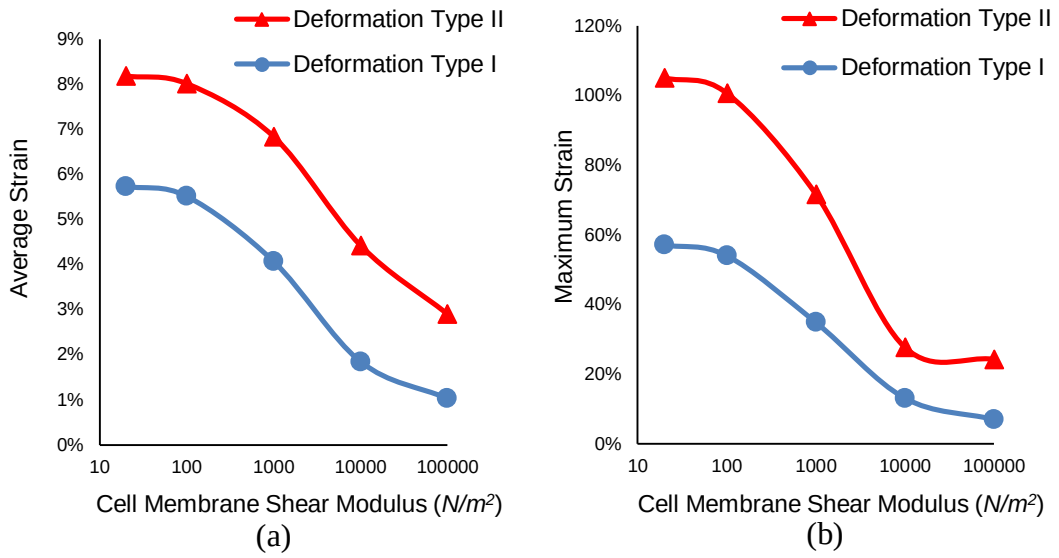

Figure 5-5 (a) average strain on cell membrane of deformation type I and deformation type II cell by varing cell membrane shear modulus $G_{membrane}$; (b) maximum strain on cell membrane of deformation type I and deformation type II cell by varing cell membrane shear modulus $G_{membrane}$.

The changing of equivalent strain distribution on the cell membrane by varing the cell membrane shear modulus $G_{membrane}$ is shown in Fig.5-6. Fig.5-6a,b present the equivalent strain distribution on the cell membrane of the deformation type I cell when $G_{membrane}$ is $20N/m^2$ and $10^5 N/m^2$. The same condition was applied to the deformation type II cell, and the results are shown in Fig. 5-6c,d. Generally, the equivalent strain intensive area decreases as the membrane shear modulus $G_{membrane}$ increases. This result

is rational, because increasing the $G_{membrane}$ increases the cell's ability to resist the shear force.

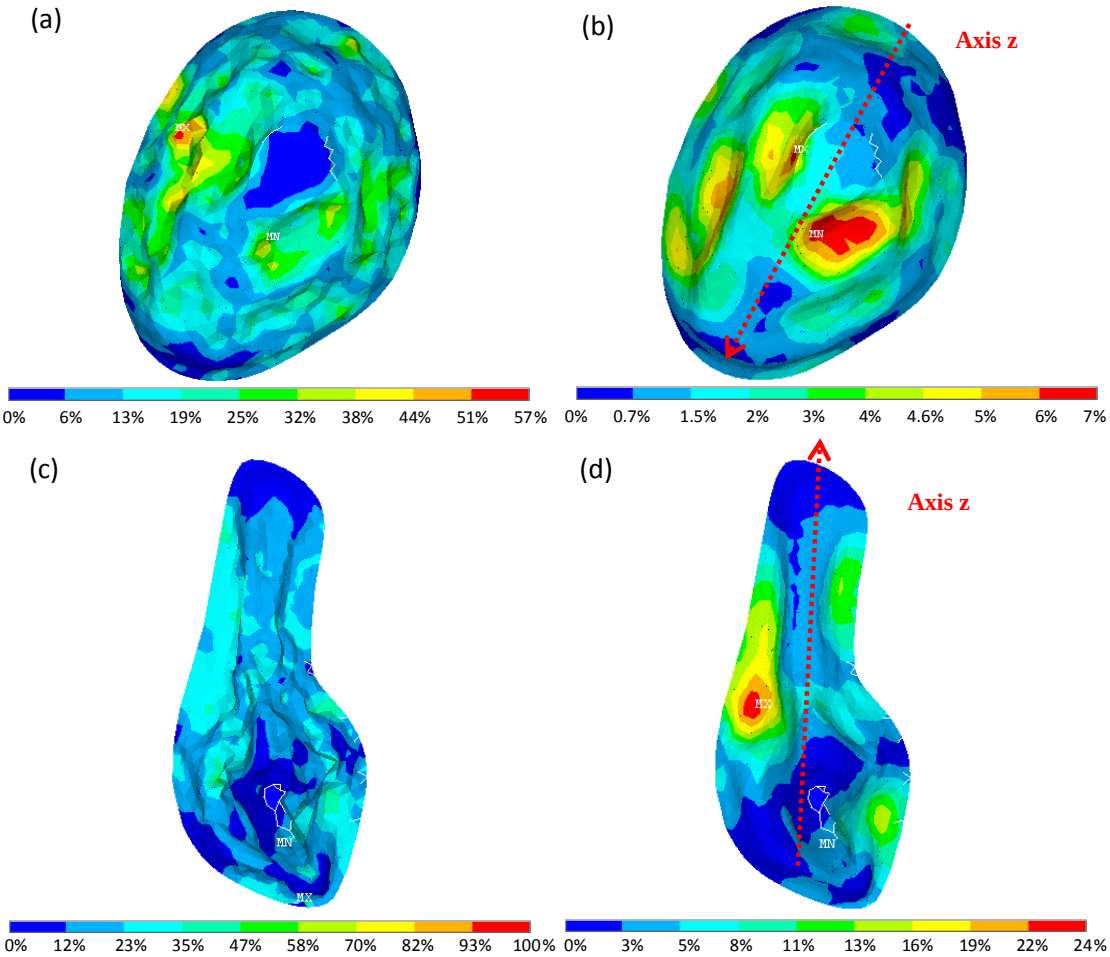

Figure 5-6 (a) equivalent strain distribution on the cell membrane of deformation type I cell when $G_{membrane}=20N/m^2$; (b) equivalent strain on the cell membrane of deformation type I cell when $G_{membrane}=10^5N/m^2$; (c) equivalent strain on the cell membrane of deformation type II cell when $G_{membrane}=20N/m^2$; (d) equivalent strain on the cell membrane of deformation type II cell when $G_{membrane}=10^5N/m^2$.

This result is also similar to the trend observed when the membrane elastic modulus $E_{menbrane}$ is varied. Interestingly, when the membrane shear modulus $G_{membrane}$ is high, the equivalent strain intensive area is not only greatly minimized, but also tends to be localized in the cell elongation region. As shown in Fig. 5-6b, for the deformation type I cell, the direction of the elongation is towards the bottom-left corner (pointed out by axis z). The high equivalent strain areas are almost axissymmetric with the axis z and located on the side-wall of the cell. This phenomenon is even more obvious on the deformation type II cell. The elongation effect gives the cell a spindle morphology. As a result, a relatively thin and long region is formed. Fig. 5-6d reveals that, starting from the spindle-shaped head and extending toward the spindel-shaped tail, a major part of the high equivalent strain areas is located on the two sides of axis z (cell elongation direction). These results reveal that under the same CII pressure, both sides of the cell elongaion region are more fragile than the other regions on the cell membrane.

In Fig. 5-7a,b, the cell elastic modulus E_{cell} is varied from 200 to 1000N/m^2. Like the results obtained above, for both types of deformed cells, the avearge and maximum strain decrease as the cell elastic modulus E_{cell} increases. Small cell elastic modulus E_{cell} can generate high strains.

However, the strain value quick drops down as the E_{cell} increases. the average strain value in the deformation type II cell is still higher, compared to the value obtained under the same conditions for the deformation type I cell. In the last set of comparison, the average and maximum strain values were compared by varying the cell membrane thickness *h*. Fig. 5-7c,d show that increasing the membrane thickness decreases the average strain for both types of deformed cells. For the deformation type I cell, the average strain decreases from 9% to 4%, while for the deformation type II cell, the average strain decreases from 11% to 6%.

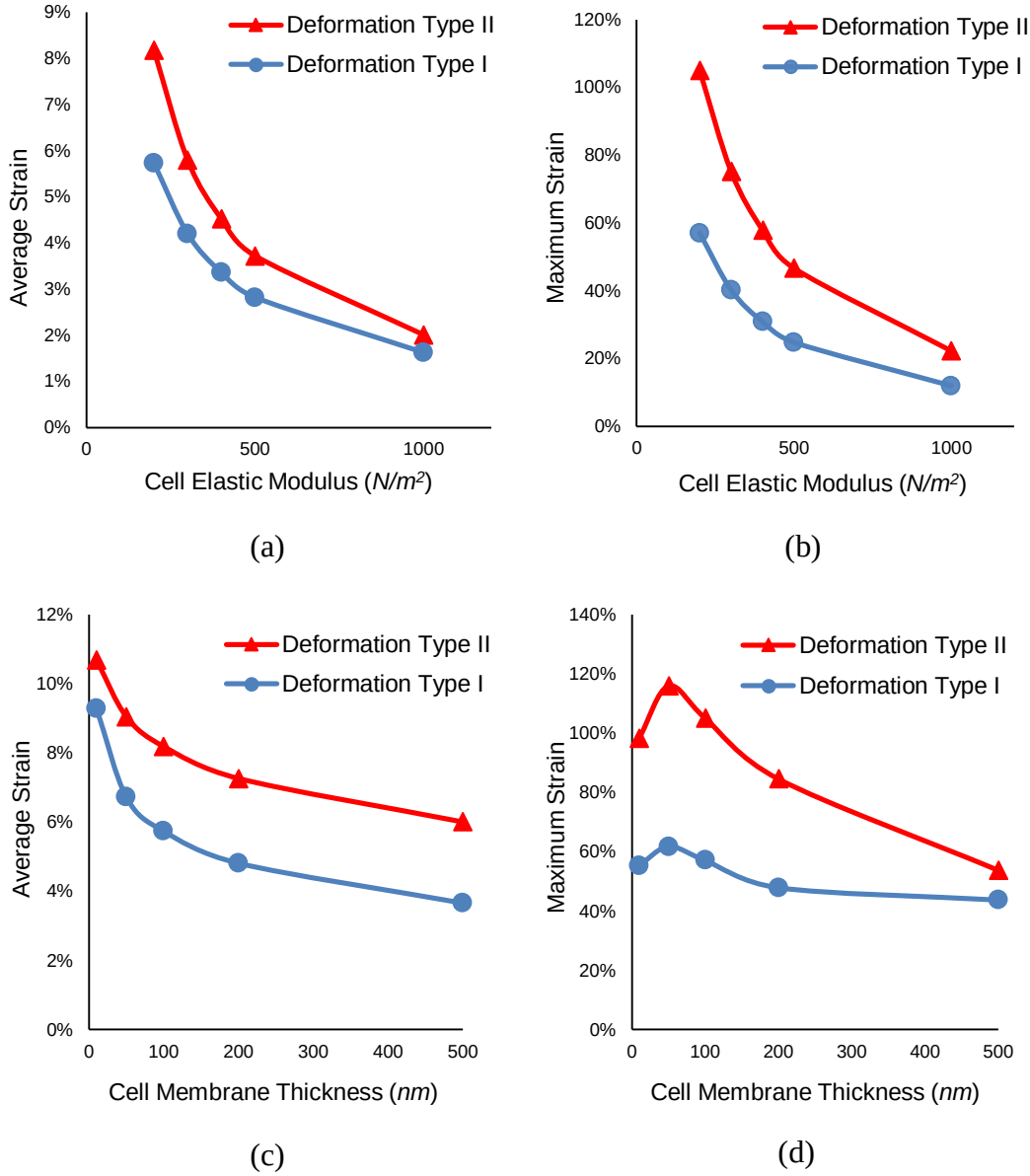

Figure 5-7 (a) average strain on cell membrane of deformation type I and deformation type II cell by varing cell elastic modulus E_{cell} ; (b) maximum strain on cell membrane of deformation type I and deformation type II cell by varing cell elastic modulus E_{cell} ; (c) average strain on cell membrane of deformation type I and deformation type II cell by varing membrane thickness *h*; (d) maximum strain on cell membrane of deformation type I and deformation type II cell by varing membrane thickness *h*.

Interestingly, the maximum strain for both types of deformed cells slightly increase when the cell memrane gets thicker. However, the value of maximum strain quickly drops down after reaching the peak value.

5.4 Discussion

5.4.1 The effect of cell deformed morphology on the cell membrane permeability

One of the aims of this study is to investigate the role of cell deformed morphology induced by the centrifugation field on the cell membrane permeability. To simply quantify the degree of cell deformation, parameter named $o(c)$ was defined for this study. This value is calculated by simply dividing the cell model maximum length by the width as shown in Eq. 5-6. The results for the deformation type I and deformation type II cell are listed in Table 5-3.

$$o(c)=\frac{\text{Maximum length}}{\text{Width}} \tag{5-6}$$

	Deformation type I cell	Deformation type II cell
$o(c)$	1.35	3.43

Table 5-3 $o(c)$ values for deformation type I and deformation type II cells

In a higher centrifugation field, cell deformation is more serious than in a lower centrifugation field. The cell shape is much closer to a spindle. If one cell is more deformed than another, the maximum length will be longer, while the width will be shorter. As expected, $o(c)$ indicated that deformation type II cell is more deformed than the deformation type I cell. Results in Fig. 5-3, Fig. 5-5 and Fig. 5-7 indicate that given the same CII pressure and mechanical properties, the deformation type II cell generally undergoes a higher average strain than the deformation type I cell. If the strain on cell membrane is correlated with cell membrane permeability as mentioned in [197], extracellular materials are easier to be delivered into the deformation type II cell than to the deformation type I cell. This observation accords with our experimental results [214]. The delivery efficiency of FITC-dextran is higher for the MCF-7 cells treated under 9056*g* than the ones treated under 252*g*.

Results in Fig. 5-4 and Fig. 5-6 suggest that the cell morphology elongation effect also play a major role in the localized increase of cell membrane permeability, especially when the cell membrane has a large elastic modulus $E_{membrane}$ or shear modulus $G_{membrane}$. When the cell mechanical properties are with low values, almost everywhere on the cell surface experiences high strain. If the cell mechanical properties are with high modulus which make the cell a stiffer solid, Fig. 5-4 presents that

most of the strain intensive areas are along the elongation region of the deformation type I cell. As explained in the section 5.3, this trend is more significantly shown by the deformation type II cell (Fig. 5-6d). These simulation results correlate well with the previously taken confocal microscope images. As Fig. 3-5c shows, most of the delivered FD is located along the side of the cell in the cell elongation region. The MCF-7 results are shown in Fig. 3-5g. Based on the mage, most of the cells have recovered their round morphology. For the cells successfully delivered with FD, the FD is located in only limited cell region. This phenomenon indicates that the cell membrane permeability is greatly increased in a limited region. Compared with our simulation result, a speculation might be drawn that the regions with FD delivered might be the one that is elongated during the centrifugation field.

These simulation results confirm our original speculation that the degree of cell deformation will have a critical effect on cell membrane permeability. The deformation type II cell is more elongated or stretched than deformation type I cell. As a result, the deformation type II cell undergoes a higher average strain than the deformation type I cell. The localized high strain area tends to be located in the cell extended region in both types of deformed cells. By controlling the cell morphology, a researcher might

control the delivery of extracellular materials into certain regions of the cells.

5.4.2 The effect of cell mechanical properties on the cell membrane permeability

Another aim of this study is to investigate the effect of cell mechanical properties on cell membrane permeability. Unlike the trend reported by Dailey et al. [197], no consistent trend was found for the maximum strain when varying the cell mechanical properties in this thesis. For the deformation type II cell, when the cell membrane elastic modulus $E_{membrane}$ and membrane thickness h were increased, the value of the maximum strain on cell membrane also increased at some points instead of decreasing. This phenomenon indicates that the cell mechanical properties alone cannot totally determine the strain value. Generally, increasing the cell mechanical properties will make a cell more tolerant of the external forces. This is demonstrated by the simulation results in Fig. 5-3, 5-5 and 5-7. When the cell membrane elastic modulus $E_{membrane}$, shear modulus $G_{membrane}$, cell solid elastic modulus E_{cell}, or membrane thickness h increased, the averaged strain on the cell membrane decreased. As Fig. 5-4 shows, after increasing the cell membrane elastic modulus $E_{membrane}$, although most of the cell regions experience a relatively small strain, the

cell's deformed morphology causes certain regions to experience an extremely high strain. The membrane area experiencing a localized high strain is most likely to be penetrated. In Fig. 3-5c and g, most of the FD delivered inside the cells exists in small blocks, possibly because only a small region on the membrane is opened, so the FD has to enter the cell through a thin channel and thus accumulates in the same cell region.

These results show that cell mechanical properties are important for cell membrane permeability. Although the average strain is decreased as the cell mechanical properties increase, the maximum strain is a synergistic effect of cell morphology and cell mechanical properties. Modifying the cell mechanical properties will also change cell membrane permeability.

5.4.3 Model limitations

In this study, a confocal microscope images-based method was used to build a cell deformation model to enhance our understanding of cell and microbubble interaction in a high centrifugation field. As Dailey et al. mention, this method has some common limitations [197]. Several assumptions must be made to make the simulation more applicable. First, a cell is assumed to be isotropic elastic material, but, in reality, a cell has a highly inhomogeneous structure. However, the cell has been modeled as a homogeneous medium in many studies [191-194, 196, 197]. Second, no

experimental measurements of the mechanical properties of MCF-7 are available. Thus, the parameters were estimated based on the literature review. The parameters were varied in a broad range so that the cell response could be observed. The results indicate that cell morphology and cell mechanics simultaneously decide the range and distribution of the cell membrane strain. The strain contour plot accords well with the captured confocal microscope image. Finally, only the cell upside body is considered in this interaction. Generally, cells go through two stages during centrifugation. During the first stage, the cell flows towards the centrifuge wall, and during the second stage, the cell glides along the centrifuge wall. The cell motion in the centrifuge tube is very complex. If the cell rotation is ignored, only half of the cell body will interact with the microbubble because the cell and microbubble are moving towards each other. Since a collision might happen on any region of the cell upper body, the collision results in pressure on the cell membrane. As the focus of this investigation is on the interaction between microbubbles and cells, the half of the cell which is attached to the centrifuge tube surface was ignored.

5.5 Conclusions

In this study, the effects of cell deformed morphology and mechanical properties on cell membrane permeability were investigated. The

structural behaviors of cells which were deformed to different degrees, such as deformation type I cell and deformation type II cell were compared. The results indicated that both cell morphology and cell mechanical properties played an important role in the range of the strain values and strain distributions on the cell membrane. Generally, under the same CII pressure, cell with more deformed morphology experienced a higher strain than the less deformed cell. This result was supported by our previous experimental data, which showed that a higher centrifugation field resulted in higher intracellular delivery efficiency. As the value of the cell mechanical properties increased, the average strain on the cell membrane decreased. However, the maximum localized strain was further increased in some conditions, possibly because of the synergistic effect of cell morphology and cell mechanics. The strain intensive areas were more likely to be located along the cell elongation region induced by the centrifugation process. This simulation results were also supported by the confocal microscope images. These results increased our understanding of how the CII pressure and high centrifugation field help to increase cell membrane permeability.

Chapter 6

VI. Conclusions and future work

6.1 Conclusions

Low cell membrane permeability is one of the major obstacles for successful gene therapy. In this thesis, two methods to increase cell membrane permeability were developed.

In the first method, an innovative purification process of mCNT extraction from purchased raw arc-discharged CNT materials was demonstrated. The process is divided into three main procedures: SDS treatment, organic solvent treatment, and H_2O_2 treatment. To maintain the magnetic particles, a harsh acid treatment was avoided although it is considered as a commonly used traditional purification method. A method to monitor the purification process by combining AFM-FCA with TEM images was also developed. The advantage of this method is that it can directly differentiate mCNT once the standard material analysis is performed. Our experimental results are in line with the theoretical estimation. The developed mCNT was tested on various cell lines. FITC was used to assist the quantification

and observation of the delivery results. The results indicated that the developed mCNT efficiently increased the cell membrane permeability.

In the second method, cell membrane permeability was increased by using a microbubble-assisted high centrifugation field. The increase in cell membrane permeability was demonstrated by the successful delivery of FD (40*kDa*) into hard-to-deliver THP-1 cells, and FD (40*kDa* and 70*kDa*) into MCF-7 cells. A simplified model of the cell-microbubble interaction in a high centrifugation field estimated that once the relative velocity between a cell and a microbubble reached a critical value, the collision-induced hydrodynamic force would be large enough to penetrate the cell membrane and create intracellular pathways. The same method was applied on canola plant cells. Biomaterial with a size up to 250*kDa* was successfully delivered into 90% canola protoplasts and canola cells with cell walls. The delivery efficiency was similar within the broad range of centrifugation speeds and amounts of microbubble solution. The FACS histogram shows an obvious difference on fluorescence signal between the cells centrifuged alone and cells centrifuged with microbubbles. This result means the permeability of the cell membrane or the cell wall permeability was further increased.

To investigate the effect of cell deformed morphology and mechanical properties on cell membrane permeability, confocal microscope images

were used to build cell deformation models in a high centrifugation field. The structural behaviors of cells with different deformations such as deformation type I cell and deformation type II cell were studied. The results indicated that both cell morphology and cell mechanical properties played an important role in deciding the range of the strain value and strain distribution on the cell membrane. Under the same CII pressure, the cells with the more deformed morphology experienced a higher strain than the less deformed cells. This finding was supported by our experimental results, which showed that a higher centrifugation speed resulted in higher intracellular delivery efficiency. It was also found that, as the cell mechanical properties increased, the average strain decreased. However, the maximum localized strain was increased in some conditions, possibly because of the synergistic effect of cell morphology and cell mechanics. Based on the strain distribution on the cell membrane, the strain intensive areas were more likely to be located along the cell elongation region. This observation was also supported by the confocal microscope images, as most of the delivered FD was located in the cell extension region near the inner border of the cell membrane. In summary, the results showed that the CII pressure and high centrifugation field helped to increase the cell membrane permeability. This simulation study helps us to better

understand the cell and microbubble interaction in a high centrifugation field.

6.2 Future work

Two methods to increase cell permeability were successfully developed in this thesis, but many important and interesting problems still require further investigation.

In Chapter 2, mCNT was successfully extracted from raw materials, and the ability of mCNT to increase cell membrane permeability was tested. However, in order to apply this technique to gene therapy, efficient protocols need to be developed to combine the genetic biomaterial with the mCNT. In addition, the mCNT developed in this thesis were bundled together. Further treatment might help to separate the bundled nanotubes into smaller SWNT which would facilitate the cell endocytosis process. However, if the bundled mCNTs are separated, the amount of nickel on each CNT will decrease and make the CNT less responsive to a given magnetic field. As a result, a whole new process is required in order to overcome these trade-off problems.

In Chapter 3 and Chapter 4, a method using a microbubble-assisted high centrifugation field to increase cell membrane permeability was presented. This method can create intracellular pores even on hard cell walls. Further

studies can focus on optimizing the experimental protocols based on the application requirements. For example, for mammalian cells, although high efficiency can be achieved, cell viability is low at the same time. Moreover, special centrifugation tools can be developed to increase the interaction duration between microbubbles and cells. For example, in the current commercialized centrifuge and centrifuge tube, the cells gather together quickly and slide along the centrifuge tube wall into the bottom of the centrifuge tube in a very short time. If the tube is long enough or has a spiral structure, the cells and microbubbles will have more opportunities to interact with each other even in a low centrifugation field. As a result, the CII will have more effect on the cell membrane.

Finally, the results of Chapter 5 indicated that both cell deformed morphology and mechanical properties had an impact on cell membrane permeability. This result indicated that the cells could have been pretreated with chemicals to modify their internal structure before treating them with the two physically-based methods developed in this thesis. In addition, cell membrane permeability could be increased locally on the cell membrane by modifying the cell morphology. For example, by incubating cells in a predesigned container, cell morphology can be controlled. This pre-treatment could create certain regions on the cell membrane that would be more vulnerable compared to other regions. Thus, a physically-

based method could target these weak regions to maximize the efficiency while decreasing the side effects at the same time.

References

1. Blaese, R.M., et al., *T-Lymphocyte-Directed Gene-Therapy for Ada(-) Scid - Initial Trial Results after 4 Years.* Science, 1995. **270**(5235): p. 475-480.
2. Bennett, J., et al., *AAV2 Gene Therapy Readministration in Three Adults with Congenital Blindness.* Science Translational Medicine, 2012. **4**(120).
3. Taira, K., K. Kataoka, and T. Niidome, *Non-viral gene therapy gene design and delivery*, 2005, Springer: Tokyo ; New York. p. xii, 487 p.
4. Arjumand, W. and S. Sultana, *Role of VHL gene mutation in human renal cell carcinoma.* Tumor Biology, 2012. **33**(1): p. 9-16.
5. Hacein-Bey-Abina, S., et al., *LMO2-associated clonal T cell proliferation in two patients after gene therapy for SCID-X1.* Science, 2003. **302**(5644): p. 415-419.
6. Kipps, T.J., et al., *CD40-ligand (CD154) gene therapy for chronic lymphocytic leukemia.* Cancer Gene Therapy, 2000. **7**(12): p. S16-S16.
7. Kaplitt, M.G., et al., *Safety and tolerability of gene therapy with an adeno-associated virus (AAV) borne GAD gene for Parkinson's disease: an open label, phase I trial.* Lancet, 2007. **369**(9579): p. 2097-2105.
8. Symonds, G.P., et al., *The use of cell-delivered gene therapy for the treatment of HIV/AIDS.* Immunologic Research, 2010. **48**(1-3): p. 84-98.
9. Griffiths, A.J.F., *Introduction to genetic analysis*. 8th ed2005, New York: W.H. Freeman and Co. xvi, 782 p.
10. Jeong, J.H., S.W. Kim, and T.G. Park, *Molecular design of functional polymers for gene therapy.* Progress in Polymer Science, 2007. **32**(11): p. 1239-1274.
11. Cavazzana-Calvo, M., A. Thrasher, and F. Mavilio, *The future of gene therapy.* Nature, 2004. **427**(6977): p. 779-781.
12. Yaron, P.N., et al., *Single wall carbon nanotubes enter cells by endocytosis and not membrane penetration.* Journal of Nanobiotechnology, 2011. **9**.

13. Hardin, J., *Becker's world of the cell*2012: Benjamin Cummings.

14. Griffith, F., *The Significance of Pneumococcal Types.* Journal of Hygiene, 1928. **27**(2): p. 113-159.

15. Carlson, C.A., et al., *Pseudomonas-Stutzeri and Related Species Undergo Natural Transformation.* Journal of Bacteriology, 1983. **153**(1): p. 93-99.

16. Lorenz, M.G. and W. Wackernagel, *Bacterial Gene-Transfer by Natural Genetic-Transformation in the Environment.* Microbiological Reviews, 1994. **58**(3): p. 563-602.

17. Mandel, M. and A. Higa, *Calcium-Dependent Bacteriophage DNA Infection.* Journal of Molecular Biology, 1970. **53**(1): p. 159-&.

18. Palmen, R., et al., *Physiological Characterization of Natural Transformation in Acinetobacter-Calcoaceticus.* Journal of General Microbiology, 1993. **139**: p. 295-305.

19. Sambrook, J., E.F. Fritsch, and T. Maniatis, *Molecular cloning : a laboratory manual*. 2nd ed1989, Cold Spring Harbor, N.Y.: Cold Spring Harbor Laboratory.

20. Blanco, E., et al., *Nanomedicine in cancer therapy: innovative trends and prospects.* Cancer Sci, 2011. **102**(7): p. 1247-52.

21. Ng, K.K., J.F. Lovell, and G. Zheng, *Lipoprotein-Inspired Nanoparticles for Cancer Theranostics.* Accounts of Chemical Research, 2011. **44**(10): p. 1105-1113.

22. T Al-Jamal, W. and K. Kostarelos, *Liposome-nanoparticle hybrids for multimodal diagnostic and therapeutic applications.* Nanomedicine, 2007. **2**(1): p. 85-98.

23. Muller, R.H., S. Gohla, and C.M. Keck, *State of the art of nanocrystals - Special features, production, nanotoxicology aspects and intracellular delivery.* European Journal of Pharmaceutics and Biopharmaceutics, 2011. **78**(1): p. 1-9.

24. Muller-Goymann, C.C., *Physicochernical characterization of colloidal drug delivery systems such as reverse micelles, vesicles, liquid crystals and nanoparticles for topical administration.* European Journal of Pharmaceutics and Biopharmaceutics, 2004. **58**(2): p. 343-356.

25. Rao, S.P.V.R. and J. Shao, *Self-nanoemulsifying drug delivery systems (SNEDDS) for oral delivery of protein drugs I. Formulation*

development. International Journal of Pharmaceutics, 2008. **362**(1-2): p. 2-9.

26. Byrne, M.E., K. Park, and N.A. Peppas, *Molecular imprinting within hydrogels.* Advanced Drug Delivery Reviews, 2002. **54**(1): p. 149-161.

27. Pannier, A.K. and L.D. Shea, *Controlled release systems for DNA delivery.* Molecular Therapy, 2004. **10**(1): p. 19-26.

28. Wagner, E., *Strategies to improve DNA polyplexes for in vivo gene transfer: Will "artificial viruses" be the answer?* Pharmaceutical Research, 2004. **21**(1): p. 8-14.

29. Brownlie, A., I.F. Uchegbu, and A.G. Schatzlein, *PEI-based vesicle-polymer hybrid gene delivery system with improved biocompatibility.* International Journal of Pharmaceutics, 2004. **274**(1-2): p. 41-52.

30. Ferrari, S., et al., *Polyethylenimine shows properties of interest for cystic fibrosis gene therapy.* Biochimica Et Biophysica Acta-Gene Structure and Expression, 1999. **1447**(2-3): p. 219-225.

31. Gregoriadis, G., *Genetic vaccines: Strategies for optimization.* Pharmaceutical Research, 1998. **15**(5): p. 661-670.

32. Perrie, Y. and G. Gregoriadis, *Liposome-entrapped plasmid DNA: characterisation studies.* Biochimica Et Biophysica Acta-General Subjects, 2000. **1475**(2): p. 125-132.

33. Kircheis, R., L. Wightman, and E. Wagner, *Design and gene delivery activity of modified polyethylenimines.* Advanced Drug Delivery Reviews, 2001. **53**(3): p. 341-358.

34. Arangoa, M.A., N. Duzgunes, and C.T. de Ilarduya, *Increased receptor-mediated gene delivery to the liver by protamine-enhanced-asialofetuin-lipoplexes.* Gene Therapy, 2003. **10**(1): p. 5-14.

35. Ahn, C.H., et al., *Synthesis of biodegradable multi-block copolymers of poly(L-lysine) and poly(ethylene glycol) as a non-viral gene carrier.* Journal of Controlled Release, 2004. **97**(3): p. 567-574.

36. Miyata, K., et al., *Block catiomer polyplexes with regulated densities of charge and disulfide cross-linking directed to enhance gene expression.* Journal of the American Chemical Society, 2004. **126**(8): p. 2355-2361.

37. Putnam, D., et al., *Polyhistidine-PEG : DNA nanocomposites for gene delivery.* Biomaterials, 2003. **24**(24): p. 4425-4433.

38. Rackstraw, B.J., et al., *Development of multicomponent DNA delivery systems based upon poly(amidoamine)-PEG co-polymers.* Biochimica Et Biophysica Acta-Gene Structure and Expression, 2002. **1576**(3): p. 269-286.

39. Adair, J.H., et al., *Nanoparticulate Alternatives for Drug Delivery.* Acs Nano, 2010. **4**(9): p. 4967-4970.

40. Hamidi, M., M.A. Shahbazi, and K. Rostamizadeh, *Copolymers: Efficient Carriers for Intelligent Nanoparticulate Drug Targeting and Gene Therapy.* Macromolecular Bioscience, 2012. **12**(2): p. 144-164.

41. Grossman, P.M., et al., *Results from a phase II multicenter, double-blind placebo-controlled study of Del-1 (VLTS-589) for intermittent claudication in subjects with peripheral arterial disease*. American Heart Journal, 2007. **153**(5): p. 874-880.

42. Herce, H.D. and A.E. Garcia, *Cell Penetrating Peptides: How Do They Do It?* Journal of Biological Physics, 2007. **33**(5-6): p. 345-356.

43. Howl, J., I.D. Nicholl, and S. Jones, *The many futures for cell-penetrating peptides: how soon is now?* Biochemical Society Transactions, 2007. **35**: p. 767-769.

44. Deshayes, S., et al., *Primary amphipathic cell-penetrating peptides: Structural requirements and interactions with model membranes.* Biochemistry, 2004. **43**(24): p. 7698-7706.

45. Milletti, F., *Cell-penetrating peptides: classes, origin, and current landscape.* Drug Discovery Today, 2012. **17**(15-16): p. 850-860.

46. Eguchi, A. and S.F. Dowdy, *siRNA delivery using peptide transduction domains.* Trends in Pharmacological Sciences, 2009. **30**(7): p. 341-345.

47. Mae, M. and U. Langel, *Cell-penetrating peptides as vectors for peptide, protein and oligonucleotide delivery.* Current Opinion in Pharmacology, 2006. **6**(5): p. 509-514.

48. Jarver, P., I. Mager, and U. Langel, *In vivo biodistribution and efficacy of peptide mediated delivery.* Trends in Pharmacological Sciences, 2010. **31**(11): p. 528-535.

49. Iijima, S., *Helical Microtubules of Graphitic Carbon.* Nature, 1991. **354**(6348): p. 56-58.

50. Singh, M., P.K. Kathuroju, and N. Jampana, *Polypyrrole based amperometric glucose biosensors.* Sensors and Actuators B-Chemical, 2009. **143**(1): p. 430-443.

51. Liu, J., et al., *Oriented Nanostructures for Energy Conversion and Storage.* Chemsuschem, 2008. **1**(8-9): p. 676-697.

52. Pantarotto, D., et al., *Functionalized carbon nanotubes for plasmid DNA gene delivery.* Angewandte Chemie-International Edition, 2004. **43**(39): p. 5242-5246.

53. Korneva, G., et al., *Carbon nanotubes loaded with magnetic particles.* Nano Letters, 2005. **5**(5): p. 879-884.

54. Cai, D., et al., *Interaction between carbon nanotubes and mammalian cells: characterization by flow cytometry and application.* Nanotechnology, 2008. **19**(34).

55. Hou, P.X., C. Liu, and H.M. Cheng, *Purification of carbon nanotubes.* Carbon, 2008. **46**(15): p. 2003-2025.

56. Chiang, I.W., et al., *Purification and characterization of single-wall carbon nanotubes (SWNTs) obtained from the gas-phase decomposition of CO (HiPco process).* Journal of Physical Chemistry B, 2001. **105**(35): p. 8297-8301.

57. Rinzler, A.G., et al., *Large-scale purification of single-wall carbon nanotubes: process, product, and characterization.* Applied Physics a-Materials Science & Processing, 1998. **67**(1): p. 29-37.

58. Bonard, J.M., et al., *Purification and size-selection of carbon nanotubes.* Advanced Materials, 1997. **9**(10): p. 827-&.

59. Yu, A.P., et al., *Application of centrifugation to the large-scale purification of electric arc-produced single-walled carbon nanotubes.* Journal of the American Chemical Society, 2006. **128**(30): p. 9902-9908.

60. Lambert, J.M., et al., *Improving Conditions Towards Isolating Single-Shell Carbon Nanotubes.* Chemical Physics Letters, 1994. **226**(3-4): p. 364-371.

61. Shim, H.C., et al., *Purification of carbon nanotubes through an electric field near the arranged microelectrodes.* Nanotechnology, 2007. **18**(11).

62. Hou, P.X., et al., *Multi-step purification of carbon nanotubes.* Carbon, 2002. **40**(1): p. 81-85.

63. Tohji, K., et al., *Purification procedure for single-walled nanotubes.* Journal of Physical Chemistry B, 1997. **101**(11): p. 1974-1978.

64. Hou, P.X., et al., *Purification of single-walled carbon nanotubes synthesized by the hydrogen arc-discharge method.* Journal of Materials Research, 2001. **16**(9): p. 2526-2529.

65. Fan, Y.Y., et al., *Single- and multi-wall carbon nanotubes produced using the floating catalyst method: Synthesis, purification and hydrogen up-take.* Carbon, 2006. **44**(11): p. 2160-2170.

66. Bandow, S., et al., *Purification and magnetic properties of carbon nanotubes.* Applied Physics a-Materials Science & Processing, 1998. **67**(1): p. 23-27.

67. Li, F., et al., *Purification of single-walled carbon nanotubes synthesized by the catalytic decomposition of hydrocarbons.* Carbon, 2000. **38**(14): p. 2041-2045.

68. Zhang, H., et al., *Purification of multiwalled carbon nanotubes by annealing and extraction based on the difference in van der Waals potential.* Journal of Physical Chemistry B, 2006. **110**(19): p. 9477-9481.

69. Veeco, *Veeco diMultiMode V SPM Instruction Manual*2006: Veeco Instruments Inc.

70. Radmacher, M., et al., *Mapping Interaction Forces with the Atomic-Force Microscope.* Biophysical Journal, 1994. **66**(6): p. 2159-2165.

71. Johnson, K.L., K. Kendall, and A.D. Roberts, *Surface Energy and Contact of Elastic Solids.* Proceedings of the Royal Society of London Series a-Mathematical and Physical Sciences, 1971. **324**(1558): p. 301-&.

72. Israelachvili, J.N., *Intermolecular and surface forces*. 3rd ed2011, Waltham, MA: Academic Press. xxx, 674 p.

73. Akita, S., H. Nishijima, and Y. Nakayama, *Influence of stiffness of carbon-nanotube probes in atomic force microscopy.* Journal of Physics D-Applied Physics, 2000. **33**(21): p. 2673-2677.

74. Perry, S.S., et al., *Adhesion and friction properties of hydrogenated amorphous carbon films measured by atomic force microscopy.* Tribology Letters, 1995. **1**(2-3): p. 233-246.

75. Yaung, J.H., L. ; Jeon, J. ; Liu, T.-J.K., *Adhesive Force Characterization for MEM Logic Relays With Sub-Micron*

Contacting Regions. Journal of Microelectromechanical Systems, 2013. **PP**(99): p. 1.

76. Decossas, S., et al., *Interaction forces between carbon nanotubes and an AFM tip.* Europhysics Letters, 2001. **53**(6): p. 742-748.

77. Cheng, Q.H., et al., *Ultrasound-Assisted SWNTs Dispersion: Effects of Sonication Parameters and Solvent Properties.* Journal of Physical Chemistry C, 2010. **114**(19): p. 8821-8827.

78. Feng, Y.Y., et al., *Room temperature purification of few-walled carbon nanotubes with high yield.* Acs Nano, 2008. **2**(8): p. 1634-1638.

79. Dillon, A.C., et al., *A simple and complete purification of single-walled carbon nanotube materials.* Advanced Materials, 1999. **11**(16): p. 1354-1358.

80. Gavillet, J., et al., *TEM study of the influence of the catalyst composition on the formation and growth of SWNT.* Structural and Electronic Properties of Molecular Nanostructures, 2002. **633**: p. 202-206.

81. Sen, R., et al., *Controlled purification of single-walled carbon nanotube films by use of selective oxidation and near-IR spectroscopy.* Chemistry of Materials, 2003. **15**(22): p. 4273-4279.

82. Dujardin, E., et al., *Purification of single-shell nanotubes.* Advanced Materials, 1998. **10**(8): p. 611-+.

83. Wang, Y.H., et al., *A highly selective, one-pot purification method for single-walled carbon nanotubes.* Journal of Physical Chemistry B, 2007. **111**(6): p. 1249-1252.

84. Kubo, Y., et al., *Application of Membrane Permeability Evaluated in In Vitro Analyses to Estimate Blood-Retinal Barrier Permeability.* Journal of Pharmaceutical Sciences, 2012. **101**(7): p. 2596-2605.

85. Hao, Y.Z., et al., *FITC Delivery into Plant Cells Using Magnetic Single-Walled Carbon Nanotubes.* Journal of Nanoscience and Nanotechnology, 2012. **12**(8): p. 6287-6293.

86. Hao, Y.Z., et al., *Impact of carbondiimide crosslinker used for magnetic carbon nanotube mediated GFP plasmid delivery.* Nanotechnology, 2011. **22**(28).

87. Weaver, J.C., *Electroporation of biological membranes from multicellular to nano scales.* Ieee Transactions on Dielectrics and Electrical Insulation, 2003. **10**(5): p. 754-768.

88. Baker, P.F. and D.E. Knight, *A high-voltage technique for gaining rapid access to the interior of secretory cells [proceedings].* J Physiol, 1978. **284**: p. 30P-31P.

89. Baker, P.F. and D.E. Knight, *Influence of anions on exocytosis in 'leaky' bovine adrenal medullary cells [proceedings].* J Physiol, 1979. **296**(Nov): p. 106P-107P.

90. Wegener, J., C.R. Keese, and I. Giaever, *Recovery of adherent cells after in situ electroporation monitored electrically.* Biotechniques, 2002. **33**(2): p. 348-+.

91. Tarek, M., *Membrane electroporation: A molecular dynamics simulation.* Biophysical Journal, 2005. **88**(6): p. 4045-4053.

92. Teissie, J., M. Golzio, and M.P. Rols, *Mechanisms of cell membrane electropermeabilization: A minireview of our present (lack of ?) knowledge.* Biochimica Et Biophysica Acta-General Subjects, 2005. **1724**(3): p. 270-280.

93. Cukjati, D., et al., *Real time electroporation control for accurate and safe in vivo non-viral gene therapy.* Bioelectrochemistry, 2007. **70**(2): p. 501-507.

94. Favard, C., D.S. Dean, and M.P. Rols, *Electrotransfer as a non viral method of gene delivery.* Current Gene Therapy, 2007. **7**(1): p. 67-77.

95. Chen, C., et al., *Membrane electroporation theories: a review.* Medical & Biological Engineering & Computing, 2006. **44**(1-2): p. 5-14.

96. Schakowski, F., et al., *A novel non-viral method for transfection of primary acute leukemia cells and cell lines shows high transgene expression and low toxicity.* Blood, 2001. **98**(11): p. 406b-406b.

97. El-Kamary, S.S., et al., *Safety and Tolerability of the Easy Vax (TM) Clinical Epidermal Electroporation System in Healthy Adults.* Molecular Therapy, 2012. **20**(1): p. 214-220.

98. Thomson, K. and S.T. Kee, *Clinical Research on Irreversible Electroporation of the Liver.* Clinical Aspects of Electroporation, 2011: p. 237-246.

99. Zeira, E., et al., *Femtosecond infrared laser - An efficient and safe in vivo gene delivery system for prolonged expression.* Molecular Therapy, 2003. **8**(2): p. 342-350.

100. Sboros, V., *Response of contrast agents to ultrasound.* Advanced Drug Delivery Reviews, 2008. **60**(10): p. 1117-1136.

101. Joersbo, M. and J. Brunstedt, *Sonication - a New Method for Gene-Transfer to Plants.* Physiologia Plantarum, 1992. **85**(2): p. 230-234.

102. Price, R.J., et al., *Delivery of colloidal particles and red blood cells to tissue through microvessel ruptures resulting from microbubble destruction by ultrasound.* Circulation, 1998. **98**(17): p. 570-570.

103. van Wamel, A., et al., *Vibrating microbubbles poking individual cells: Drug transfer into cells via sonoporation.* Journal of Controlled Release, 2006. **112**(2): p. 149-155.

104. Prentice, P., et al., *Membrane disruption by optically controlled microbubble cavitation.* Nature Physics, 2005. **1**(2): p. 107-110.

105. Qiu, Y.Y., et al., *The correlation between acoustic cavitation and sonoporation involved in ultrasound-mediated DNA transfection with polyethylenimine (PEI) in vitro.* Journal of Controlled Release, 2010. **145**(1): p. 40-48.

106. Doinikov, A.A. and A. Bouakaz, *Theoretical investigation of shear stress generated by a contrast microbubble on the cell membrane as a mechanism for sonoporation.* Journal of the Acoustical Society of America, 2010. **128**(1): p. 11-19.

107. Landini, L., M.F. Santarelli, and V. Positano, *Ultrasound techniques for drug delivery in cardiovascular medicine.* Curr Drug Discov Technol, 2008. **5**(4): p. 328-32.

108. Tachibana, K. and S. Tachibana, *Albumin Microbubble Echo-Contrast Material as an Enhancer for Ultrasound Accelerated Thrombolysis.* Circulation, 1995. **92**(5): p. 1148-1150.

109. Larina, I.V., B.M. Evers, and R.O. Esenaliev, *Optimal drug and gene delivery in cancer cells by ultrasound-induced cavitation.* Anticancer Research, 2005. **25**(1A): p. 149-156.

110. Taniyama, Y., et al., *Plasmid DNA-based Gene Transfer with Ultrasound and Microbubbles.* Current Gene Therapy, 2011. **11**(6): p. 485-490.

111. Lee, P.W., et al., *The use of biodegradable polymeric nanoparticles in combination with a low-pressure gene gun for transdermal DNA delivery.* Biomaterials, 2008. **29**(6): p. 742-751.

112. Wang, K. and B. Frame, *Biolistic Gun-Mediated Maize Genetic Transformation.* Transgenic Maize: Methods and Protocols, 2009. **526**: p. 29-45.

113. Sims, N.R. and M.F. Anderson, *Isolation of mitochondria from rat brain using Percoll density gradient centrifugation.* Nature Protocols, 2008. **3**(7): p. 1228-1239.

114. Xiong, B., et al., *Separation of nanorods by density gradient centrifugation.* Journal of Chromatography A, 2011. **1218**(25): p. 3823-3829.

115. Feshitan, J.A., et al., *Microbubble size isolation by differential centrifugation.* Journal of Colloid and Interface Science, 2009. **329**(2): p. 316-324.

116. Hoffman, J.F. and S. Inoue, *Directly observed reversible shape changes and hemoglobin stratification during centrifugation of human and Amphiuma red blood cells.* Proceedings of the National Academy of Sciences of the United States of America, 2006. **103**(8): p. 2971-2976.

117. Richter, H.P., C. Hoock, and B. Neumcke, *Morphological and electrophysiological properties of centrifuged stratified Xenopus oocytes.* Biology of the Cell, 1995. **84**(3): p. 129-138.

118. Schutt, E.G., et al., *Injectable microbubbles as contrast agents for diagnostic ultrasound imaging: The key role of perfluorochemicals.* Angewandte Chemie-International Edition, 2003. **42**(28): p. 3218-3235.

119. Feigenba.H, et al., *Identification of Ultrasound Echoes from Left Ventricle by Use of Intracardiac Injections of Indocyanine Green.* Circulation, 1970. **41**(4): p. 615-&.

120. Feinstein, S.B., et al., *Two-dimensional contrast echocardiography. I. In vitro development and quantitative analysis of echo contrast agents.* J Am Coll Cardiol, 1984. **3**(1): p. 14-20.

121. Stride, E. and N. Saffari, *Microbubble ultrasound contrast agents: a review.* Proceedings of the Institution of Mechanical Engineers Part H-Journal of Engineering in Medicine, 2003. **217**(H6): p. 429-447.

122. Schneider, M., et al., *Polymeric Microballoons as Ultrasound Contrast Agents - Physical and Ultrasonic Properties Compared with Sonicated Albumin.* Invest Radiol, 1992. **27**(2): p. 134-139.

123. Stride, E. and M. Edirisinghe, *Novel microbubble preparation technologies.* Soft Matter, 2008. **4**(12): p. 2350-2359.

124. Yount, D.E., *Skins of Varying Permeability - Stabilization Mechanism for Gas Cavitation Nuclei.* Journal of the Acoustical Society of America, 1979. **65**(6): p. 1429-1439.

125. Kabalnov, A., et al., *Dissolution of multicomponent microbubbles in the bloodstream: 1. Theory.* Ultrasound in Medicine and Biology, 1998. **24**(5): p. 739-749.

126. Chomas, J.E., et al., *Mechanisms of contrast agent destruction.* Ieee Transactions on Ultrasonics Ferroelectrics and Frequency Control, 2001. **48**(1): p. 232-248.

127. Unger, E.C., et al., *Acoustically active lipospheres containing paclitaxel - A new therapeutic ultrasound contrast agent.* Invest Radiol, 1998. **33**(12): p. 886-892.

128. Zhao, Y.Z., et al., *Preparation, characterization and in vivo observation of phospholipid-based gas-filled microbubbles containing hirudin.* Ultrasound in Medicine and Biology, 2005. **31**(9): p. 1237-1243.

129. Christiansen, C., et al., *Physical and Biochemical-Characterization of Albunex(Tm), a New Ultrasound Contrast Agent Consisting of Air-Filled Albumin Microspheres Suspended in a Solution of Human Albumin.* Biotechnology and Applied Biochemistry, 1994. **19**: p. 307-320.

130. Grinstaff, M.W. and K.S. Suslick, *Air-Filled Proteinaceous Microbubbles - Synthesis of an Echo-Contrast Agent.* Proceedings of the National Academy of Sciences of the United States of America, 1991. **88**(17): p. 7708-7710.

131. Nyborg, W.L., *Biological effects of ultrasound: development of safety guidelines. Part II: general review.* Ultrasound in Medicine and Biology, 2001. **27**(3): p. 301-33.

132. Joscelyne, S.M. and G. Tragardh, *Membrane emulsification - a literature review.* Journal of Membrane Science, 2000. **169**(1): p. 107-117.

133. Kukizaki, M. and M. Goto, *Size control of nanobubbles generated from Shirasu-porous-glass (SPG) membranes.* Journal of Membrane Science, 2006. **281**(1-2): p. 386-396.

134. Kawakatsu, T., et al., *The effect of the hydrophobicity of microchannels and components in water and oil phases on droplet formation in microchannel water-in-oil emulsification.* Colloids and Surfaces a-Physicochemical and Engineering Aspects, 2001. **179**(1): p. 29-37.

135. Hettiarachchi, K., et al., *On-chip generation of microbubbles as a practical technology for manufacturing contrast agents for ultrasonic imaging.* Lab on a Chip, 2007. **7**(4): p. 463-468.

136. Pancholi, K.P., et al., *Novel methods for preparing phospholipid coated microbubbles.* Eur Biophys J, 2008. **37**(4): p. 515-20.

137. Dollet, B., et al., *Role of the channel geometry on the bubble pinch-off in flow-focusing devices.* Physical Review Letters, 2008. **100**(3).

138. Pancholi, K., E. Stride, and M. Edirisinghe, *Dynamics of bubble formation in highly viscous liquids.* Langmuir, 2008. **24**(8): p. 4388-4393.

139. Castro-Hernandez, E., et al., *Microbubble generation in a co-flow device operated in a new regime.* Lab on a Chip, 2011. **11**(12): p. 2023-2029.

140. McNaught, A.D., A. Wilkinson, and International Union of Pure and Applied Chemistry., *Compendium of chemical terminology : IUPAC recommendations*. 2nd ed1997, Oxford: Blackwell Science. 450 p.

141. Helmholtz, H. Pogg. Ann, 1853. **LXXXIX**(211).

142. Gouy, L.G., *Sur la constitution de la charge électrique à la surface d'un électrolyte.* Comptes rendus hebdomadaires des séances de l'Académie des sciences, 1909. **149**: p. 654-657.

143. Chapman, D.L., *A Contribution to the Theory of Electrocapillarity.* Philosophical Magazine, 1913. **25**(148): p. 475-481.

144. Sakakima, Y., et al., *Gene therapy for hepatocellular carcinoma using sonoporation enhanced by contrast agents.* Cancer Gene Therapy, 2005. **12**(11): p. 884-889.

145. Fong, S.W., E. Klaseboer, and B.C. Khoo, *Interaction of microbubbles with high intensity pulsed ultrasound.* Journal of the Acoustical Society of America, 2008. **123**(3): p. 1784-1793.

146. Karshafian, R., et al., *Ultrasound-induced uptake of different size markers in mammalian cells.* 2005 Ieee Ultrasonics Symposium, Vols 1-4, 2005: p. 13-16.

147 Lisheng, W., et al., *Evaluation of MTS, XTT, MTT and3HTdR incorporation for assessing hepatocyte density, viability and proliferation*. Methods in Cell Science, 1996. 18(3): p. 249-255.

148. Kvale, S., et al., *Size fractionation of gas-filled microspheres by flotation.* Separations Technology, 1996. **6**(4): p. 219-226.

149. Chan, D.Y.C. and R.G. Horn, *The Drainage of Thin Liquid-Films between Solid-Surfaces.* Journal of Chemical Physics, 1985. **83**(10): p. 5311-5324.

150. Boal, D.H., *Mechanics of the cell*. 2nd ed2012, Cambridge ; New York: Cambridge University Press. xiv, 608 p.

151. Launiere, C.A., et al., *Rheologically biomimetic cell suspensions for decreased cell settling in microfluidic devices.* Biomedical Microdevices, 2011. **13**(3): p. 549-557.

152. Hideshima, S., et al., *Relation between Effective Charge Numbers and Signals Caused by Protein Adsorption on Field Effect Transistor Detection.* Bioelectronics, Biointerfaces, and Biomedical Applications 4, 2011. **35**(7): p. 121-124.

153. Das, C., et al., *Nanoscale mechanical probing of supported lipid bilayers with atomic force microscopy.* Physical Review E, 2010. **82**(4).

154. Grover, W.H., et al., *Measuring single-cell density.* Proceedings of the National Academy of Sciences of the United States of America, 2011. **108**(27): p. 10992-10996.

155. Chan, D.Y.C., E. Klaseboer, and R. Manica, *Film drainage and coalescence between deformable drops and bubbles.* Soft Matter, 2011. **7**(6): p. 2235-2264.

156. Tabor, R.F., et al., *Repulsive van der Waals Forces in Soft Matter: Why Bubbles Do Not Stick to Walls.* Physical Review Letters, 2011. **106**(6).

157. Faghihnejad, A. and H.B. Zeng, *Hydrophobic interactions between polymer surfaces: using polystyrene as a model system.* Soft Matter, 2012. **8**(9): p. 2746-2759.

158. Pocivavsek, L., et al., *Lateral stress relaxation and collapse in lipid monolayers.* Soft Matter, 2008. **4**(10): p. 2019-2029.

159. Ma, Y., et al., *Novel docetaxel-loaded nanoparticles based on PCL-Tween 80 copolymer for cancer treatment.* Int J Nanomedicine, 2011. **6**: p. 2679-88.

160. Suresh Reddy, J., V. Venkateswarlu, and G.A. Koning, *Radioprotective effect of transferrin targeted citicoline liposomes.* J Drug Target, 2006. **14**(1): p. 13-9.

161. Rico, C.M., et al., *Interaction of Nanoparticles with Edible Plants and Their Possible Implications in the Food Chain.* Journal of Agricultural and Food Chemistry, 2011. **59**(8): p. 3485-3498.

162. Campbell, N.A. and J.B. Reece, *Biology*. 8th ed2008, San Francisco: Pearson Benjamin Cummings. xlvi, 1267, [151] p.

163. Martin-Ortigosa, S., et al., *Parameters Affecting the Efficient Delivery of Mesoporous Silica Nanoparticle Materials and Gold Nanorods into Plant Tissues by the Biolistic Method.* Small, 2012. **8**(3): p. 413-422.

164. Elghabi, Z., S. Ruf, and R. Bock, *Biolistic co-transformation of the nuclear and plastid genomes.* Plant Journal, 2011. **67**(5): p. 941-948.

165. Finer, J.J., et al., *Development of the Particle Inflow Gun for DNA Delivery to Plant-Cells.* Plant Cell Reports, 1992. **11**(7): p. 323-328.

166. Abumhadi, N., et al., *Development of the particle inflow gun and optimizing the particle bombardment method for efficient genetic transformation in mature embryos of cereals.* Biotechnology & Biotechnological Equipment, 2001. **15**(2): p. 87-96.

167. Vain, P., et al., *Development of the Particle Inflow Gun.* Plant Cell Tissue and Organ Culture, 1993. **33**(3): p. 237-246.

168. Takeuchi, Y., M. Dotson, and N.T. Keen, *Plant Transformation - a Simple Particle Bombardment Device Based on Flowing Helium.* Plant Molecular Biology, 1992. **18**(4): p. 835-839.

169. Blackhall, N.W., et al., *Flow Cytometric Quantification of Electroporation-Mediated Uptake of Macromolecules into Plant-Protoplasts.* Protoplasma, 1995. **186**(1-2): p. 50-56.

170. Azencott, H.R., G.F. Peter, and M.R. Prausnitz, *Influence of the cell wall on intracellular delivery to algal cells by electroporation and sonication.* Ultrasound in Medicine and Biology, 2007. **33**(11): p. 1805-1817.

171. Vandam, G.J., et al., *Application of the Fitc-Anti-Fitc-Gold System to Ultrastructural-Localization of Antigens.* Journal of Histochemistry & Cytochemistry, 1991. **39**(12): p. 1725-1728.

172. Cho, H.K., et al., *Synthesis and characterization of fluorescein isothiocyanate (FITC)-labeled PEO-PCL-PEO triblock copolymers for topical delivery.* Polymer, 2009. **50**(11): p. 2357-2364.

173. Bentov, S., C. Brownlee, and J. Erez, *The role of seawater endocytosis in the biomineralization process in calcareous foraminifera.* Proceedings of the National Academy of Sciences of the United States of America, 2009. **106**(51): p. 21500-21504.

174. Michaelis, S., et al., *Macroporous silicon chips for laterally resolved, multi-parametric analysis of epithelial barrier function.* Lab on a Chip, 2012. **12**(13): p. 2329-2336.

175. Li, Y.S., et al., *Optimising ultrasound-mediated gene transfer (sonoporation) in vitro and prolonged expression of a transgene in vivo: Potential applications for gene therapy of cancer.* Cancer Letters, 2009. **273**(1): p. 62-69.

176. Kaler, K. V. and Jones, T. B. , *Dielectrophoretic spectra of single cells determined by feedback-controlled levitation*, Biophys J., 1990. **57**(2): p. 173-182.

177. Weigel, D. and J. Glazebrook, *Arabidopsis : a laboratory manual*2002, Cold Spring Harbor, N.Y.: Cold Spring Harbor Laboratory Press. xii, 354 p.

178. Ghadiali, S.N. and H.L. Dailey, *Mechanobiology and Finite Element Analysis of Cellular Injury During Microbubble Flows.* Cellular and Biomolecular Mechancis and Mechanobiology, 2011. **4**: p. 373-429.

179. Alcaraz, J., et al., *Microrheology of human lung epithelial cells measured by atomic force microscopy.* Biophysical Journal, 2003. **84**(3): p. 2071-2079.

180. Balland, M., et al., *Power laws in microrheology experiments on living cells: Comparative analysis and modeling.* Physical Review E, 2006. **74**(2).

181. Trepat, X., et al., *Viscoelasticity of human alveolar epithelial cells subjected to stretch.* American Journal of Physiology-Lung Cellular and Molecular Physiology, 2004. **287**(5): p. L1025-L1034.

182. Trepat, X., et al., *Thrombin and histamine induce stiffening of alveolar epithelial cells.* Journal of Applied Physiology, 2005. **98**(4): p. 1567-1574.

183. Okabe, K., et al., *Intracellular temperature mapping with a fluorescent polymeric thermometer and fluorescence lifetime imaging microscopy.* Nature Communications, 2012. **3**.

184. Sankin, G.N., F. Yuan, and P. Zhong, *Pulsating Tandem Microbubble for Localized and Directional Single-Cell Membrane Poration.* Physical Review Letters, 2010. **105**(7).

185. Ohl, C.D., et al., *Sonoporation from jetting cavitation bubbles.* Biophysical Journal, 2006. **91**(11): p. 4285-4295.

186. Kodama, T., et al., *Interaction of impulsive pressures of cavitation bubbles with cell membranes during sonoporation.* Therapeutic Ultrasound, 2006. **829**: p. 34-38.

187. McGarry, J.G. and P.J. Prendergast, *A three-dimensional finite element model of an adherent eukaryotic cell.* Eur Cell Mater, 2004. **7**: p. 27-33; discussion 33-4.

188. Jean, R.P., C.S. Chen, and A.A. Spector, *Finite-element analysis of the adhesion-cytoskeleton-nucleus mechanotransduction pathway during endothelial cell rounding: axisymmetric model.* J Biomech Eng, 2005. **127**(4): p. 594-600.

189. Ofek, G., R.M. Natoli, and K.A. Athanasiou, *In situ mechanical properties of the chondrocyte cytoplasm and nucleus.* J Biomech, 2009. **42**(7): p. 873-7.

190. Guilak, F. and V.C. Mow, *The mechanical environment of the chondrocyte: a biphasic finite element model of cell-matrix interactions in articular cartilage.* J Biomech, 2000. **33**(12): p. 1663-73.

191. Ferko, M.C., et al., *Finite-element stress analysis of a multicomponent model of sheared and focally-adhered endothelial cells.* Ann Biomed Eng, 2007. **35**(2): p. 208-23.

192. Kaazempur-Mofrad, M.R., et al., *Role of simulation in understanding biological systems.* Computers & Structures, 2003. **81**(8-11): p. 715-726.

193. Laurent, V.M., et al., *Assessment of mechanical properties of adherent living cells by bead micromanipulation: Comparison of magnetic twisting cytometry vs optical tweezers.* Journal of Biomechanical Engineering-Transactions of the Asme, 2002. **124**(4): p. 408-421.

194. Mijailovich, S.M., et al., *A finite element model of cell deformation during magnetic bead twisting.* Journal of Applied Physiology, 2002. **93**(4): p. 1429-1436.

195. Lim, C.T., E.H. Zhou, and S.T. Quek, *Mechanical models for living cells - A review.* J Biomech, 2006. **39**(2): p. 195-216.

196. Ohayon, J., et al., *Analysis of nonlinear responses of adherent epithelial cells probed by magnetic bead twisting: A finite element model based on a homogenization approach.* Journal of Biomechanical Engineering-Transactions of the Asme, 2004. **126**(6): p. 685-698.

197. Dailey, H.L., et al., *Image-based finite element modeling of alveolar epithelial cell injury during airway reopening.* Journal of Applied Physiology, 2009. **106**(1): p. 221-232.

198. Bryant, J.C., et al., *Massive Fluid-Suspension Cultures of Certain Mammalian Tissue Cells .3. Exploratory Supplementation Experiments with Chemically Defined Medium Natc-109.* Journal of the National Cancer Institute, 1960. **24**(4): p. 859-871.

199. Telling, R.C. and R. Elsworth, *Submerged Culture of a Hamster Kidney Cells in a Stainless Steel Vessel.* Biotechnology and Bioengineering, 1965. **7**(3): p. 417-&.

200. Augenstein, D.C., A.J. Sinskey, and D.I. Wang, *Effect of shear on the death of two strains of mammalian tissue cells.* Biotechnology and Bioengineering, 1971. **13**(3): p. 409-18.

201. Midler, M. and R.K. Finn, *A Model System for Evaluating Shear in Design of Stirred Fermentors.* Biotechnology and Bioengineering, 1966. **8**(1): p. 71-&.

202. Handa, A., A.N. Emery, and R.E. Spier, *On the evaluation of gas-liquid interfacial effects on hybridoma viability in bubble column bioreactors.* Dev Biol Stand, 1987. **66**: p. 241-53.

203. Bavarian, F., L.S. Fan, and J.J. Chalmers, *Microscopic visualization of insect cell-bubble interactions. I: Rising bubbles, air-medium interface, and the foam layer.* Biotechnol Prog, 1991. **7**(2): p. 140-50.

204. Trinh, K., et al., *Quantification of Damage to Suspended Insect Cells as a Result of Bubble Rupture.* Biotechnology and Bioengineering, 1994. **43**(1): p. 37-45.

205. Tramper, J. and J.M. Vlak, *Bioreactor design for growth of shear-sensitive mammalian and insect cells.* Adv Biotechnol Processes, 1988. **7**: p. 199-228.

206. Bilek, A.M., K.C. Dee, and D.P. Gaver, *Mechanisms of surface-tension-induced epithelial cell damage in a model of pulmonary airway reopening.* Journal of Applied Physiology, 2003. **94**(2): p. 770-783.

207. Tschumperlin, D.J. and S.S. Margulies, *Equibiaxial deformation-induced injury of alveolar epithelial cells in vitro.* American Journal of Physiology-Lung Cellular and Molecular Physiology, 1998. **275**(6): p. L1173-L1183.

208. Jacob, A.M. and D.P. Gaver, *An investigation of the influence of cell topography on epithelial mechanical stresses during pulmonary airway reopening.* Physics of Fluids, 2005. **17**(3).

209. Slomka, N. and A. Gefen, *Cell-to-cell variability in deformations across compressed myoblasts.* J Biomech Eng, 2011. **133**(8): p. 081007.

210. Slomka, N. and A. Gefen, *Confocal microscopy-based three-dimensional cell-specific modeling for large deformation analyses in cellular mechanics.* J Biomech, 2010. **43**(9): p. 1806-16.

211. Or-Tzadikario, S. and A. Gefen, *Confocal-based cell-specific finite element modeling extended to study variable cell shapes and intracellular structures: the example of the adipocyte.* J Biomech, 2011. **44**(3): p. 567-73.

212. Slomka, N., C.W.J. Oomens, and A. Gefen, *Evaluating the effective shear modulus of the cytoplasm in cultured myoblasts subjected to compression using an inverse finite element method.* Journal of the Mechanical Behavior of Biomedical Materials, 2011. **4**(7): p. 1559-1566.

213. He, C., et al., *Biomolecule delivery into canola protoplasts by centrifuging cells with microbubbles.* Febs Letters, 2013. **587**(3): p. 285-290.

214. Chuan. H, Q.G., Hongbo Z., Hao Z., Min H., James X., Jie C., *Microbubble-Enhanced Cell Membrane Permeability in High Gravity Field.* Cellular and Molecular Bioengineering, 2013.

215. Geers, B., et al., *Elucidating the mechanisms behind sonoporation with adeno-associated virus-loaded microbubbles.* Mol Pharm, 2011. **8**(6): p. 2244-51.

216. Lokhandwalla, M., et al., *Mechanical haemolysis in shock wave lithotripsy (SWL): II. In vitro cell lysis due to shear.* Physics in Medicine and Biology, 2001. **46**(4): p. 1245-1264.

217. Kudo, N., K. Okada, and K. Yamamoto, *Sonoporation by Single-Shot Pulsed Ultrasound with Microbubbles Adjacent to Cells.* Biophysical Journal, 2009. **96**(12): p. 4866-4876.

218. Geddes, D.M., R.S. Cargill, 2nd, and M.C. LaPlaca, *Mechanical stretch to neurons results in a strain rate and magnitude-dependent increase in plasma membrane permeability.* J Neurotrauma, 2003. **20**(10): p. 1039-49.

219. Trickey, W.R., et al., *Determination of the Poisson's ratio of the cell: Recovery properties of chondrocytes after release from complete micropipette aspiration (Trickey et al., Journal of Biomechanics, 39 (2006) 78-87 - Response to Dr. Schachar.* J Biomech, 2006. **39**(12): p. 2344-2345.